Hydrogen Burning of ^{23}Na in Globular Cluster Red Giant Stars

by

C. Rowland

A dissertation submitted to the faculty of the University of North Carolina at Chapel Hill in partial fulfillment of the requirements for the degree of Doctor of Philosophy in the Department of Physics & Astronomy.

Chapel Hill

2003

Approved:

C. Iliadis, Advisor

A. E. Champagne, Reader

B. W. Carney, Reader

ABSTRACT

C. ROWLAND: Hydrogen Burning of ^{23}Na in Globular Cluster Red Giant Stars
(Under the Direction of C. Iliadis)

The standard model of stellar evolution predicts constant surface abundances for globular cluster stars on the red giant branch. Contrary to these expectations, stars within a given globular cluster can show large variations in the abundance of C, N, and O as well as certain light metals, such as Na and Al. Also observed are global anticorrelations, such as that between O and Na. The question that rises is whether these variations are due to primordial differences in material that formed the cluster or from extra physics beyond the standard theory of stellar evolution, such as mixing.

Answering this question requires reliable thermonuclear reaction rates. The ^{23}Na(p,α)^{20}Ne and ^{23}Na(p,γ)^{24}Mg reactions are part of the Ne-Na cycle and are important for nucleosynthesis in globular cluster red giant stars. Both reactions are uncertain at astrophysically interesting temperatures, leading to uncertainties in the predicted abundances.

For nuclear reactions which proceed through narrow resonances, the reaction rates are directly proportional to the resonance strengths. The absolute strength of the $E_R^{Lab} = 338$ keV resonance in ^{23}Na(p,α)^{20}Ne was measured and used as a standard strength in determining the reaction rate. Prior to the present work, no standard strengths for this reaction were available. For the ^{23}Na(p,γ)^{24}Mg reaction, the uncertainty in the reaction rate comes from a resonance at $E_R^{cm} = 144$ keV. Traditionally this resonance has been difficult to measure because of low count rates combined with a large background. In the present work a technique for minimizing background via coincidences was developed. This technique was used to search for and obtain a much improved upper limit for the $E_R^{cm} = 144$ keV resonance. The upper limit in the present work is over an order of magnitude lower than the current literature value.

Some astrophysical implications resulting from the new ^{23}Na + p reaction rates are explored via a nuclear reaction network and stellar models.

ACKNOWLEDGMENTS

Thank you Christian Iliadis for teaching me so much. Thank you for being so patient when you didn't have to be. Thank you for being such an excellent mentor and teacher. You are the best role model a student could ask for. Thank you for spending so much time and energy on this project. Your encouragement and enthusiasm has made all the difference. Thank you for always having time for me. You never claimed to be too busy, even though I knew you were. Thank you for working so hard to see me through to the end. You are a great scientist and it has been a real honor and privilege to work with you.

Thank you Art Champagne for your constant support, thoughtful advice and generous assistance. Thank you for working so hard on all my experiments, and thank you for making LENA a reality.

Thank you Bruce Carney for mentoring me in my Master's project. The time I spent working for you was some of the most well spent. Thank you for taking me to Kitt Peak. I will never forget walking up to the Mayall Observatory at twilight. Thank you for teaching me to be an astronomer.

Thank you Hugon Karwowski for being a constant source of support. Thank you for working hard to make the transition to the nuclear group easier for me. Thank you about caring so much about the progress of my project.

Thank you Rich Superfine for your great advice and encouragement.

Thank you Bill Thompson for teaching me quantum mechanics. You went well beyond the call of duty to help me out, and I will never forget it.

Thank you Ryan Fitzgerald for being so generous with your time and knowledge. You have been a constant source of support and encouragement. I truly cannot thank

you enough.

Thank you Bob Runkle for your tireless work on LENA. You did an amazing job.

Thank you Chris Fox and Johannes Pollanen for your hard work during experiments. Thank you for coming in so early and staying so late. Thank you for making me laugh when nothing worked.

Thank you Brian Fisher for sticking it out with me. You have been so helpful and understanding and a great friend through these years.

Thank you Rob Cavallo for your stellar models and reaction network code. Thank you helping me get it running at TUNL.

Thank you Richard O'Quinn for always making time to help me out. Thank you for coming in at 6am and keeping me awake. Thank you Chris Westerfeldt for never being too busy. It would take a good many more pages to list all the things you've done for me. Thank you John Dunham and Paul Carter for never turning away when I've needed help.

Thank you Michael Neece for teaching me how to Ramble. You are a fine teacher and an amazing person. I'm honored to know you.

Thank you Austin Guiles for letting me work and teach at Morehead Planetarium. Thank you for being so supportive and understanding. Thank you for always reminding me on Monday.

Thank you Kristi Concannon, Jennifer Mosher and Mitzi Boswell. Your friendship and understanding has meant a lot.

Thank you Bruce Wieland for giving me the opportunity to work at PET. Your taking a chance on me has opened up many doors.

Thank you Ron Canterna and Timothy Brown for mentoring me during my undergraduate research.

Thank you Tony Jusick, Kevin Riggs, and Tom Lick for teaching me physics during my years at Stetson. You are gifted physicists and teachers. I would not have made it through graduate school without the benefit of your instruction.

Thank you Eric Carr for learning with me. It was always so good to see that your office light was still on.

Thank you Kristen Houdeshell-Zajak for being my best friend. Thank you for staying up late and working so hard. Thank you for inspiring me. Thank you for your caring and friendship. I am surely the better for knowing you.

Thank you most of all Wende Rowland for your love and support.

To see a world in a grain of sand
And heaven in a wild flower
Hold infinity in the palm of your hand
And eternity in an hour
–William Blake

CONTENTS

LIST OF FIGURES

LIST OF TABLES

Chapter 1

Motivation and background

1.1 Globular cluster red giant stars

A globular cluster is a gravitationally bound group of hundreds of thousands of stars packed into a region of only about a hundred light years across. There are roughly 180 such clusters in the Milky Way Galaxy. Most globular clusters are members of the galactic halo and the rest are members of the thick disk. Their beauty is surpassed only by their utility to astronomy. As the oldest entities within the bounds of our galaxy, globulars act as fossils in tracing the origin and evolution of the Milky Way.

Globular clusters have also profoundly influenced our understanding of stellar evolution. A star's evolution is determined primarily by its mass and to a lesser extent by its chemical composition. Globular clusters are thought to be formed such that all stars within the cluster are born more or less simultaneously and from the same material, making them monometallic. Therefore, according to the standard model, the only variable among these stars is mass, or equivalently, evolutionary state.

Since globular clusters are so distant, astronomical observations generally focus on the most luminous stars within a cluster. These stars have left the main sequence and are on the tip of the red giant branch, that is the stars have reached the stage in their evolution where the majority of the hydrogen in the core has been converted into helium via the proton-proton chain and the star is fusing hydrogen in a shell surrounding an inert helium core. The main sequence and red giant branch can be

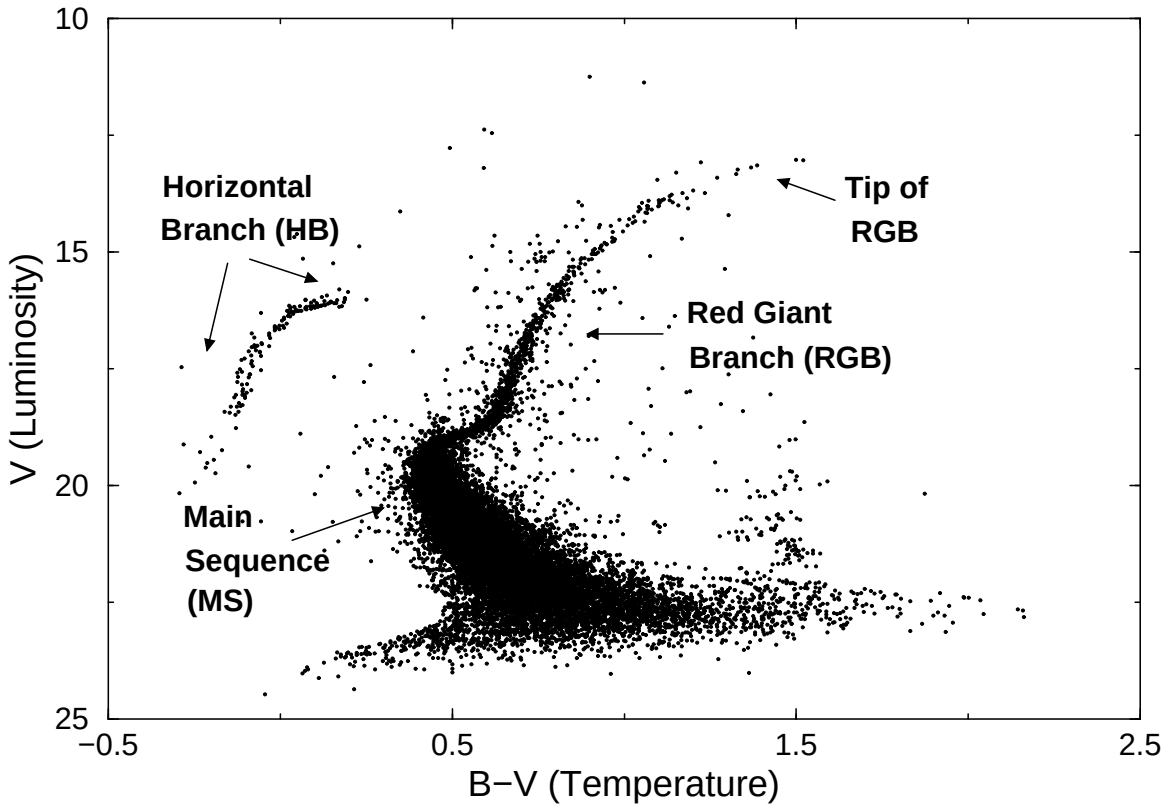

Figure 1.1: Color-magnitude diagram for the globular cluster M2 [Lee99].

seen on a color-magnitude diagram. Such a diagram plots luminosity vs. temperature for each star in a globular cluster. Note that temperature increases to the left of the diagram. Fig. 1.1 shows the color-magnitude diagram for the globular cluster M2. For stars on the red giant branch, hydrogen in the shell is converted into helium via the carbon-nitrogen-oxygen (CNO) cycle and the proton-proton chain. For stars with temperatures high enough, additional cycles such as the neon-sodium (NeNa) and the magnesium-aluminum (MgAl) cycle also may occur. Both cycles involve large Coulomb barriers, so neither is significant as an additional stellar energy source. These cycles are, however, important for the nucleosynthesis of elements between ^{20}Ne and ^{27}Al [Rol88].

When a star first becomes a red giant it develops a convection zone which reaches down to a region where a limited amount of CNO-cycle burning occurs. This convective zone advances outward ahead of the CNO burning shell so that a firm connection

between the two is never established. A lack of connection between the convective zone and the shell suggests that there should be little change in the observed surface abundances of these stars. (It is worth noting here that measurements of chemical abundances reflect only what is in the photosphere, or outer envelope, of the star.) Some minor changes are expected. For example, a decline is expected in the $^{12}C/^{13}C$ ratio from the initially assumed solar value of 90 to about 20–30. Also, carbon abundances should drop by about 30% and nitrogen should increase by 80%. All other elements should remain unchanged since the convection zone does not reach deep enough into to CNO burning shell to dredge up processed material. Only a small increase in ^{13}C and ^{14}N occur as a result of ^{12}C depletion during the CNO cycle. Further, interior temperatures are not hot enough to process elements heavier than oxygen [Kra94].

Additional changes in surface abundances are expected later in a star's evolution. As the CNO burning shell moves outward, the temperature in the inert helium core increases. Eventually the core ignites (the He core flash) and the star moves to the horizontal branch of the color-magnitude diagram. Evolution following the He core flash allows for processed material from the interior of the star to reach the surface so that abundance variations later in a star's life are not considered anomalous.

1.2 Predictions vs. observations

The standard model for stellar evolution predicts that there should be little change in the surface abundances of red giants within a monometallic globular cluster. Contrary to predictions, however, there are wide star-to-star variations in the abundances of elements such as C, N, O, Na, and Al. Some of these variations are related to evolutionary state and suggest that some extra process, such as non-canonical deep mixing, is responsible for the anomalies. Other variations could be due to primordial differences, possibly caused by the nucleosynthesis in stars of a previous generation enriching the material that formed the cluster.

Many of the abundance anomalies have been found to be consistent with a mixing

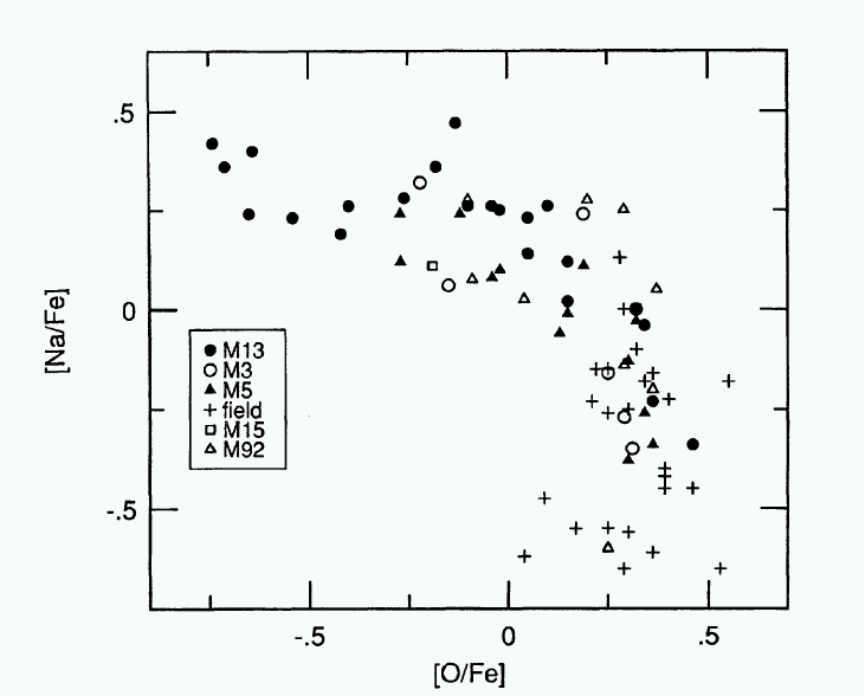

Figure 1.2: The Na-O anticorrelation among giant stars in globular clusters. [Kra94].

scenario, as described in Cavallo *et al* [Cav98]. For example, in metal poor and intermediate metallicity clusters, C is seen to decrease with increasing luminosity. This implies that material above the H-burning shell, where C and O are depleted is being transported to the outer convective envelope. Also consistent with a mixing hypothesis is the observation that in intermediate and metal-rich clusters, the $^{12}C/^{13}C$ ratio is seen to decrease with increasing luminosity. (The ratio decreases to an equilibrium value between 4 and 10.) Observations also show anticorrelations involving O with both N and Na, with the N and Na abundances increasing with luminosity. Further, there are star-to-star variations in Na, likely resulting from an evolutionary scenario. Fig. 1.2 shows the Na-O anticorrelation among giant stars at the tip of the RGB in five different globular clusters [Kra94]. The halo field stars (indicated by crosses) show no such anticorrelation.

Al is also found to be anticorrelated with O, with a stronger dependence on metallicity than the variations in Na. Observations show metal poor clusters with large amounts of Al and metal rich clusters with no Al enhancements at all. In the metal

poor clusters it is thought that the excess Al is a result of proton captures on ^{25}Mg and ^{26}Mg.

Observations of Mg abundances have proved to be most puzzling and seemingly inconsistent. For example, faint red giants with small Na enhancements are observed to have large Mg abundances. Therefore, it is expected that giants with large amounts of Na would have small Mg enhancements. This is true for about half of the giants observed. The rest of the giants having large amounts of Na show varying amounts of Mg. In the case of the highly luminous giants, most have an overabundance of Na, but over half of these stars show no Mg depletion. Understanding these Mg anomalies presents an observational challenge since there are three stable and relatively plentiful isotopes of Mg. The ^{24}Mg:^{25}Mg:^{26}Mg ratio is 79:10:11 on Earth and is assumed to be the same in the solar photosphere [Cav98]. Determining the abundances of individual isotopes is difficult, and although abundances of ^{24}Mg and the abundance sum of ^{25}Mg + ^{26}Mg have been observed by Shetrone [She96], it has not yet been possible to separate the three.

As mentioned above, observational evidence suggests that many of the above described abundance anomalies in globular cluster red giant stars are the result of non-canonical mixing between the surface and the deep stellar interior. It was suggested by Sweigart & Mengel [Swe79] that rotationally driven meridional circulation is responsible for this mixing and subsequent transfer of materials. In this scenario, material from the envelope would be mixed into two regions above the hydrogen-shell. In the outermost region, the CN (carbon-nitrogen) cycle processes material and closer to the hydrogen-shell, the ON (oxygen-nitrogen) cycle can occur. Hence in the star there are points where (i) carbon falls to half of its original value, (ii) oxygen reaches half of its original value, and (iii) the H abundance has dropped to half of its original value at the center of the hydrogen shell. Variations in the rotation rate from star to star result in different mixing depths and hence different amounts of processed material being brought to the envelope.

The mixing scenario can be studied in further detail by combining a nuclear reaction network with detailed stellar sequences. The result is a determination of abun-

dance profiles around the hydrogen-burning shell for different models of globular cluster red giant stars. Reaction rates determined in the present work and those presented in [Ili01], are used in combination with the stellar models of Cavallo *et al.* to determine the effects of reaction rate changes on the predicted abundances. The network and evolutionary sequences are combined in order to follow the production and destruction of the C, N, O, Ne, Na, Mg, and Al isotopes around the hydrogen-burning shell for several different models. A detailed discussion of the reaction network, evolutionary sequences, and consequences of mixing will be presented in Ch. 7.

Understanding the likelihood of either an evolutionary or primordial scenario and the mechanism by which it would occur requires reliable estimates of thermonuclear reaction rates. Of interest in the present work are the ^{23}Na$(p,\gamma)^{24}$Mg and ^{23}Na$(p,\alpha)^{20}$Ne reactions. Both reactions take place in the hydrogen-burning shell of globular cluster red giant stars. They are part of the NeNa cycle and are important for understanding nucleosynthesis in globular cluster red-giant stars. Fig. 1.3 shows the NeNa cycle. The solid arrows indicate a (p,γ) reaction, the dashed lines indicate β-decay, and the dotted line represents the ^{23}Na$(p,\alpha)^{20}$Ne reaction. If the ^{23}Na$(p,\alpha)^{20}$Ne rate is larger than the ^{23}Na$(p,\gamma)^{24}$Mg rate, there will be cycling through the NeNa cycle. Otherwise there will be leakage into the MgAl cycle.

As can be seen in Fig. 1.4, the reaction rates for ^{23}Na$(p,\gamma)^{24}$Mg and ^{23}Na$(p,\alpha)^{20}$Ne are uncertain at temperatures of astrophysical interest [Ili01]. The rate of ^{23}Na$(p,\gamma)^{24}$Mg is uncertain by four orders of magnitude between $T_9 = 0.04$ - 0.15. Shell hydrogen burning in red giant stars occurs in this region of uncertainty at $T_9 \approx 0.055$. The ^{23}Na$(p,\alpha)^{20}$Ne can be seen to be uncertain at $T_9 \leq 0.015$ by a factor of 150.

If the ratio of the (p,α) rate to the (p,γ) rate is considered, it is not possible to determine which rate is faster. In Fig. 1.5, the top curve shows the ratio of the upper limit of the (p,α) reaction rate to the lower limit of the (p,γ) reaction rate. The bottom curve is the ratio of the lower limit of the (p,α) reaction rate to the upper limit of the (p,γ) reaction rate. The middle line is the ratio of the recommended rates. It is clear that for $T_9 = 0.01 - 0.04$ the (p,α) rate dominates, but for $T_9 = 0.05 - 0.6$, it is not clear which rate is larger. This is precisely the temperature region of hydrogen-shell

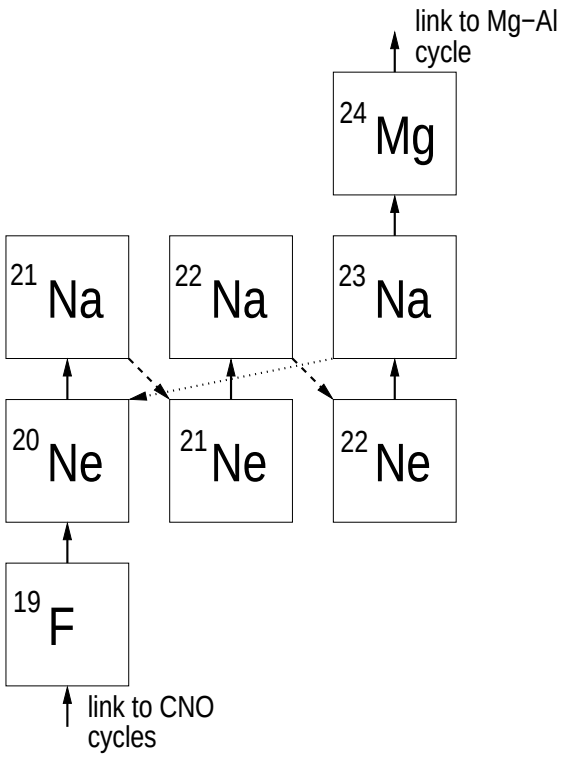

Figure 1.3: The Neon-Sodium Cycle.

burning in globular cluster red giant stars. If the (p,α) rate is larger, there will be cycling through the NeNa cycle and if the reverse is true, there will be leakage into the MgAl cycle.

1.3 Scope of the present work

The aim of this thesis is to reduce the uncertainties in the ^{23}Na$(p,\gamma)^{24}$Mg and ^{23}Na$(p,\alpha)^{20}$Ne reaction rates and to discuss their astrophysical significance in light of stellar model and network calculations. Thermonuclear reaction rates are determined by a combination of the resonant and nonresonant contributions to the reaction mechanism. For narrow, isolated resonances, the reaction rate is directly proportional to the resonance strength, $\omega\gamma$.

Resonance strengths are usually determined using the step-height of the thick target yield curve. This method requires knowledge of target and beam properties,

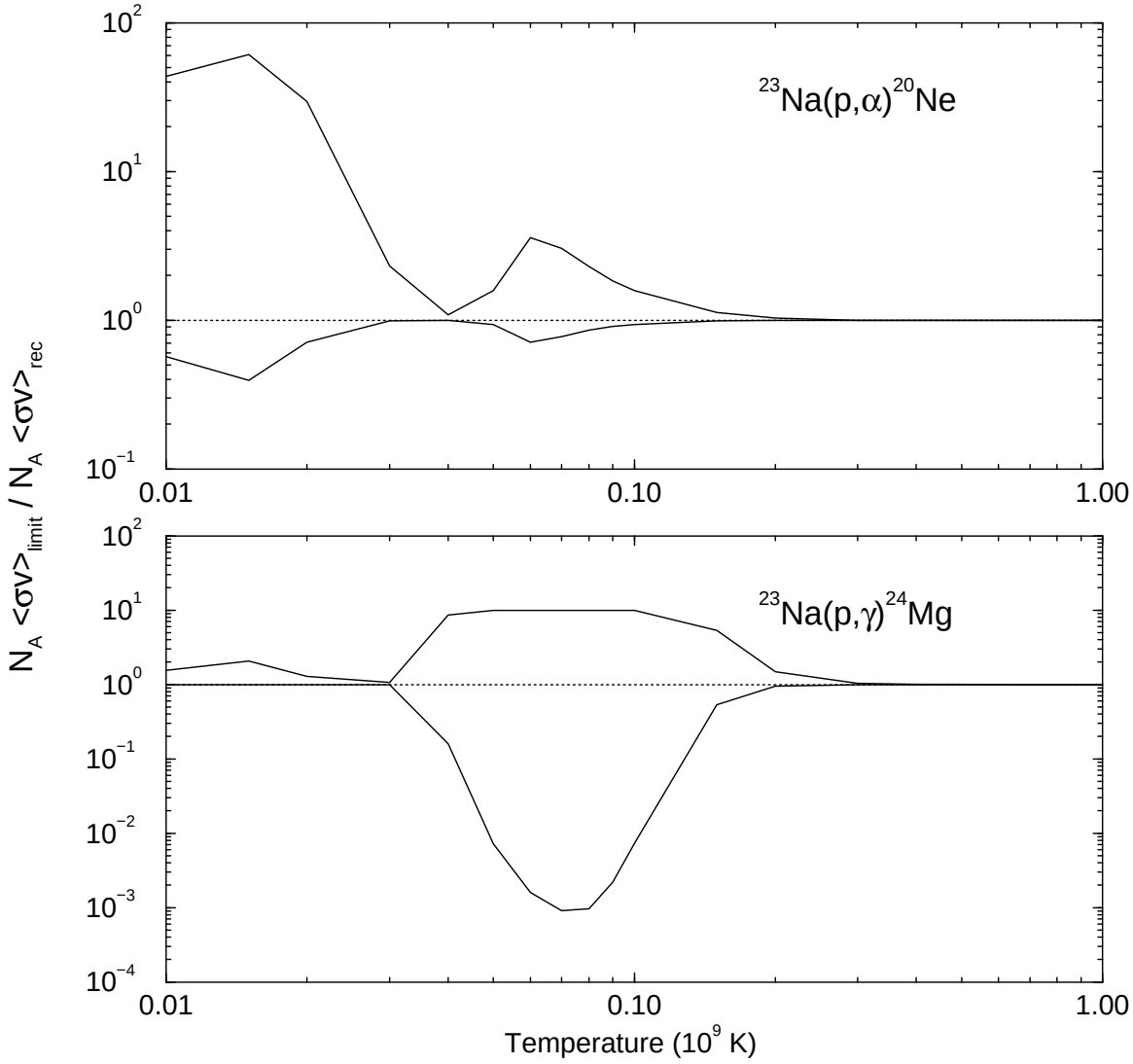

Figure 1.4: Ratio of the the upper and lower limits of the ^{23}Na$(p,\gamma)^{24}$Mg and ^{23}Na$(p,\alpha)^{20}$Ne reaction rates to the recommended values vs. temperature.

as well as absolute detection efficiencies. These factors are difficult to determine and are sources of potential systematic errors. Discrepancies in the literature by factors of 2 or more between different absolute resonance strengths are not uncommon. For the ^{23}Na(p,α)^{20}Ne reaction there were no standard resonance strengths available prior to this work. Consequently systematic uncertainties were thought to be large. In the present work a standard strength for the E_R = 338 keV resonance was determined using a method that does not depend on the properties of the target or beam.

In the case of ^{23}Na(p,γ)^{24}Mg, the largest source of uncertainty in the reaction rate

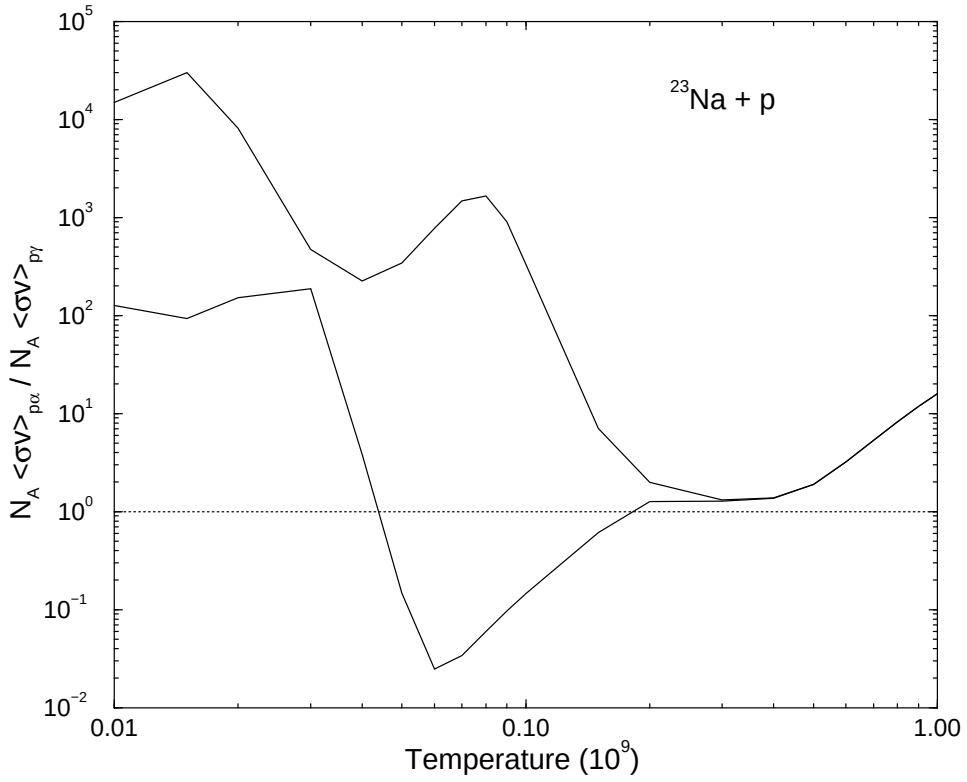

Figure 1.5: Ratio of the (p,α) rate to the (p,γ) rate vs. temperature.

comes from an expected resonance at $E_R^{Lab} = 144$ keV. Measurement of this resonance has been impossible so far and the literature reports only an upper limit for the resonance strength [Gör89]. The difficulty lies in detecting a very small γ-ray yield in the presence of large background. In the present work, a coincidence technique was developed in order to minimize this background so that weak resonances (like that at $E_R^{Lab} = 144$ keV) may be detected more easily, or at least an improved upper limit can be obtained.

The present work focuses on what consequences improved ^{23}Na+p reaction rates have on the abundance profiles of globular cluster red giant stars. It should be noted, however, that these rates are also important in other astronomical regimes. For example the ^{23}Na+p reaction rates are important for the understanding of nucleosynthesis during novae outbursts. Nova explosions appear to be caused by the transfer of matter from a normal star, through an accretion disk, onto the surface of a white dwarf. This matter is mostly hydrogen, and when it accumulates on the surface of the white dwarf,

it forms a layer of unprocessed fuel. This layer deepens, becoming denser and hotter until the hydrogen fuses in a sudden explosion. The nova explosion ejects significant amounts of nuclear processed material into the interstellar medium.

Among the isotopes synthesized during the explosion, the radioactive nuclei ^{22}Na and ^{26}Al have generated particular astrophysical interest [Jos99]. Deriving limits on the production and destruction of these isotopes is important in order to develop theoretical models of nova explosions. Also, novae are thought to be potential contributors to Galactic ^{26}Al. Since the synthesis of ^{22}Na and ^{26}Al in novae is very dependent on the adopted nuclear reaction rates, the uncertainties present in some key reactions of both NeNa and MgAl cycles may significantly modify the expected yields [Jos99]. The implications of the improved ^{23}Na + p reaction rates on novae are outside of the scope of the present work, however these implications will certainly be studied elsewhere.

Ch. 2 describes the nuclear and astrophysics formalism used in this work. Ch. 3 describes the laboratory equipment, experimental setups and target production for each measurement. Ch. 4 discusses experimental techniques, including the coincidence method used to minimize background. Ch. 5 discusses in detail the measurement of the E_R = 338 keV resonance in ^{23}Na(p,α)^{20}Ne. In Ch. 6, the coincidence technique is applied to the search for the E_R = 144 keV resonance in ^{23}Na(p,γ)^{24}Mg, and the method used in determining an improved upper limit for the strength is presented. Finally, Ch. 7 discusses the reaction rates, network and stellar model calculations, and the resulting astrophysical implications. Unless noted otherwise, all energies are given in the laboratory frame of reference.

Chapter 2

Nuclear astrophysics formalism

2.1 The thermonuclear reaction rate

The reaction rate per particle pair for a (p,γ) or a (p,α) reaction is given by [Rol88]

$$\langle \sigma \mathrm{v} \rangle \;=\; \left(\frac{8}{\pi\mu}\right)^{1/2} \frac{1}{(kT)^{3/2}} \int_0^\infty \sigma(E) E e^{(-\frac{E}{kT})} dE, \tag{2.1}$$

where μ is the reduced mass, k is the Boltzmann constant and σ is the total cross section. The rate in Eq. 2.1 is dependent upon the the probability of the incident proton interacting with the nucleus of interest. This probability is expressed in terms of the total cross section, σ. Classically, the cross section is equal to the combined geometrical area of the projectile and target nucleus. Nuclear reactions, however, are governed by the laws of quantum mechanics, so the geometrical cross section is instead an energy dependent quantity. Determination of this total cross section requires knowledge of the resonant and nonresonant contributions to the nuclear reaction mechanism.

The nonresonant part of the cross section may be expressed as

$$\sigma(E) \;=\; \frac{1}{E} e^{(-2\pi\eta)} S(E). \tag{2.2}$$

Here η is the Sommerfeld parameter given by

$$\eta \;=\; \frac{Z_1 Z_2 e^2}{\hbar v}, \tag{2.3}$$

where Z_1 and Z_2 are the integral charges of the interacting nuclei. The astrophysical-factor, S(E), is defined by Eq. 2.2 and contains information about the purely nuclear effects. For nonresonant reactions, this factor varies smoothly with bombarding proton energy.

If Eq. 2.2 is inserted into Eq. 2.1, the reaction rate per particle pair becomes

$$\langle \sigma \mathrm{v} \rangle \;=\; \left(\frac{8}{\pi\mu}\right)^{1/2} \frac{1}{(kT)^{3/2}} \int_0^\infty S(E) exp\left(-\frac{E}{kT} - \frac{b}{E^{1/2}}\right) dE. \tag{2.4}$$

The quantity b is given by

$$b \;=\; \frac{(2\mu)^{1/2}\pi e^2 Z_1 Z_2}{\hbar} \;=\; 0.989 \;\; Z_1 Z_2 \mu^{1/2} \;\; (MeV)^{1/2}. \tag{2.5}$$

The energy dependence of the integrand in Eq. 2.4 is determined primarily by the exponential term. The first term in the exponent is a measure of the number of particles available in the high-energy tail of the Maxwell-Boltzmann distribution. The second term in the exponent results from the Coulomb barrier penetrability. The product of these two terms leads to a peak of the integrand, called the Gamow peak, which defines a narrow energy window around the most effective stellar burning energy at a particular temperature. The energy for which the integrand in Eq. 2.4 has a maximum value is given by

$$E_o \;=\; \left(\frac{bkT}{2}\right)^{2/3} \;=\; 0.122 \;\; (Z_1^2 Z_2^2 \mu T_9^2)^{1/3} \;\; (keV), \tag{2.6}$$

and the 1/e width of the peak at E_o is given by

$$\Delta \;=\; \frac{4}{3^{1/2}} (E_o kT)^{1/2} e^{\left(\frac{2E_o}{kT}\right)} = 0.237 \;\; (Z_1^2 Z_2^2 \mu T_9^5)^{1/6} \;\; (keV). \tag{2.7}$$

Since the S-factor for a nonresonant reaction varies slowly as a function energy, it may be expanded in a Taylor series so that

$$S(E) \;=\; S(0) + E\dot{S}(0) + \frac{1}{2}\ddot{S}(0)E^2 ... \tag{2.8}$$

The terms S(0), $\dot{\mathrm{S}}(0)$, and $\ddot{\mathrm{S}}(0)$ are determined experimentally by a fit to the data. If the expansion for S(E) given in Eq. 2.8 is inserted into Eq. 2.4, the reaction rate per particle pair becomes a sum of integrals. As described in [Rol88], the S-factor in Eq. 2.4 can be replaced by an effective S-factor, S_{eff}, where

$$S_{eff} \;=\; S(0)\left[1+\frac{5}{12\tau}+\frac{\dot{S}(0)}{S(0)}\left(E_o+\frac{35}{36}kT\right)+\frac{1}{2}\frac{\ddot{S}(0)}{S(0)}\left(E_o^2+\frac{89}{36}E_okT\right)\right]. \quad (2.9)$$

Here τ is a dimensionless parameter given by

$$\tau=\frac{3E_o}{kT}. \quad (2.10)$$

Using Eq. 2.9, the non-resonant part of the reaction rate per particle pair from Eq. 2.4 may finally be written as

$$\langle\sigma \mathrm{v}\rangle_{NR} \;=\; \left(\frac{2}{\mu}\right)\frac{\Delta}{(kT)^{3/2}}\;S_{eff}(E_o)\;e^{\left(\frac{-3E_o}{kT}\right)}. \quad (2.11)$$

In the case of narrow and isolated resonances, the cross section can be described by the Breit-Wigner formula,

$$\sigma_{BW}(E) \;=\; \frac{\lambda^2}{4\pi}\frac{2J_R+1}{(2J_t+1)(2J_p+1)}\frac{\Gamma_p(E)\Gamma_x(E)}{(E_R-E)^2+\frac{1}{4}\Gamma(E)^2}, \quad (2.12)$$

where λ is the de Broglie wavelength and J_R, J_t, and J_p are the spin of the resonance, target, and proton, respectively. Γ_p is the proton partial width, Γ_x is the γ-ray or α-particle partial width, and Γ is the total width. The partial widths describe the probability of formation or decay of the resonance state. The integration of the Breit-Wigner cross section, σ_{BW}, gives

$$\int_0^\infty \sigma_{BW}(E)dE \;=\; \frac{\lambda_R^2}{4}\omega\frac{\Gamma_p\Gamma_x}{\Gamma}, \quad (2.13)$$

where λ_R is the de Broglie wavelength at the resonance energy and the quantity ω is a statistical spin factor given by

$$\omega \;=\; \frac{2J_R+1}{(2J_t+1)(2J_p+1)}. \quad (2.14)$$

The product of ω with the ratio $\gamma = \Gamma_p\Gamma_x/\Gamma$ is called the resonance strength, $\omega\gamma$. Substitution of σ_{BW} into Eq. 2.1 yields the reaction rate per particle pair for the case of several narrow resonances,

$$\langle \sigma \mathrm{v} \rangle_R = \left(\frac{2\pi}{\mu kT}\right)^{3/2} \hbar^2 \sum_i (\omega\gamma)_i \; exp\left(\frac{-E_{R_i}}{kT}\right), \tag{2.15}$$

where E_{R_i} are the resonance energies and the $\omega\gamma_i$ are the strengths of those individual resonances. Note that Eq. 2.15 is derived assuming that the energy dependence of the Maxwell-Boltzmann distribution and that of the partial widths is negligible over the width of the resonance.

2.2 Broad and subthreshold resonances

In the case of a broad resonance, the cross section $\sigma(\mathrm{E})$ extends over a wider energy range than in the case of narrow resonance. Consequently, the determination of the reaction rate per particle pair must take into account the energy dependence of the Breit-Wigner cross section. In Eq. 2.15, the wing of the resonance is neglected. If a resonance E_R does not fall within the range $\mathrm{E}_o \pm 2\Delta$ of the Gamow peak, then the narrow resonance reaction formalism given by Eq. 2.15 will not adequately describe the total resonance reaction rate [Ili01] and the wing of the resonance must be taken into account.

Since the Breit-Wigner cross section is described by the partial widths, it is necessary to determine the energy dependence of those widths for the case of broad resonances. In terms of the penetration factors, P, the proton or α-particle partial width is given by

$$\Gamma_x(E) = \Gamma_x(E_R)\frac{P(E)}{P(E_R)}, \tag{2.16}$$

and the γ-ray partial width is given by

$$\Gamma_\gamma(E) = \Gamma_\gamma(E_R) B_\gamma \left(\frac{E + Q_{p\gamma} - E_{xf}}{E_R + Q_{p\gamma} - E_{xf}}\right)^{2L+1}. \tag{2.17}$$

In Eq. 2.17, $Q_{p\gamma}$ is the reaction Q-value (E_R=E_x-Q), which for ^{23}Na(p,γ)^{24}Mg is 11692.9 $\pm$ 0.2 keV and for ^{23}Na(p,α)^{20}Ne is 2376.5 $\pm$ 0.2 keV [Aud95]. E_{xf} is the energy of the final state, B_γ is the primary γ-ray branching ratio to the final state, and L is the multipolarity of the γ-ray emitted in the decay. To determine the reaction rate for a broad resonance, the energy dependent partial widths can be substituted into the Breit-Wigner cross section given in Eq. 2.12. This cross section can then in turn be substituted into Eq. 2.1 after which a numerical integration will yield the reaction rate.

For resonances well below the Coulomb barrier, the partial width for the entrance channel will vary much more rapidly over the resonance region than the partial width for the exit channel. The resulting cross section is asymmetric with respect to the resonance energy, E_R, and will vary more rapidly for energies below E_R than for energies above E_R. This asymmetric shape of the cross section can be largely eliminated by parameterizing the cross section in terms of the S-factor as in Eq. 2.2. In this case, the low energy tails of broad resonances vary smoothly with energy and the formalism developed for nonresonant reactions can be applied for these cases.

In the case of subthreshold resonances, the energy of a state is smaller than the reaction Q-value and the excited state cannot be formed through this reaction channel at its excitation energy. In this case, the resonance energy E_R is negative, or equivalently, E_R is below the particle threshold Q with a value of E_R. However, a state located at an energy E_r has an associated width Γ. This width allows the state to be "seen" at energies above and below the value E_r so that in some cases the high-energy wing of a subthreshold state will extend above the particle threshold and contribute to the total reaction rate.

2.3 Proton partial widths and spectroscopic factors

The calculation of a resonant reaction rate depends upon the resonance strength, $\omega\gamma$, which by definition includes the partial widths. These partial widths may be estimated using spectroscopic factors, which can be measured in transfer reaction studies. This method uses the optical model to account for the fact that the incoming and outgoing plane waves of the interacting particles are distorted by the nucleus. If the state of interest cannot be described by a pure single-particle shell-model state, then the measured cross section is thus reduced from the calculated shell-model value by a number called the spectroscopic factor, S. A value of S = 1 corresponds to a pure single-particle shell model state.

At low resonance energies, the proton partial width is negligible compared to the γ-ray partial width. If the p- and γ-channel are the only channels open, then the resonance strength can be approximated by $\omega\gamma \approx \omega\Gamma_p$. The proton partial width can then be calculated for a given spectroscopic factor according to

$$\Gamma_p \;=\; C^2 S \Gamma_{sp}, \tag{2.18}$$

where C^2 is the isospin Clebsch-Gordan coefficient, S is the spectroscopic factor and Γ_{sp} is the partial width of a single-particle resonance located at the same energy as the resonance of interest [Ili01]. This quantity can be found numerically by solving the Schrödinger equation for the elastic scattering of protons by an optical model potential. Γ_p is given by [Ili97]

$$\Gamma_p \;=\; 2\frac{\hbar^2}{\mu a^2}\; P_l\; C^2 S\; \theta_{sp}^2 \tag{2.19}$$

where a is the interaction radius given by $a = a_0\ (\mathrm{A}_t^{1/3} + \mathrm{A}_p^{1/3})$, with A_p and A_t being the projectile and target mass numbers. P_l is the penetrability of the Coulomb and centrifugal barrier for orbital angular momentum l, and θ_{sp}^2 is the dimensionless single-particle reduced width and is written as

$$\theta_{sp}^2 \;=\; \frac{a}{2}\phi_l^2, \tag{2.20}$$

where ϕ_l^2(a) is the square of the single-particle radial wave function of the l orbit at the interaction radius a. In the literature it is assumed θ_{sp}^2 is equal to unity, but [Ili97] shows that this assumption leads to a large error in the calculation of Γ_p, which results in an overestimation of the reaction rates.

Chapter 3

Experimental equipment

3.1 Laboratories and accelerators

The experiments in the present work were performed at the Triangle Universities Nuclear Laboratory (TUNL). Measurement of the $E_R = 338$ keV resonance strength in ^{23}Na(p,α)^{20}Ne and the development and testing of the coincidence technique used to measure the $E_R = 144$ keV resonance in ^{23}Na(p,γ)^{24}Mg were both done at the Low Energy Beam Facility located at TUNL. The strength of the $E_R = 144$ keV resonance in ^{23}Na(p,γ)^{24}Mg was measured at the TUNL Laboratory for Experimental Nuclear Astrophysics (LENA).

A schematic of the Low Energy Beam Facility is shown in Fig 3.1. Unpolarized H^- ions are extracted from the Atomic Beam Polarized Ion Source at an energy of 75 keV. The H^- are bent through an inflection magnet and then accelerated through the 200 kV minitandem accelerator [Bla93]. At the center of the minitandem, electrons are stripped from the H^- and the resulting protons are sent through the analyzing magnet and delivered to the target chamber. For the tests of the coincidence technique and for the measurement of the $E_R = 338$ keV resonance in ^{23}Na(p,α)^{20}Ne, the minitandem provided proton beams of ≈ 1 μA in the energy range $E_p \leq 480$ keV with an uncertainty in absolute energy and energy spread of $\pm$ 2 keV and 1 keV, respectively.

For the measurement of the $E_R = 144$ keV resonance, the proton beam was provided solely by 1 MV JN Van de Graaf accelerator at LENA. A schematic of LENA is shown

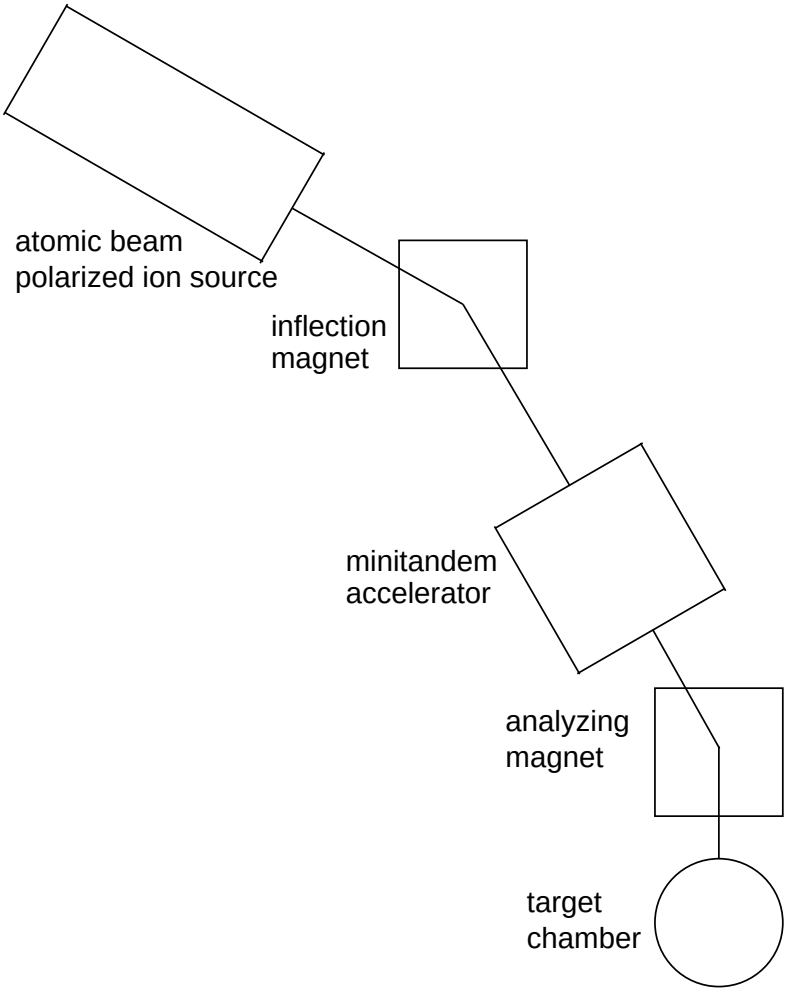

Figure 3.1: Schematic of the beam line used for the coincidence tests and for the ^{23}Na(p,α)^{20}Ne E_R = 338 keV resonance strength measurement. Figure is not to scale.

in Fig 3.2. The 200 kV ECR ion source was not used in this experiment.

3.2 Detectors and electronics

3.2.1 ^{23}Na(p,α)^{20}Ne

The experimental setup used for the measurement of the E_R = 338 keV resonance strength in ^{23}Na(p,α)^{20}Ne is shown in Fig. 3.3. The proton beam entered the scattering chamber through a 3-mm–diameter collimator, passed through the transmission target, and was stopped $\approx$ 1.5 m away on a tantalum beam stop located outside of the

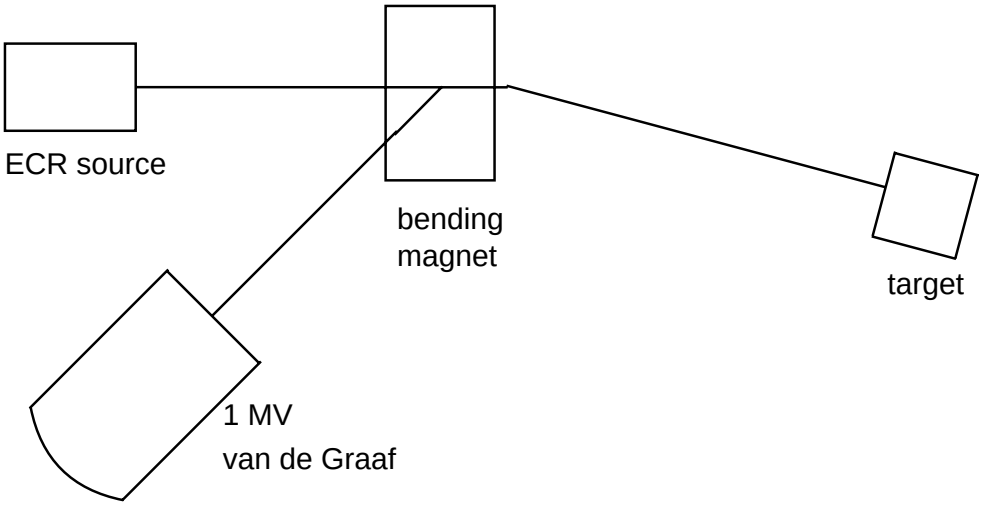

Figure 3.2: Schematic of the Laboratory for Experimental Astrophysics (LENA). Figure is not to scale.

chamber. Proton beam intensities on target were typically 80–300 nA. The scattering chamber with target ladder was electrically insulated from the beam line and the entrance collimator. Emission of secondary electrons was suppressed by using anti–scattering slits and a permanent magnet, located behind and around the collimator, respectively. The scattering chamber together with the target ladder and beam stop acted as a Faraday cup for measuring the total current passing through the target.

For this measurement elastically scattered protons were detected with a 100 μm thick ion–implanted Si detector. A 0.8 mm diameter aperture was placed in front of the detector at a distance of 10.1 cm from the target. The energy calibration and resolution of the detector were obtained by measuring protons elastically scattered from a thin Au transmission target. The energy resolution was ≈ 10 keV. The detector angle was fixed at $\theta_p = 155^\circ$ with respect to the beam direction, except for the angular distribution measurements. The error in detector angle is estimated to be $\approx 1^\circ$ [Pow99].

The α–particles were detected in a 1000 μm silicon surface–barrier detector with an active area of 450 mm^2. A 2.2 μm thick Havar foil (CrCoNi alloy) was placed in front of the detector in order to prevent the large number of elastically scattered protons from reaching the counter. The detector was mounted at a distance of 4.2 cm from the target and the angle was fixed at $\theta_\alpha = 140^\circ$ with respect to the beam

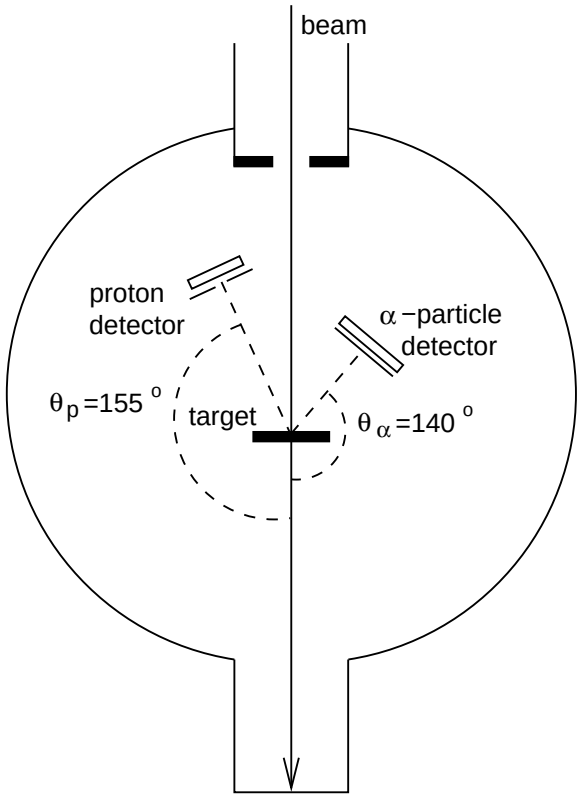

Figure 3.3: Schematic diagram of the experimental setup used for the ^{23}Na(p,α)^{20}Ne resonance strength measurement. Figure is not to scale.

direction. Throughout the experiments, dead times and amplifier gain stabilities were monitored with a precision pulse generator.

3.2.2 Coincidence Tests

The ^{26}Mg(p,γ)^{27}Al reaction was used as a test of the coincidence technique. The target chamber and detectors are shown in Fig 3.4. The proton beam entered the chamber through a collimator and was focused into a profile of about 5 mm diameter on target. The chamber was electrically insulated from the beam line and the entrance collimator. The magnesium beamstop target was directly water cooled and mounted at an angle of 90° with respect to the beam direction. A liquid–nitrogen cooled copper tube was placed between the collimator and the target to minimize carbon deposition on the target. Target and chamber formed a Faraday cup for charge integration and

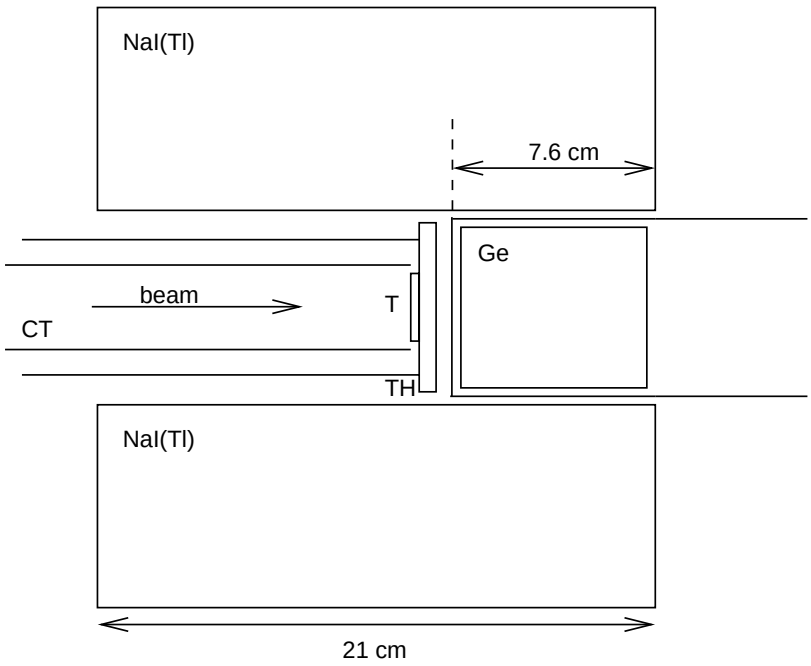

Figure 3.4: Cross–sectional view of the setup used in the ^{26}Mg(p,γ)^{27}Al measurement. Germanium detector (Ge), target (T), target holder (TH) and copper tube (CT) are located inside the NaI(Tl) annulus. The distance between the target and the front face of the germanium detector is 1.9 cm. Figure is not to scale

a negative voltage (-300 V) was applied to the copper tube to suppress secondary electron emission from the target. The pressure in the chamber was about 1×10^{-6} Torr.

For these tests, a high–purity germanium detector with a crystal length and diameter of 93 and 90 mm, respectively, was selected for the primary counter. The Ge detector has an active volume of 582 cm^3 which corresponds to a relative efficiency of 140%. The energy resolution was 3.0 keV at $E_\gamma = 1.33$ MeV. The detector was placed at an angle of $\theta_\gamma = 0^o$ with respect to the beam direction at a front-face-to-target distance of 1.9 cm. An accurate energy calibration was obtained by using γ–ray lines from a ^{56}Co source and from the ^{26}Mg(p,γ)^{27}Al reaction ($E_R = 292$, 339 keV [End90]). Full–energy peak efficiencies for the germanium detector are presented in Ch. 4.

The secondary counter consisted of a NaI(Tl) annular detector which surrounded the target and the germanium detector (Fig. 3.4). The annulus has an outer and inner diameter of 23 and 11 cm, respectively, and a crystal length of 21 cm, and is divided

lengthwise into four optically separated sections, each viewed by a photomultiplier tube. The energy resolution was 18% at $E_\gamma = 0.66$ MeV for each segment and about 20% for the energy sum. Total γ–ray efficiencies for the NaI(Tl) detector are discussed in Ch. 4.

A schematic of the electronics used for the coincidence tests is shown in Fig. 3.5. The Ge preamplifier signal was fed into both a spectroscopy amplifier and a timing filter amplifier (TFA). The unipolar output of the spectroscopy amplifier with a shaping time of 6.0 μs provided the energy signal to the ADC. The output of the TFA was connected to a constant fraction discriminator (CFD) and the resulting timing signal was used to generate the gate for the ADC and to provide the start pulse for a time-to-digital converter (TDC) with a time range of 800 ns. The threshold of the discriminator was set to a value corresponding to a γ–ray energy of about 120 keV. Event rates in the Ge spectra were typically $\leq$300 counts/s.

The segmented NaI(Tl) annulus was used as a single detector with the photomultiplier signals connected in parallel. The summed signal was passed through a spectroscopy amplifier with a shaping time of 0.5 μs to an ADC, as well as through a TFA that was connected to a CFD. The resulting timing signal, delayed by 200 ns, provided the stop for the TDC. The discriminator threshold corresponded to a γ–ray energy of 250 keV.

The timing signal of the Ge detector represented the master trigger. A time resolution of about 15 ns was obtained for Ge–NaI(Tl) coincidences with a ^{60}Co source. Data acquisition was done with CAMAC ADC, CAMAC TDC and VME onboard computer. Events were monitored on–line and stored on disk in event-by-event mode for off-line analysis.

3.2.3 ^{23}Na(p,γ)^{24}Mg

Measurement of the strength of the $E_R = 144$ keV resonance in ^{23}Na(p,γ)^{24}Mg was completed at LENA using a setup nearly identical to that described above. The target chamber and detectors are shown in Fig. 3.6.

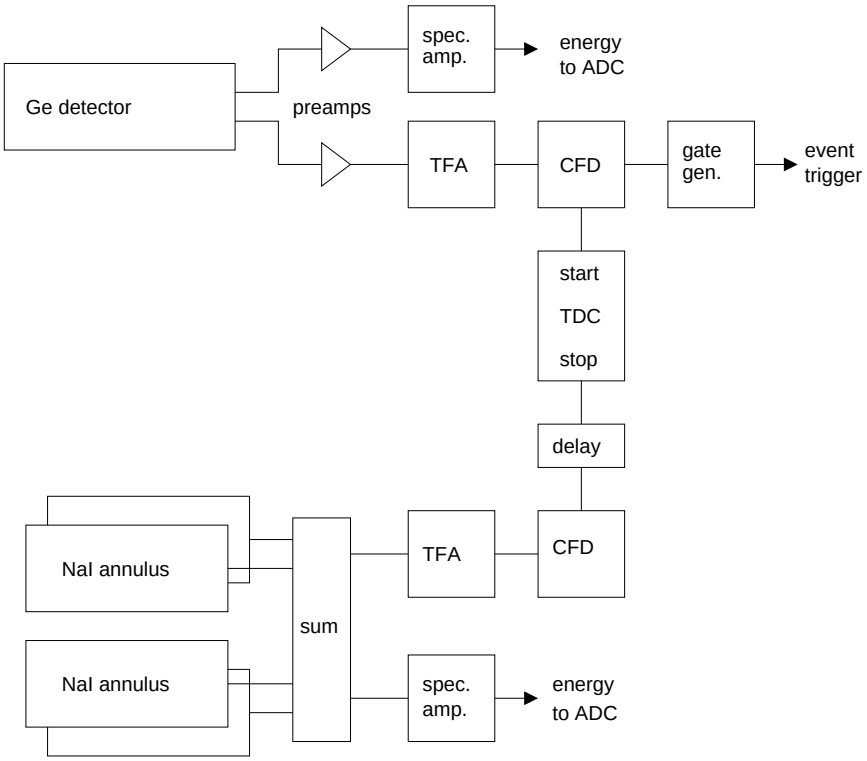

Figure 3.5: Schematic of the electronics used in the ^{26}Mg(p,γ)^{27}Al measurement.

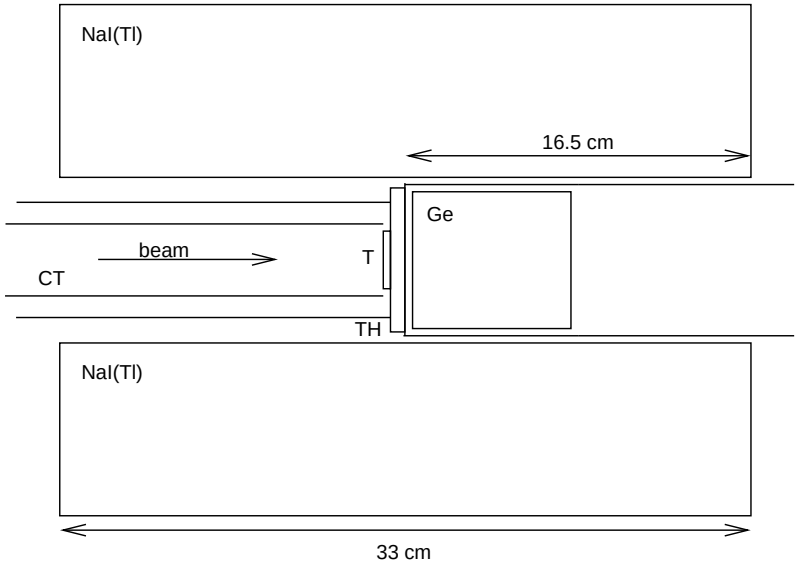

Figure 3.6: Cross-sectional view of the setup used in the ^{23}Na(p,γ)^{24}Mg measurement at LENA. Germanium detector (Ge), target (T), target holder (TH), and copper tube (CT) are located inside the NaI annulus. The target holder was flush with the Germanium detector for this experiment. Figure is not to scale.

The same germanium detector described above for the coincidence technique tests was used as the primary counter for this experiment. Again the detector was placed at an angle of $\theta_\gamma = 0^o$ with respect to the beam direction, but the distance from front face to target was only 0.3 cm. Energy calibration was obtained by using γ–ray lines from a ^{56}Co source. Full–energy peak efficiencies for the germanium detector are presented in Ch. 6.

The secondary counter consisted of a NaI annular detector which surrounded the target and the germanium detector (Fig. 3.6). This annulus, purchased after the ^{26}Mg+p tests, has an outer and inner diameter of 11.4 and 38 cm, respectively, and a crystal length of 33 cm, and is divided lengthwise into sixteen optically separated sections, each viewed by a photomultiplier tube. The energy resolution was 7.5% at $E_\gamma = 0.66$ MeV for each segment and about 8% for the energy sum. Total γ–ray efficiencies for this NaI detector are discussed in Ch. 6.

The electronics used for this measurement were similar to those described above for the coincidence technique tests. For this experiment the TDC was replaced with a TAC (time-to-analog converter), and the time and energy signals were fed into a CAEN VME ADC.

3.3 Target production

For the ^{26}Mg+p coincidence tests, a magnesium beamstop target was prepared by evaporating ^{26}Mg onto a 0.5-mm-thick tantalum backing. The evaporation was done using ^{26}Mg enriched (99.8%) MgO. The MgO powder was thoroughly mixed with zirconium fine powder in a proportion of about 1:6 and placed in a previously outgassed tantalum dimple boat. Reagent grade ethyl alcohol was added to the powder mixture to insure good heat contact between the MgO and zirconium [Tak66]. The boat was placed in a vacuum evaporator and gradually heated. After outgassing, the reduction occurs at a temperature of ≈ 1200°C. The target thickness was first estimated during the evaporation with a crystal thickness monitor and then determined to be about 5 keV at a bombarding energy of $E_p = 340$ keV. The target was checked frequently and

was found to be stable throughout the course of the experiment.

For the measurement of the $E_R = 144$ keV resonance in $^{23}Na(p,\gamma)^{24}Mg$, a sodium beamstop target was used. The target backings were again 0.5-mm-thick tantalum, like those described above. The tantalum backings have a rough surface and contain contaminants such as carbon and boron. To minimize background contributions from these contaminants and to smooth the surface, the tantalum backings were etched before the evaporation. The etching process allowed for removal of scratches and surface grease, and gave the tantalum backings a smooth and polished surface.

The procedure for etching used in the present work can be found in Giesen [Gie92]. What follows is a brief description of that procedure. The recipe for chemically polishing sheets of tantalum consists of five parts 95% sulfuric acid (H_2SO_4), two parts 70% nitric acid (HNO_3), and 2 parts 48% hydrofluoric acid (HF). The etching process releases dangerous fumes and must be performed under a hood, with an emergency shower and eyewash nearby. The 300 mL Teflon beaker used to mix the acids was submerged in an ice bath throughout the procedure. The acids were mixed in the following sequence and quantities: 70 mL of 95% H_2SO_4, 30 mL of 70% HNO_3, and 30 mL of the 48% HF. This amount of liquid was enough to completely submerge a tantalum backing. The backings were handled with long, Teflon coated tweezers and slowly dipped three times, 20 seconds each time. One charge of the mixture is able to etch four to five backings. After etching, the backings were rinsed with distilled water and methanol. The backings were heated and outgassed in a vacuum of $\leq 3\mu$Torr.

Sodium was evaporated onto the etched tantalum backings. A variety of sodium compounds were tested in beam and the results of those tests are quantitatively summarized in Table 3.1. The most stable compound was found to be sodium tungstanate (Na_2WO_4), and therefore these targets were used for the $E_R = 144$ keV resonance strength measurement.

For the measurement of the $E_R = 338$ keV resonance strength in $^{23}Na(p,\alpha)^{20}Ne$, a carbon backing foil of 20 $\mu g/cm^2$ thickness was floated on water and mounted on a stainless steel frame with a 1-cm diameter hole. NaCl was evaporated from a tantalum boat onto this foil under vacuum. The resulting target thickness was ≈ 5.0

Sodium compound	Effective stopping power at E_p = 140 keV ($eV/(1e^{15}/cm^2)$)	Stability of beamstop targets
Sodium chloride (NaCl)	48.84	very unstable
Sodium bromide (NaBr)	54.08	unstable
Sodium tungstanate (Na_2WO_4)	66.88	stable
Sodium titanate ($Na_2Ti_3O_7$)	108.72	unstable

Table 3.1: Comparison of sodium compounds for target fabrication.

keV at proton beam energies of $E_p \approx 340$ keV. The NaCl transmission target was tested frequently during the course of the experiment by monitoring the spectrum of backscattered protons. The target could withstand beam currents of up to 300 nA over several hours without noticeable deterioration in thickness or yield.

Chapter 4

$\gamma\gamma$-coincidence measurements

4.1 Motivation

As mentioned in Sec. 1.3, the detection of low-energy resonances in proton or α–particle capture reactions is challenging because of Coulomb barrier penetrability considerations. Such resonances frequently dominate thermonuclear reaction rates at temperatures of astrophysical interest, and substantial efforts are necessary in order to detect a very small capture γ–ray yield in the presence of relatively large background contributions from various sources. The weakest (p,γ) resonance ever observed was measured in the ^{26}Mg+p reaction [Ili90]. The experimental technique employed in this work is typical of many similar investigations and is summarized as follows. An intense proton beam ($\approx$ 500 μA) at a bombarding energy of $E_p \approx 0.15$ MeV was incident on a Mg beamstop target, which was directly water-cooled. A germanium detector with an active volume of 145 cm^3 was positioned as close as possible to the target in order to maximize counting efficiency. Target chamber and detector were shielded with lead of about 10 cm thickness, covering the full solid angle except for the direction of the proton beam. A plastic scintillator was placed outside of the lead shielding in order to suppress cosmic-ray background contributions. With the setup described above, a strength of $\omega\gamma \approx 8{\cdot}10^{-8}$ eV [Ili90] was measured for the $E_R = 155$ keV resonance in ^{26}Mg+p.

For detection of even weaker resonances, several aspects of the setup could be im-

proved. For example, a larger γ–ray detector and a higher ion beam intensity would increase the capture γ–ray yield. Ultimately, however, γ–ray background contributions from various sources will limit the sensitivity of the setup. Therefore, effective background suppression is a necessary condition for the observation of weak resonances with strengths in the range of $\omega\gamma = 10^{-10}$ – 10^{-8} eV.

The background arises from several sources and various background-suppression methods have been described previously [Heu95]. For example contributions from terrestrial radioactivity can be reduced by surrounding the detector with a low-activity lead shield [Ste68, Mal84]. Radioimpurities in the detector itself are suppressed by careful selection of construction materials [Bro85]. Background from radon and progenitors is reduced by replacing the air surrounding the setup with nitrogen [Heu86]. Events from cosmic ray muons and neutrons are partially rejected either by using anticoincidence detectors (e.g., plastic scintillators [Mül90]) or by operating the γ–ray detector deep underground [Kay72, Kam86, Heu91]. Compton background can also be reduced with anticoincidence detectors, such as NaI(Tl) [Coo72]. Finally, the target has to be prepared carefully in order to minimize background contributions from contaminant reactions [Gov60].

It is interesting to note that many capture reactions of astrophysical interest have Q-values of several MeV. Therefore, the populated threshold levels can decay to the ground state via $\gamma\gamma$-cascades. For example, consider the level scheme of ^{27}Al shown in Fig. 4.1. An inspection of primary γ–ray branching ratios for resonances below $E_R = 3.0$ MeV in the ^{26}Mg+p reaction ($Q_{p\gamma} = 8.27$ MeV) reveals that the majority of γ–ray decays proceed to the five lowest-lying levels in ^{27}Al with excitation energies of $E_x < 3.0$ MeV [Ili90, Smi82]. Similar arguments hold for (p,γ) reactions on other target nuclei in the sd-shell [End90, End98]. Consequently, it should be possible to reduce the background substantially via $\gamma\gamma$–coincidence counting techniques.

In the present work the performance of a coincidence setup consisting of a germanium detector and a sodium-iodide annulus was tested. Similar techniques have been described previously, for example, in Refs. [Kam86, Coo72, Bra75, Mas91]. However, these measurements were concerned with radioenvironmental work or weak interac-

tion studies, implying γ–ray energies below 2.0 MeV whereas, many astrophysically important capture reactions produce γ rays with energies exceeding 10 MeV. This setup was tested by measuring the E_R = 227 keV resonance in the ^{26}Mg(p,γ)^{27}Al reaction which has a well-known γ–ray decay scheme. However, its measured strength of $\omega\gamma = (5 \pm 2)\cdot 10^{-5}$ eV is small and proton beam intensities of several hundred μA were required in previous studies [Ili90, Buc80]. This resonance was detected in the present work by using a coincidence setup with a proton beam intensity of only 1.5 μA.

The results presented in this chapter have recently been published (see Rowland *et al.* [Row02a]). Sec. 4.2 describes the experimental procedure and results, including germanium and NaI(Tl) detection efficiencies. Studies of γ–ray background and suggestions for possible improvements are discussed in Sec. 4.3. A summary of this work and its implications are given in Sect 4.4. Throughout this chapter, all quantities are given in the laboratory system unless mentioned otherwise.

4.2 Experimental procedure

4.2.1 General considerations

As described in 4.1, for many reactions of astrophysical interest the majority of primary γ–ray transitions proceed to the first few excited levels in the compound nucleus. For the ^{26}Mg(p,γ)^{27}Al reaction these levels are located at energies of $E_x < 3.0$ MeV, implying that most primary and secondary γ–ray transitions will have energies above and below E_γ = 3.0 MeV, respectively (Fig. 4.1). Since the full-energy peak efficiency decreases with increasing γ–ray energy, the Ge detector will register more secondary than primary transitions. Furthermore, the higher-energy primary γ–ray peaks will be Doppler-broadened. However, since natural γ–ray background dies away at energies above 2 MeV, its contribution will be much smaller in the region of the primary transitions. Nevertheless, the Ge detector is expected to be more sensitive for secondary compared to primary γ–ray transitions if the low-energy background can

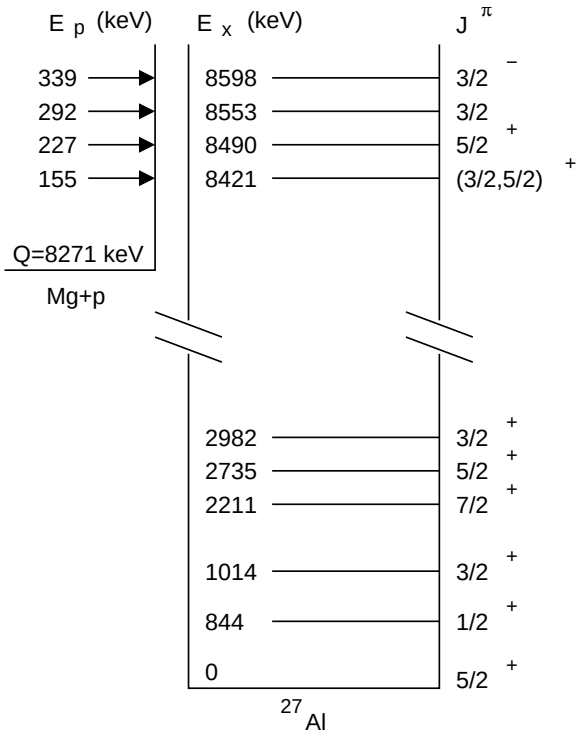

Figure 4.1: Level diagram of ^{27}Al. Low-lying levels and proton threshold states are shown together with corresponding resonances. Energies and J^{π} values are adopted from [End90] and [End98]

be reduced significantly. In the present work Ge spectra were measured in coincidence with γ–rays detected by the NaI(Tl) counter. Requiring a NaI(Tl) energy window of $E_\gamma > 3.0$ MeV will strongly reduce the background of the coincident Ge spectrum in the region of the secondary γ–ray transitions below $E_\gamma = 3.0$ MeV, while a NaI(Tl) window of $E_\gamma < 3.0$ MeV will suppress the Ge detector background in the range of the primary transitions above $E_\gamma = 3.0$ MeV.

It is possible to estimate a minimum detectable resonance strength, $\omega\gamma_{min}$, which is an inverse measure of the sensitivity of the detection apparatus. The resonance strength is related to the thick-target yield Y by the expression [Gov59]

$$\omega\gamma \;=\; \frac{2\epsilon}{\lambda^2}\; Y, \tag{4.1}$$

where λ is the center-of-mass de Broglie wavelength of the incident proton and ϵ is the stopping power, both evaluated at the resonance energy. The thick-target yield is experimentally given by

$$Y \;=\; \frac{N_\gamma}{N_p f(B_\gamma, \eta_\gamma, W_\gamma)}, \tag{4.2}$$

with N_γ, B_γ, η_γ and W_γ representing the number of observed γ–rays, the branching ratio, the detection efficiency and the angular distribution, respectively, of the γ–ray transitions under consideration. For singles germanium detector spectra, the function f is simply given by the product $f = B_\gamma \eta_\gamma W_\gamma$, whereas for coincidence germanium spectra f will depend on the resonance decay scheme and the Ge and NaI(Tl) detection efficiencies (Sec. 4.2.3.) The quantity N_p denotes the total number of incident protons. The minimum detectable number of γ–ray counts after background subtraction in the peak of interest can be approximated by [Deb88]

$$N_{\gamma,min} \;\approx\; 5.4 + 3.3\sqrt{2N_b}, \tag{4.3}$$

where N_b is the number of background counts as determined from either side of the expected peak of interest. Poisson statistics are assumed for the background. The quantity N_b can be expressed as [Deb88]

$$N_b \;= n\ \overline{B}\ \approx 1.2\ \Delta E_\gamma\ \overline{B}. \tag{4.4}$$

Here $\overline{B}$ is the average background per channel, n is the number of channels included in the γ–ray peak, and ΔE_γ is the FWHM (in channels) of the peak. Substitution of Eqs. 4.2 - 4.4 into Eq. 4.1 yields

$$\omega\gamma_{min} \;\approx\; 10.6\ \frac{\epsilon}{\lambda^2}\ \ \frac{1.0 + \sqrt{\Delta E_\gamma\ \overline{B}}}{N_p\ f(B_\gamma, \eta_\gamma, W_\gamma)}. \tag{4.5}$$

This estimate of the minimum detectable resonance strength $\omega\gamma_{min}$ is nearly proportional to the square root of the background counts and the detector resolution. In the following sections, Eq. 4.5 is used in order to compare sensitivities for various modes of operation.

4.2.2 Singles and coincidence γ–ray spectra

Figs. 4.2– 4.4 show germanium spectra for the weak E_R = 227 keV resonance in ^{26}Mg(p,γ)^{27}Al. For each spectrum the accumulated charge amounted to 0.05 C, corresponding to a running time of about 10 hours with 1.5 μA proton beam intensity.

Part of a singles germanium detector spectrum is shown in Fig. 4.2(a). The germanium detector was unshielded. The spectrum displays the energy range $E_\gamma < 3.0$ MeV of expected secondary γ–ray transitions in ^{27}Al. The observed γ–ray peaks are due to various environmental background contributions. No peaks are seen at energies of secondary γ–ray transitions expected from the ^{26}Mg+p reaction. Fig. 4.2(b) shows the same γ–ray energy region as before, but the spectrum was obtained by shielding the germanium detector with lead of 5-cm thickness. Compared to the unshielded detector, the background is reduced by about one order of magnitude, but still no peaks are detected at the energies of expected secondary γ–ray transitions. Fig. 4.2(c) was obtained by measuring the germanium detector spectrum in coincidence with γ–rays detected in the NaI(Tl) annulus. An energy window of E_γ = 3.0–9.0 MeV was selected in the NaI(Tl) spectrum, corresponding to the energy region of primary γ–ray transitions in ^{27}Al. No active or passive shielding was used in this case. As compared to the unshielded singles germanium spectrum, the continuous γ–ray background is reduced by more than three orders of magnitude and the γ–ray peaks arising from environmental radioactivity have disappeared. The resonant γ–ray transitions of the second and third excited states in ^{27}Al at E_x = 1014 and 2211 keV, respectively, are now clearly observed. Although random coincidences have been subtracted from the spectrum, their number amounts only to 0.2% of the total counts in the energy region shown. The remaining background shown in Fig. 4.2(c) is primarily induced by cosmic radiation and is investigated in Sec. 4.3.

Most γ–rays from environmental sources have typical energies below E_γ = 3.0 MeV. These events will not give rise to $\gamma\gamma$-coincidences in the present setup if an energy window above E_γ = 3.0 MeV is selected in the NaI(Tl) spectrum. Consequently, the background in the low-energy part of the germanium coincidence spectrum is

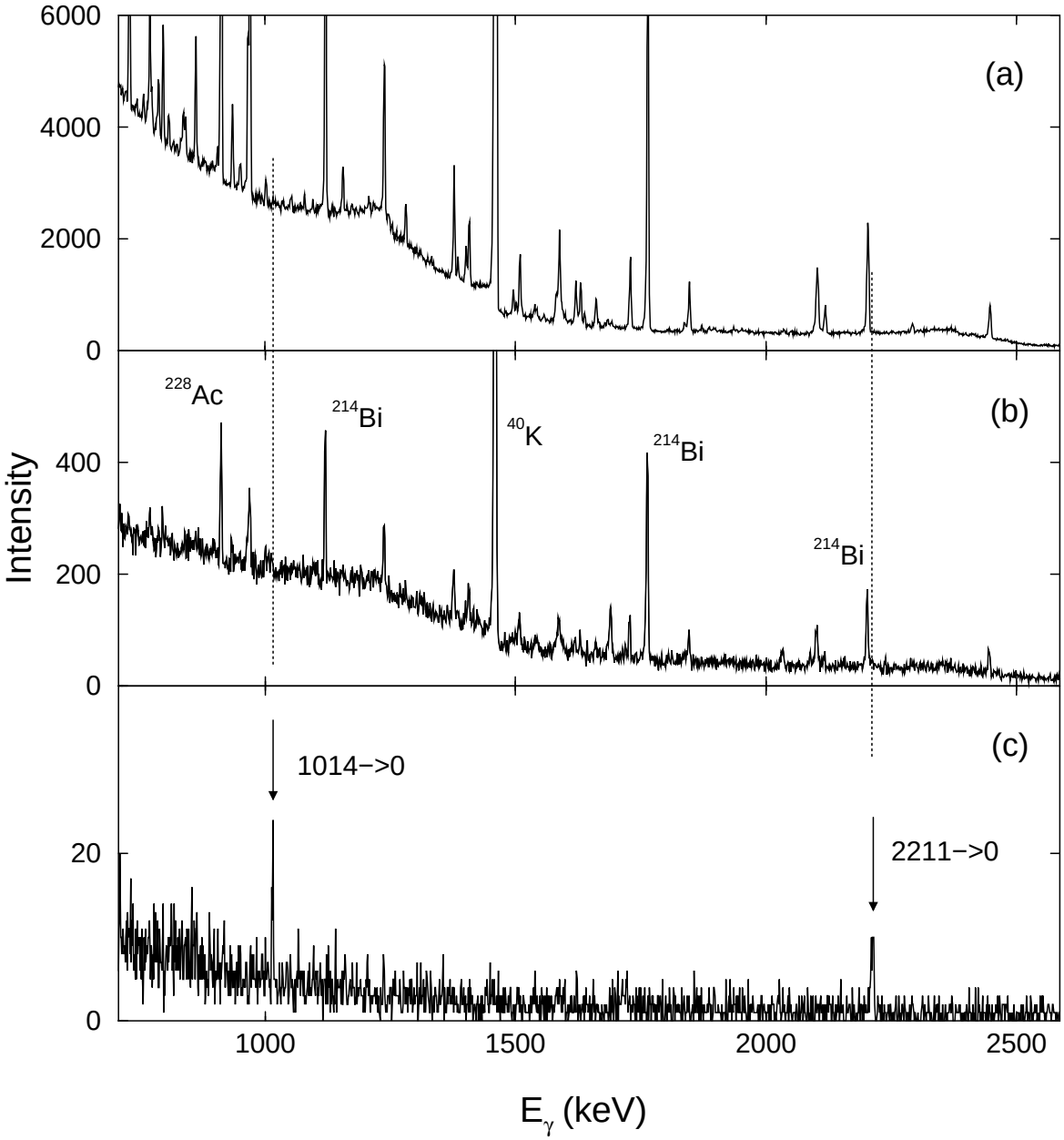

Figure 4.2: Germanium detector spectra for the $E_R = 227$ keV resonance in ^{26}Mg+p in the region E_γ^{Ge} = 800-2500 keV, measured with a proton beam intensity of $I_p \approx 1.5$ μA and a running time of 10 hours: (a) singles spectrum without lead shield; (b) singles spectrum with 5cm of lead shielding; (c) coincidence spectrum (without lead shield) obtained for an Na(Tl) energy window of E_γ^{NaI} = 3.0 - 9.0 MeV. All observed γ–ray lines in (a) and (b) arise from room background contributions. Only the strongest background lines are labeled in (b). The ground state transitions of the second and third excited state in ^{27}Al are clearly seen in (c).

strongly reduced. If secondary ^{27}Al transitions peaks are observed in the germanium coincidence spectrum, then corresponding primary γ–rays interacted via photoelectric effect, Compton scattering or pair production with the NaI(Tl) annulus, thereby depositing an energy of at least 3.0 MeV. Note that the observed signal-to-noise ratio in Fig. 4.2(c) is rather sensitive to the lower limit of the selected energy window in the NaI(Tl) spectrum. If a too small value for the lower limit is chosen (say, a few hundred keV), then γ–rays from environmental sources will Compton scatter from one counter to the other and will contribute to the coincidence background. If, on the other hand, a too large value is selected (say, several MeV), then the number of observed resonant secondary γ–rays in the germanium coincidence spectrum will decrease as a result of a reduced total NaI(Tl) detection efficiency (Sec. 4.2.3) for resonant primary ^{27}Al transitions. The effect is illustrated in Fig. 4.3, showing coincidence germanium spectra for the same energy region as displayed in Fig. 4.2, versus the lower limit of the NaI(Tl) energy window. In the present work, an optimum signal-to-noise ratio in the germanium coincidence spectrum was obtained by using a value of about 3.0 MeV, Figs. 4.2(c) and 4.3(b), for the lower limit of the NaI(Tl) energy window.

Fig. 4.4(a) displays a singles germanium spectrum for the E_R = 227 keV resonance in ^{26}Mg+p at energies of expected primary transitions above E_γ = 4.0 MeV. The spectrum shows very weak peaks at energies corresponding to the three strongest primary γ–ray branches to ^{27}Al states at E_x = 2211, 2735 and 2982 keV (Fig. 4.1). The spectrum was measured with the unshielded germanium detector, but in this energy region no noticeable difference was observed when the germanium detector was shielded with lead of 5-cm thickness. Fig. 4.4(b) shows a corresponding germanium coincidence spectrum, obtained without active or passive shielding. All events shown in the spectrum have been selected according to the condition that the sum of energies deposited in germanium and NaI(Tl) detector does not exceed substantially the excitation energy of the compound nucleus state populated in the capture reaction, i.e., 0.25 MeV $< E_\gamma^{Ge} + E_\gamma^{NaI} <$ 9.0 MeV. The observed peak corresponds to the primary γ–ray transition to the E_x = 2735 keV level in ^{27}Al. Clearly, the coincidence requirement improves the signal-to-noise ratio, although it is a far smaller improvement than

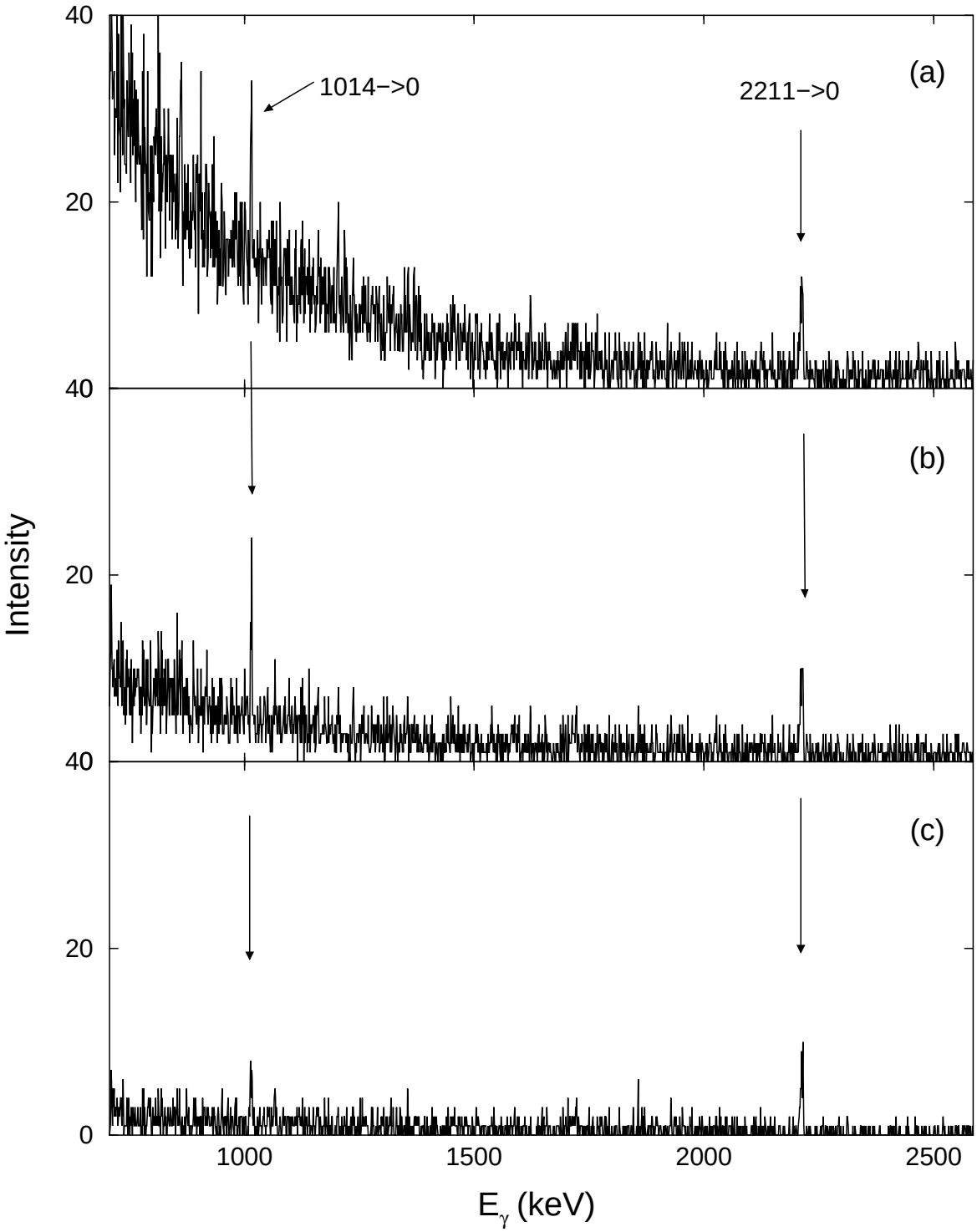

Figure 4.3: Germanium detector spectra for the region E_γ^{Ge} = 800–2500 keV versus different NaI(Tl) energy windows: (a) E_γ^{NaI} = 2.5–9.0 MeV; (b) E_γ^{NaI} = 3.0–9.0 MeV; (c) E_γ^{NaI} = 5.0–9.0 MeV. Note (b) is identical to Fig. 4.2(c).

seen in Fig. 4.2. The γ–ray background displayed in Figs. 4.4(a) and 4.4(b) is most likely induced by cosmic radiation and is investigated in Sec. 4.3.

The information presented in Figs. 4.2– 4.4 has been used in order to estimate $\omega\gamma_{min}$ values for a hypothetical ^{26}Mg+p resonance located at $E_R = 0.23$ MeV. It was assumed that the compound nucleus level decays to the ground state through an intermediate level at $E_x = 1$ MeV via a two-γ–ray cascade. The numerical results have been obtained by using detection efficiencies measured in the present work (see Sec. 4.2.3). Isotropic angular distributions have been assumed for the primary and secondary γ–ray transition. Relative detection sensitivities for various modes of operation are displayed in Fig. 4.5. The vertical axis shows the factor $F = (1 + \sqrt{\Delta E_\gamma \overline{B}})/\eta_\gamma^{Ge,P}$ of Eq. 4.5, with $\eta_\gamma^{Ge,P}$ being the full-energy peak efficiency of the Ge detector. The numbers 1–5 on the horizontal axis correspond to the spectra shown in Figs. 4.2(a), 4.2(b), 4.2(c), 4.4(a) and 4.4(b), respectively. It can be seen that the largest sensitivity, i.e., the smallest value of F, is obtained for observing secondary γ–rays in the germanium detector in coincidence with primary γ–rays measured in the NaI(Tl) counter. For this case, we obtain a value of $\omega\gamma_{min} \approx 7{\cdot}10^{-6}$ eV for the minimum resonance strength detectable with our setup, a proton beam intensity of $I_p \approx 1.5$ μA, and a running time of about 10 hours. The results shown in Fig. 4.5 depend on, among other things, the specific capture reaction under investigation, the bombarding energy chosen, and the γ–ray decay scheme of the resonance, but nevertheless provide useful estimates for purposes of comparison.

4.2.3 Detection efficiencies

The calculation of resonance strengths from γ–ray peak intensities observed in the singles and coincidence germanium spectra requires reliable detection efficiencies as input. It follows from the discussion in previous sections that the quantities of primary interest here are the absolute full-energy peak efficiency of the Ge detector and the absolute total efficiency of the NaI(Tl) annulus.

For the germanium detector, absolute full-energy peak efficiencies in the range

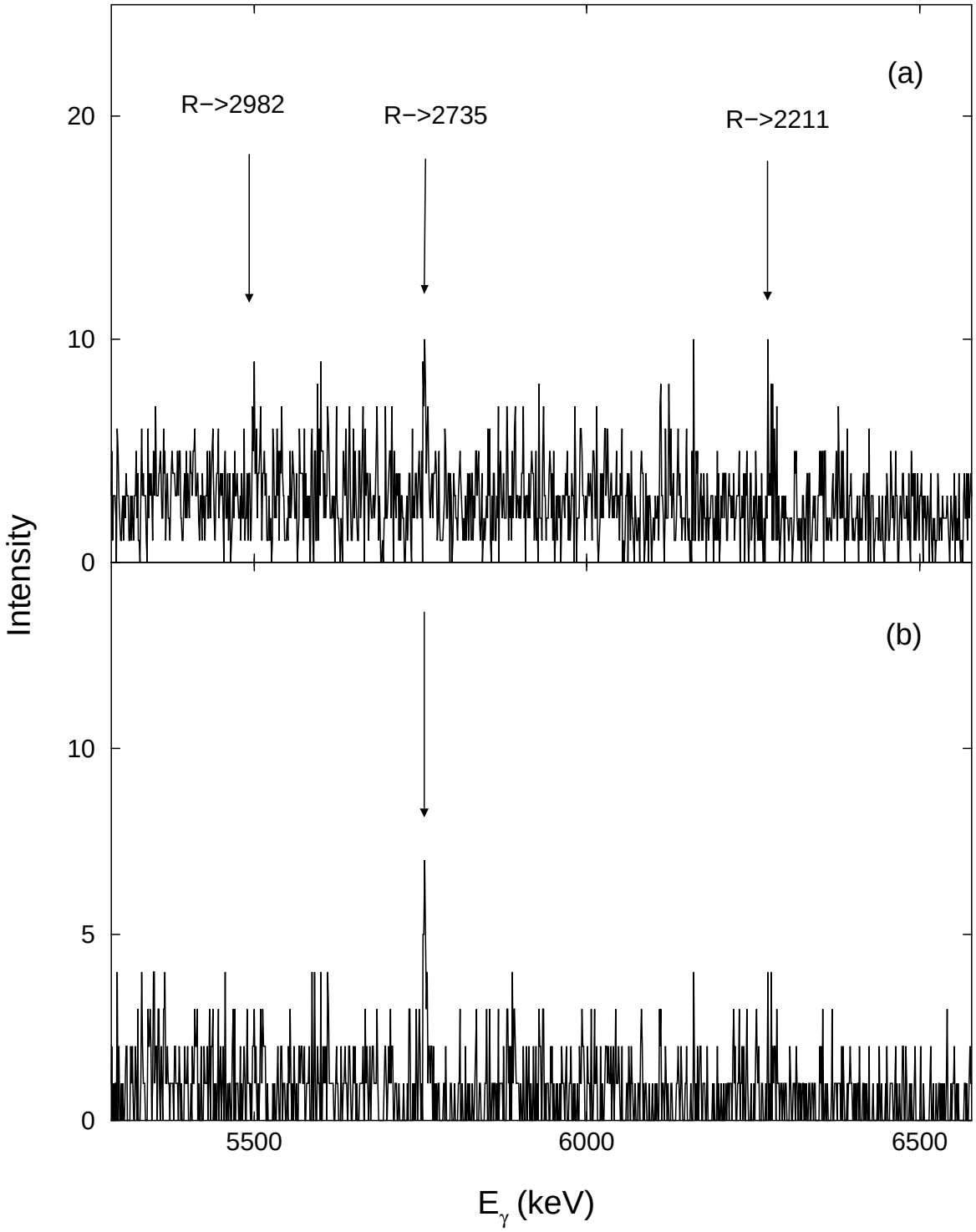

Figure 4.4: Germanium detector spectra for the $E_R = 227$ keV resonance in ^{26}Mg+p in the region $E_\gamma^{Ge} = 5400$–6500 keV, measured with a proton beam intensity of $I_p \approx 1.5\mu$A and a running time of 10 hours: (a) Singles spectrum without lead shield. Very weak γ–ray lines are observed corresponding to the strongest primary transitions in ^{27}Al; (b) Coincidence spectrum (without lead shield) obtained with the condition 0.25 MeV $< (E_\gamma^{Ge} + E_\gamma^{NaI}) < 9.0$ MeV. The primary transition to the fourth excited state in ^{27}Al is clearly seen.

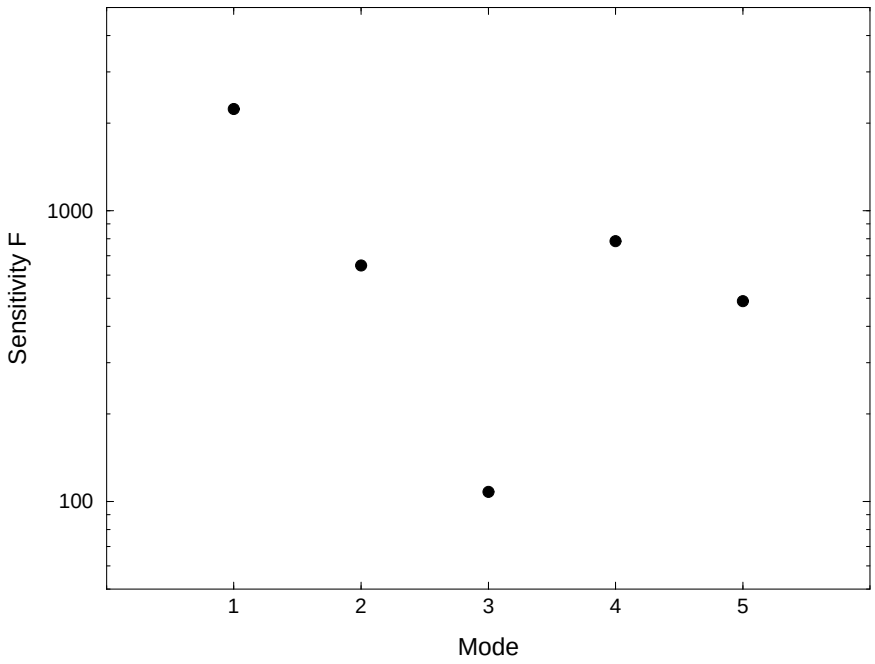

Figure 4.5: Detection sensitivity for a hypothetical ^{26}Mg+p resonance at $E_R = 0.23$ MeV, decaying to the ground state through an intermediate level at $E_x = 1$ MeV via a two-γ–ray cascade. The vertical axis displays the factor $F = (1+\sqrt{\Delta E_\gamma \overline{B}})/\eta_\gamma^{Ge,P}$ of Eq. 4.5. On the horizontal axis, the numbers 1, 2, 3, 4 and 5 indicate the mode of operation corresponding to the spectra shown in Figs. 4.2(a), 4.2(b), 4.2(c), 4.4(a) and 4.4(b), respectively.

$E_\gamma = 0.8$–12.0 MeV were measured by using a calibrated ^{56}Co source as well as resonant γ–rays from the reaction ^{27}Al(p,γ)^{28}Si (E_R = 992, 1317 keV [End90]). The latter calibration runs were performed with proton beams from the 3-MV KN Van de Graaff accelerator at TUNL. The experimental efficiency values are displayed in Fig. 4.6(a). The results have been corrected for coincidence summing effects (Appendix A), since the germanium detector was located in close geometry to the target (Fig. 3.4).

For the NaI(Tl) annulus, the total efficiency depends on the selected energy window. The two NaI(Tl) windows of primary interest in the present work cover energies of E_γ^{NaI} = 0.25–9.0 MeV and 3.0–9.0 MeV. These windows provide the best signal-to-noise ratios for coincidence germanium spectra in the region of primary and secondary γ–ray transitions in ^{27}Al, respectively (Sec. 4.2.2). Total NaI(Tl) γ–ray efficiencies have been estimated as follows. A γ–ray decay scheme is presented in Fig. 4.7, showing the decay of a compound nucleus state A via a two-γ–ray cascade γ_0-γ_1 in the presence of competing three-γ–ray cascades γ_0-γ_3-$\gamma_{3'}$ and γ_2-$\gamma_{2'}$-γ_1. If the

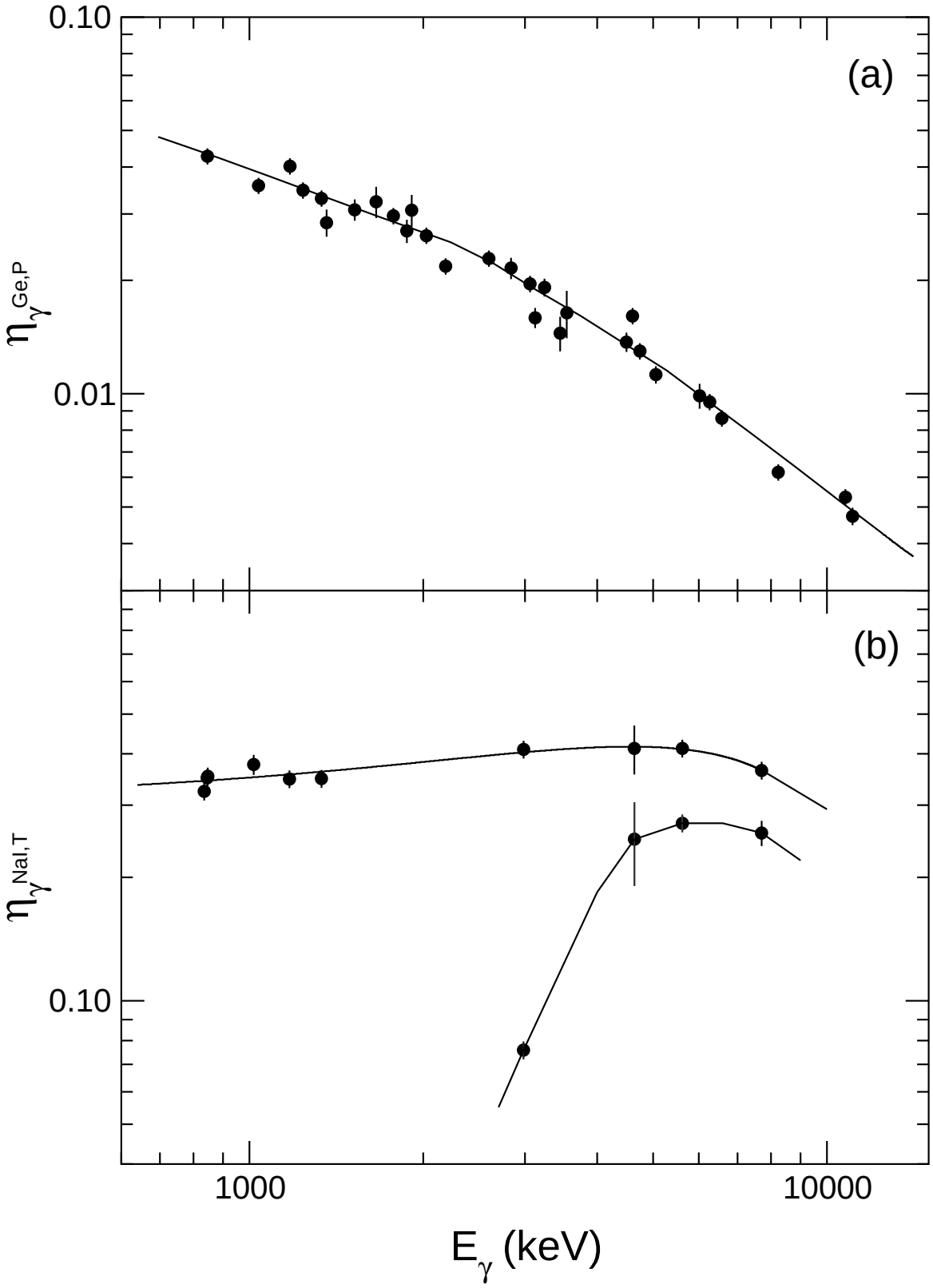

Figure 4.6: (a) Absolute full-energy peak efficiency of germanium detector versus γ–ray energy; (b) absolute total efficiency of NaI(Tl) annulus for energy windows of E_{γ}^{NaI} = 0.25–9.0 MeV (upper curve) and E_{γ}^{NaI} = 3.0–9.0 MeV(lower curve). The solid lines are to guide the eye.

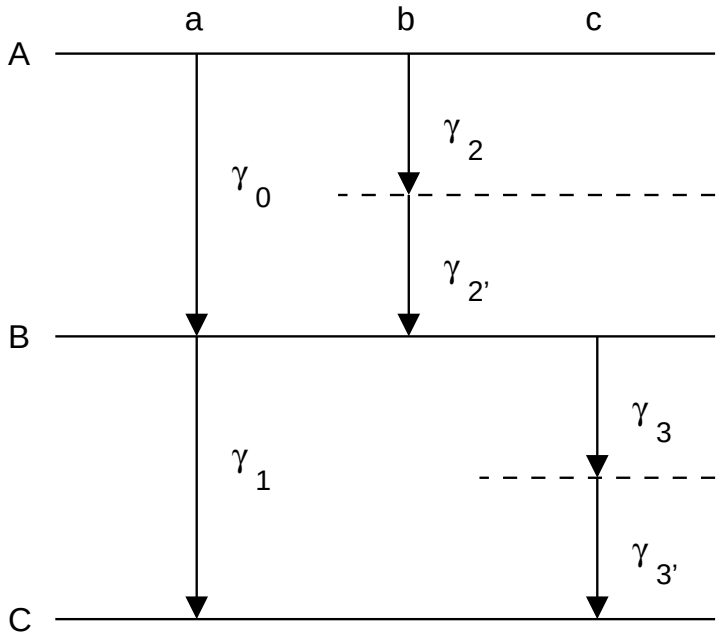

Figure 4.7: A simple decay scheme to illustrate the calculation of absolute total NaI(Tl) detection efficiencies.

level lifetimes are negligible compared to the coincidence resolving time, then the total NaI(Tl) efficiency for the secondary γ–ray γ_1 is given by the ratio of intensities for the corresponding primary γ–ray γ_0 observed in the coincidence and singles germanium spectra,

$$\eta_{\gamma_1}^{NaI,T} = \frac{N_{\gamma_0}^{Ge,coin}}{N_{\gamma_0}^{Ge,sing}} (1 - \eta_{\gamma_1}^{Ge,T}), \tag{4.6}$$

with $\eta_{\gamma_1}^{Ge,T}$ the total germanium detector efficiency for γ–ray γ_1. The term in parenthesis is a correction for coincidence summing in the singles germanium spectrum. The above equation provides a reliable estimate for $\eta_{\gamma_1}^{NaI,T}$ only if the intermediate level B decays to the ground state C with a branching ratio close to 100%, i.e., $B_{\gamma_1} \approx 1$ and $B_{\gamma_3} \approx 0$. Competing cascades γ_2-$\gamma_{2'}$ *feeding* level B have no influence on the result since they are uncorrelated with γ–ray γ_0 observed in the germanium detector. Similarly, the total NaI(Tl) efficiency for the primary γ–ray γ_0 is given by the expression

$$\eta_{\gamma_0}^{NaI,T} = \frac{N_{\gamma_1}^{Ge,coin}}{N_{\gamma_1}^{Ge,sing}} (1 - \eta_{\gamma_0}^{Ge,T}). \tag{4.7}$$

This relation provides reliable results if the intermediate level B is populated only directly from the decaying level A, i.e., $B_{\gamma_2} \approx 0$ or $B_{\gamma_{2'}} \approx 1$. Competing cascades γ_3-$\gamma_{3'}$ *decaying* from level B have no influence on the result since they are uncorrelated with γ–ray γ_1 observed in the germanium detector. The relations discussed above allow an estimate of absolute total NaI(Tl) efficiencies without the use of calibrated γ–ray sources or capture reactions with known radiation yields. The experimental results are shown in Fig. 4.6(b). The values of $\eta_\gamma^{NaI,T}$ were obtained by measuring two strong ^{26}Mg+p resonances at E_R = 339 keV and E_R = 292 keV, and the decay of ^{60}Co. by using Eqs. 4.6 and 4.7 for selected two-γ–ray cascades. Note that the use of three-γ–ray cascades yields more complicated expressions for $\eta_\gamma^{NaI,T}$ because of coincidence summing effects in the NaI(Tl) detector. Therefore, the latter case has been disregarded for the calculation of efficiencies.

The variation of efficiencies with source-detector geometry has also been investigated in the present work. Fig 4.8(a) shows full-energy peak efficiencies at E_γ = 1.33 MeV for the germanium detector, measured with a calibrated ^{60}Co source, versus distance between detector front face and source. All data shown were corrected for coincidence summing effects. The ^{60}Co source was mounted on the target holder in order to take γ–ray absorption effects into account. The vertical dashed line indicates the geometry of the (p,γ) measurements. For the data point at d = 0.7 cm the target holder was in contact with the germanium detector front face. Increasing the distance to only d = 2.5 cm decreases the germanium efficiency by a factor of two. Clearly, for searches of weak resonances it is most important to place the germanium detector as close as possible to the target.

Corresponding results for the NaI(Tl) annulus are shown in Fig. 4.8(b). A calibrated ^{54}Mn source which provides a single γ–ray line at E_γ = 0.84 MeV was used in order to avoid coincidence summing effects. Only events with energies above E_γ = 0.25 MeV were taken into account. The source was placed on the symmetry axis of the annulus at a distance measured from one front face. The vertical dashed line indicates the geometry of the (p,γ) measurements. The data shown by open circles have been measured by using the bare ^{54}Mn source. As expected, the total NaI(Tl) efficiency is

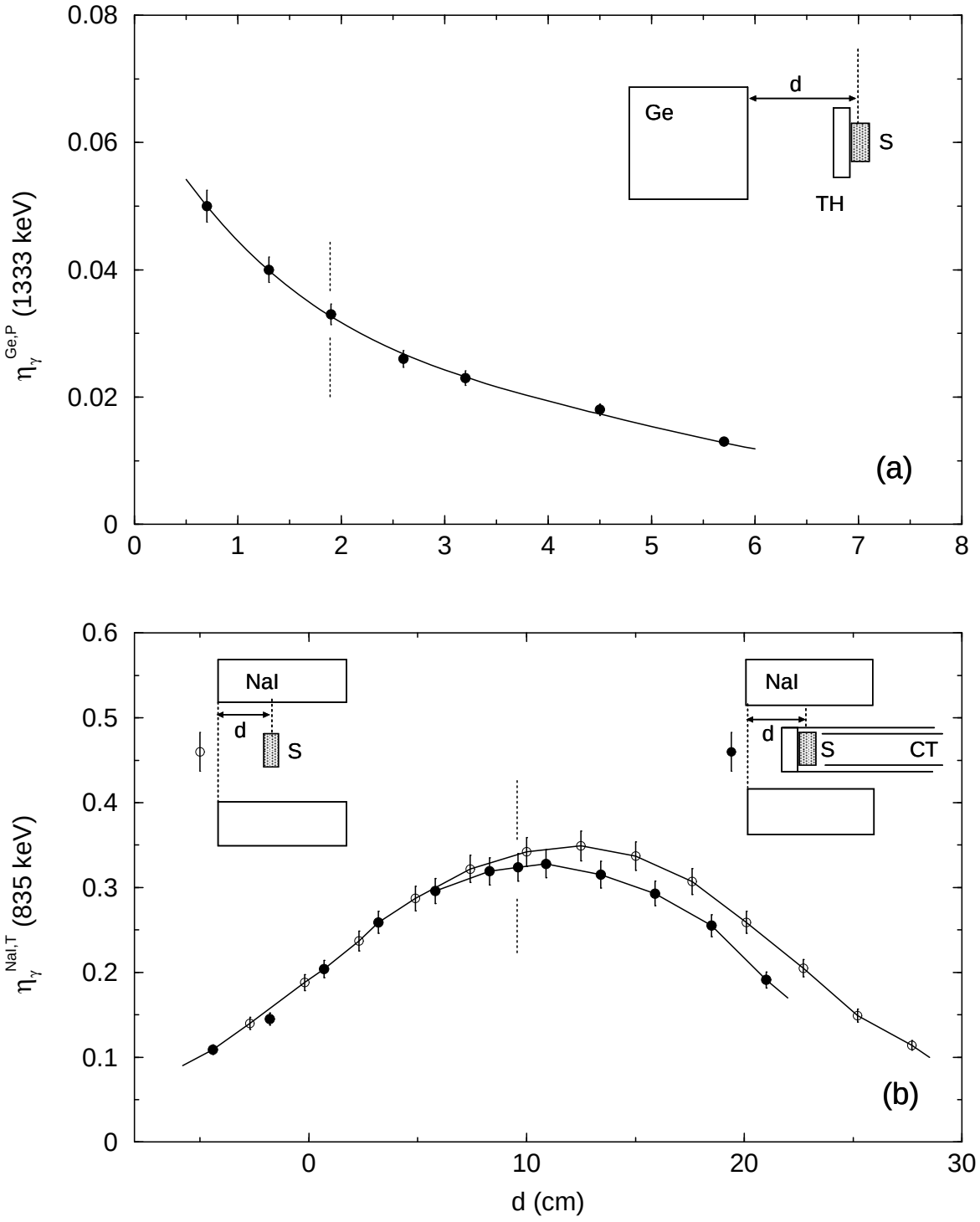

Figure 4.8: Dependence of detection efficiency on the distance between counter front face and source; (a) absolute full-energy peak efficiency of Ge detector at $E_\gamma = 1.33$ MeV (measured with ^{60}Co); (b) absolute total efficiency of NaI(Tl) detector at $E_\gamma = 0.83$ MeV (measured with ^{54}Mn). The dashed vertical lines indicate the geometry of the beam experiment (Sec. 4.2.2). Target holder, source and copper tube are labeled with TH, S and CT, respectively. The open and full circles in part (b) indicate efficiencies measured without and with the target holder, respectively (see Sec. 4.2.3). The solid lines are to guide the eye.

at maximum at d = 11.4 cm close to the center of the annulus. The data shown by solid circles were obtained by mounting the source in the target chamber including the copper tube. In addition, the germanium detector was kept at a distance of 1.9 cm with respect to the source in order to reproduce the conditions of the (p,γ) measurements (Sec. 3.2). Although the total NaI(Tl) efficiency decreases as compared to the case of the bare source because of γ–ray absorption effects, the changes are small (less than 5%). However, the NaI(Tl) energy resolution degrades rapidly beyond d = 13 cm owing to scattering and absorption of γ–rays in material located between source and detector.

4.3 Gamma-ray background studies

4.3.1 General considerations

According to Eq. 4.5, the sensitivity of the detection apparatus depends on the square-root of the average number of background counts in the region of interest. Therefore, it is important to understand the nature of the γ–ray background in germanium detector spectra (Figs. 4.2– 4.4) and to investigate possibilities for reducing the background further.

Possible sources of γ–ray background are discussed in Heusser [Heu95]. Terrestrial γ–radiation originates almost exclusively from the U and Th decay series and from ^{40}K decay. The majority of γ–rays from these sources, including radon in the air, have energies of less than E_γ = 3.0 MeV. Spontaneous fission of ^{238}U produces prompt γ–rays with energies up to 7 MeV. Cosmic radiation represents another important source of background. The most relevant cosmic-ray components for low-level γ–ray background measurements are muons and neutrons [Heu95, Voj94]. The muon-induced background arises from direct ionization events in the detector crystal, radioisotope production via interactions with nuclei, muon bremsstrahlung, production of δ–electrons, muon decay and electron-positron pair production. The latter three processes also give rise to bremsstrahlung. For typical germanium detectors, computer simulations

[Voj95] indicate that δ–electron production and direct ionization events are the dominant muon-induced background sources at γ–ray energies below and above $E_\gamma \approx 5$ MeV, respectively. Neutrons are also produced by primary cosmic radiation (these neutrons are also called secondary neutrons), spontaneous fission, and (α,n) reactions. Tertiary neutrons are produced by slow muons via the capture reaction p(μ^-,ν_μ)n, and by fast muons via (γ,n) reactions and photo-fission. Fast neutrons, in turn, react with nuclei via (n,n$'\gamma$) reactions, while thermal neutrons interact via (n,γ) reactions. Most γ–rays from neutron inelastic scattering and radiative neutron-capture have energies less than about 2 MeV [Heu93]. However, the neutron-capture reaction on iron, for example, produces γ–rays with energies of about 10 MeV.

Table 4.1 lists recently published background count rates for the energy region below $E_\gamma = 3.0$ MeV, measured using low-background germanium detector systems. Information regarding shielding, location and detector volume is also given. Note that the construction materials for all detection systems listed in the table have been carefully selected in order to reduce radioimpurities. Passive shields consisted of several layers of different low-activity materials (Pb, Cu, Fe, etc.). In some cases, plastic scintillators or multiwire proportional chambers have been used for active background discrimination. The results listed were obtained from *singles* germanium detector spectra. In laboratories located at sea level, singles background rates of ≥ 10 counts per minute (cpm) have been measured. Improved results were obtained either at moderate shielding depths by using anticoincidence counters or by performing the measurements deep underground, yielding singles background rates as low as 0.76 cpm. Unfortunately no published germanium detector background count rates for energies above $E_\gamma = 3.0$ MeV has been found.

It should be emphasized again that background radiation of energy in excess of 3.0 MeV is of primary importance for the present work. Radiation of smaller energy does not contribute to the *coincidence* germanium detector background in the region of the secondary or primary γ–ray transitions (Sects. 4.2.1 and 4.2.2). Thus, it is assumed that contributions of γ–rays from the U and Th decay series, ^{40}K decay, radon in the air and (n,n$'\gamma$) reactions to the background seen in the coincidence germanium spectra are

Reference	Shielding[a]	Location[b] (m w.e.)	V_{Ge}[c] (cm^3)	E_γ (keV)	$N_{\gamma,BG}^{Ge,sing}$ [d] (cpm)
Heusser 1991 [Heu91]	passive+active	15	170	511	0.011
				65–2680	1.65
	passive	1000	170	511	0.002
				65–2680	0.76
Heusser 1993 [Heu93]	passive+active	15	170	511	0.011
				50–500	0.7
Vojtyla 1994 [Voj94]	passive+active	0	180	40–1500	15
Bourlat 1994 [Bou94]	passive	4400	207	20–2000	1.0
Wordel 1996 [Wor96]	passive	0	100	95–2900	26
Laurec 1996 [Lau96]	passive+active	0	196	30–2700	10

Table 4.1: Comparison of background count rates from previous work.

[a] The construction materials for all detector systems listed have been carefully selected in order to reduce radioimpurities; the passive shields consisted of several layers of different low-activity materials (Pb, Cu, Fe etc.); for active shielding, either plastic scintillators or multiwire proportional chambers were used.

[b] Shielding depth in units of meter water equivalent.

[c] Active volume of germanium detector crystal.

[d] Singles germanium detector background count rate in units of counts per minute.

negligible. It is expected that muon-induced bremsstrahlung, direct ionization events of muons, γ–rays from spontaneous fission, and γ–rays induced by radiative neutron capture to be the most important sources of coincidence γ–ray background. Several different processes are likely to occur. For example, a single bremsstrahlung photon of energy $E_\gamma > 3$ MeV might Compton-scatter from the Ge to the NaI(Tl) detector or vice versa, and thereby depositing energy in both counters. Alternatively, one muon might create two or more bremsstrahlung photons close to the experimental apparatus and thus contribute to the coincident γ–ray background. Or, a muon might directly

ionize both germanium and NaI(Tl) detectors within the coincidence resolving time. Delayed background processes involving neutrons are also possible. For example, one parent muon might directly ionize only one of the detectors, but in addition it might create a neutron. The neutron slows down and produces a γ–ray after being captured. If the γ–ray is detected in the other counter, the process gives rise to a coincidence background event. Clearly, the situation is complex and the relative contribution of different processes to the coincidence γ–ray background will depend sensitively on the geometric and construction details of the setup.

Note that at a bombarding energy of $E_R \approx 0.23$ MeV there is no observation of any γ–ray lines from contaminant proton-induced reactions. The continuous background in the coincidence germanium spectra measured with beam at $E_R \approx 0.23$ MeV and without beam also show insignificant differences.

4.3.2 Experimental results

In the following, possibilities for further reducing the background observed in the coincidence germanium spectra (Figs. 4.2(c) and 4.4(b)) are investigated. A series of measurements was performed without beam at LENA. The germanium and NaI(Tl) detectors were arranged in the same relative geometry as described before (Sec. 3.2 and Fig. 3.4). Measured germanium background spectra are presented in Fig. 4.9. The left-hand side of the figure shows the energy region E_γ^{Ge} = 600–3000 keV in coincidence with a NaI(Tl) window of E_γ^{NaI} = 3000–9000 keV, while the right-hand side displays the region E_γ^{Ge} = 4000–9000 keV in coincidence with a NaI(Tl) window of E_γ^{NaI} = 250–3500 keV. Each spectrum was recorded for about 24 hours. The corresponding background count rates are listed in Table 4.3.2.

First, the setup of the TUNL beam experiment was reproduced. The germanium spectrum shown in Fig. 4.9(a) was recorded without any shielding. The measured coincidence background count rates are 3.0 and 2.3 cpm for the energy regions E_γ^{Ge} = 600–3000 keV and E_γ^{Ge} = 4000–9000 keV, respectively, in agreement with the results obtained earlier (Figs. 4.2(c) and 4.4(b)). A comparison of Tables 4.1 and 4.3.2

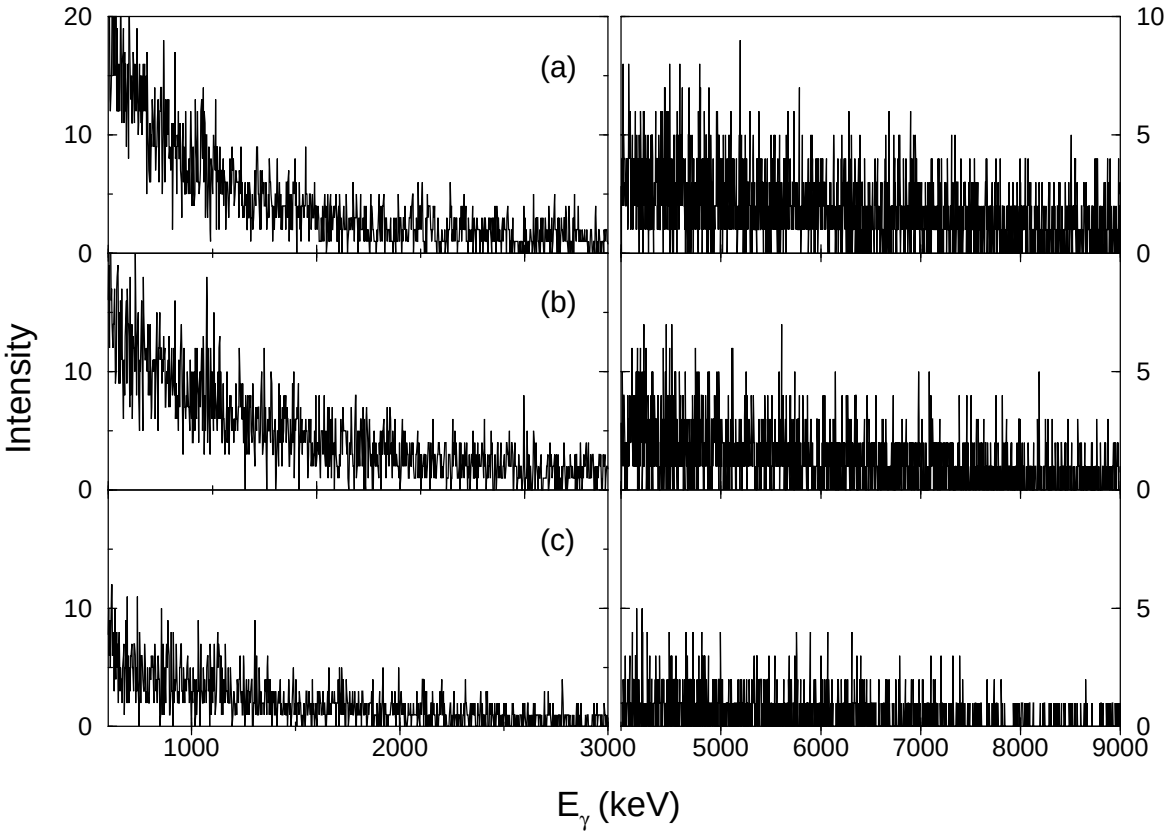

Figure 4.9: Coincidence Ge background spectra for energies E_γ^{Ge} = 600–3000 keV (left) and E_γ^{Ge} = 4000–9000 keV (right). The corresponding coincidence energy windows in the NaI(Tl) detector are E_γ^{NaI} = 3000–9000 keV and E_γ^{NaI} = 250–3500 keV, respectively; (a) no shielding; (b) passive shielding; (c) passive and active shielding. The spectra were recorded without beam for 24 h. Corresponding background count rates are listed in Table 4.3.2. Note that Fig. 4.2(b) shows a singles Ge detector spectrum obtained with a lead shield, whereas the left-hand side of Fig 4.9(b) displays a coincidence spectrum obtained with lead shielding.

shows that for energies $E_\gamma^{Ge} < 3$ MeV the coincidence background count rate is smaller than the previous singles background count rates measured in laboratories at sea level.

Second, the germanium and NaI(Tl) detectors were surrounded with lead of 5 cm thickness. As a consequence, the coincidence background count rate for E_γ^{Ge} = 600–3000 keV increased to 3.3 cpm, while the count rate for E_γ^{Ge} = 4000–9000 keV decreased to 1.6 cpm, as shown in Fig. 4.9 (b) and Table 4.3.2. The result suggests that higher-energy γ–rays were converted to lower energies by the material of the passive shield via Compton scattering and pair production. For this mode of operation, the measured contribution of random coincidences to the background count rates quoted above is less than 0.6%. Third, an anticoincidence counter was added to the setup in order to reduce

Mode[b]	$N_{\gamma,BG}^{Ge,coin}$ (cpm)[c]		
	511 keV	600–3000 keV	4000–9000 keV
no shield	0.53	3.0	2.3
passive shield	0.27	3.3	1.6
passive+active shield	0.11	1.2	0.71

Table 4.2: Background count rates measured in present work[a].

[a] Studies performed without beam after the proton capture experiment at LENA by using the same relative geometry of Ge and NaI(Tl) detectors; the Ge detector volume was 582 cm^3.

[b] The passive shield consisted of lead with a thickness of 5 cm; for active shielding a single plastic scintillator was used as anticoincidence counter.

[c] Coincidence germanium detector background count rates in units of counts per minute; events of the annihilation peak and the energy region E_γ^{Ge} = 600–3000 keV are in coincidence with a NaI(Tl) energy window of E_γ^{NaI} = 3000–9000 keV, while events of the region E_γ^{Ge} = 4000–9000 keV are in coincidence with a NaI(Tl) energy window of E_γ^{NaI} = 250–3500 keV.

muon-induced background events, including γ–rays from tertiary neutron interactions. A plastic scintillator with length, width and thickness of 175 cm, 50 cm and 5 cm, respectively, was placed above the lead shield and centered above the germanium crystal. A veto signal duration of 10 μs was chosen in order to account for delayed muonic background events [Ste68, Heu91]. With an anticoincidence detector count rate of $\approx$ 5000/s, the dead-time correction measured with a ^{60}Co source amounted to about 5%. The measured coincidence germanium background spectrum (with veto) is shown in Fig. 4.9 (c). The coincidence background count rates are reduced to 1.2 and 0.71 cpm for energies of E_γ^{Ge} = 600–3000 keV and E_γ^{Ge} = 4000–9000 keV, respectively (Table 4.3.2). The observed background reduction by a factor of 2-3 is smaller than what is expected from the polar angle distribution of muons at sea level [Voj95] and the solid angle covered by the plastic scintillator. Similar background suppressions by using only one anticoincidence counter positioned above the germanium detector have been reported in Heusser [Heu91] and Vojtyla *et al.* [Voj94]. Test runs with a longer

veto signal duration of 20 μs gave similar results.

4.4 Conclusions

The smallest coincidence germanium background count rates observed in the present work (Table 4.3.2) might be reduced further by several techniques. The most obvious improvement involves a five- or six-sided anticoincidence detector arrangement for better suppression of muon-induced background events. With such devices, singles germanium background reduction factors of 5–13 at $E_\gamma < 3.0$ MeV [Heu91, Lau96] and 6–70 at $E_\gamma = 4.5$–12.0 MeV [Mül90, For84] have been reported previously.

It might be possible to take advantage of the NaI(Tl) detector segmentation in order to discriminate some muon-induced events based on their presumably high multiplicity. However, an average multiplicity of only three has been reported by Kamikubota *et al.* [Kam86] for charged cosmic ray events. Since many γ–ray cascades produced by (p,γ) or (α,γ) reactions will have similar multiplicities, the success of this method is rather uncertain.

Recently, discrimination techniques based on germanium detector pulse shapes were investigated and it has been demonstrated that a fraction of Compton-scattered γ–ray events escaping from the Ge detector could be rejected. Such methods are based, for example, on differences in pulse rise times [Zop93] or on unfolding of complete charge pulse shapes [Sch99]. At present, these methods achieve a suppression of Compton escape events at the expense of a reduced full-energy peak efficiency, a result which is undesirable in view of Eq. 4.5.

Finally, the coincidence germanium background induced by cosmic rays may be substantially suppressed by locating an apparatus similar to that used in the present work deep underground. It would be interesting to investigate how the background levels achieved underground compare to measurements at sea level with a complete anticoincidence shield.

Chapter 5

The ^{23}Na(p,α)^{20}Ne reaction

5.1 Motivation

As mentioned in 1.3, many important nuclear reactions in stars proceed through resonances and the thermonuclear reaction rates are directly proportional to the resonance strengths [Rol88].

Most resonance strengths are derived from the step height of thick-target yield curves as described in [Gov59]. This method requires knowledge of the target stoichiometry, absolute stopping powers, absolute proton charge deposited on the target and absolute detection efficiencies. All these factors are difficult to determine and are sources of potential systematic errors. Consequently, discrepancies by factors of two or more between different absolute resonant strength measurements are common in the literature. Relative measurements of resonance strengths are less difficult and literature values derived by different authors are usually in good agreement. Relative resonance strengths are frequently converted to absolute strengths by comparing the thick-target yield for the resonance of interest to the yield for a resonance of recommended standard strength.

Reliable resonance strength standards for (p,α) reactions at low energies have not been reported in the literature because of the above described difficulties. Powell [Pow99] described a method of measuring absolute resonance strengths for (p,γ) reactions which does not depend on the properties of the target (stoichiometry, stop-

ping power and uniformity) and the incident ion beam (current integration and beam straggling). This method has been used in the present work and extended to the case of a (p,α) reaction. This method involves measuring the number of resonant α–particles, integrated over the yield curve, simultaneously with the number of Rutherford-scattered protons.

The method described in Powell *et al.* was used to measure the E_R = 338 keV[1] resonance in the ^{23}Na(p,α)^{20}Ne reaction. As mentioned in Sec. 1.3, there were no standard resonance strengths available for this reaction prior to the present work. This measurement was performed at the TUNL Low Energy Beam Facility. The equipment used, including the experimental setup, targets, and detectors has been described in Ch. 3. The results described in this chapter have been published (see Rowland *et al.* [Row02b]).

Sec. 5.2 of this chapter describes the formalism of determining absolute resonance strengths for a (p,α) reaction. The procedures for measuring resonance strengths and detection efficiencies are presented in Sec. 5.3. Experimental results and implications of this experiment are given in 5.4. Throughout this chapter, E_p and E_R denote the proton bombarding energy and the resonance energy, respectively.

5.2 Formalism

For a (p,α) reaction, the resonance strength is defined by

$$\omega\gamma \;=\; \frac{2J+1}{(2J_t+1)(2J_p+1)}\frac{\Gamma_p\Gamma_\alpha}{\Gamma}, \tag{5.1}$$

where J, J_p and J_t are the spin of the resonance state, projectile and target nucleus, respectively. The partial widths Γ_p and Γ_α describe the probability of formation and decay of the resonance through the proton and α–particle channel, respectively. The resonance strength $\omega\gamma$ is related to the area, A, under a resonant yield curve [Gov59] by

[1]Note that Endt [End90] quotes a value of E_R = 338.6 ± 0.6 keV, whereas one obtains E_R = 336.3 ± 0.8 keV from the quoted excitation energy[End90] and the (p,γ) Q-value [Aud95].

$$\omega\gamma \;=\; \frac{2}{\lambda^2}\,\frac{1}{n_t}\,A, \tag{5.2}$$

where λ is the de Broglie wavelength of the incident proton evaluated at the resonance energy, and n_t is the number of active target nuclei per unit area. It is shown in Gove that Eq. 5.2 is independent of straggling and beam homogeneity. In Powell *et al.* [Pow98], it was stated that Eq. 5.2 is applicable if the target thickness is much larger than the resonance width. However, closer inspection of the formalism described in [Gov59] reveals that $\omega\gamma$ in Eq. 5.2 is independent of the resonance width as long as (i) the resonant cross section is described by the Breit-Wigner formula (Eq. 2.13) and (ii) the de Broglie wavelength and the partial widths are nearly constant over the width of the resonance. This consideration is important for the present work since the $E_R = 338$ keV resonance in ^{23}Na(p,α)^{20}Ne has a total width of ≈ 0.7 keV [End90].

The differential yield Y_{Ruth} of Rutherford-scattered protons is given by

$$Y_{Ruth} \;=\; \int_{E-\xi}^{E} \frac{\sigma_{Ruth}(E')}{\epsilon(E')}dE' \;\approx\; \sigma_{Ruth} n_t, \tag{5.3}$$

where E is the bombarding proton energy, ϵ is the stopping power, ξ is the target thickness in units of energy, and σ_{Ruth} is the differential Rutherford cross section. For sufficiently thin targets, the cross section and the stopping power are approximately constant over the target thickness. The approximation in Eq. 5.3 may be substituted into Eq. 5.2 allowing the resonance strength to be written as

$$\omega\gamma \;=\; \frac{2}{\lambda^2} A \frac{\sigma_{Ruth}}{Y_{Ruth}}. \tag{5.4}$$

The resonance strength in Eq. 5.4 is independent of target and beam properties.

The area under a resonant γ–ray yield curve is given experimentally by

$$A \;=\; \frac{1}{B_\gamma \eta_\gamma W_\gamma(\theta)} \int \frac{N_\gamma(E)}{N_p(E)}dE, \tag{5.5}$$

where N_γ, B_γ, η_γ and W_γ are the number of observed γ–rays, the branching ratio, the detection efficiency, and the angular distribution. N_p is the number of incident protons. It follows that the area under a resonant α–particle yield may be written as

$$A \;=\; \frac{1}{\eta_\alpha W_\alpha(\theta)} \int \frac{N_\alpha(E)}{N_p(E)} dE, \tag{5.6}$$

with N_α, η_α and W_α being the number of α–particles, the α–particle detection efficiency, and the angular distribution of the resonant α–particles averaged over the solid angle of the α–particle detector. The differential yield of Rutherford scattered protons, with incident energy E, is given by

$$Y_{Ruth}(E) \;=\; \frac{N_{p'}(E)}{N_p(E)\Omega_p}, \tag{5.7}$$

where $N_{p'}$ is the number of backscattered protons, and Ω_p is the center-of-mass solid angle of the proton detector. As long as the proton scattering is well described by the Rutherford law, the ratio of σ_{Ruth}/Y_{Ruth} in Eq. 5.4 is independent of bombarding energy and may be measured at any value of E. If the resonant γ–rays or α–particles are detected simultaneously with the elastically scattered protons, the resonance strength may be written as

$$\omega\gamma_{p\gamma} \;=\; \frac{2}{\lambda^2} \frac{1}{B_\gamma W_\gamma(\theta)} \frac{\Omega_p}{\eta_\gamma} \int \frac{N_\gamma(E)}{N_{p'}(E)} \sigma_{Ruth}(E) dE \tag{5.8}$$

for a (p,γ) reaction, and

$$\omega\gamma_{p\alpha} \;=\; \frac{2}{\lambda^2} \frac{4\pi}{W_\alpha(\theta)} \frac{\Omega_p}{\Omega_\alpha} \int \frac{N_\alpha(E)}{N_{p'}(E)} \sigma_{Ruth}(E) dE \tag{5.9}$$

for a (p,α) reaction. Note that in Eq. 5.9 the efficiency of the α–particle detector is replaced by $4\pi/\Omega_\alpha$, where Ω_α is the solid angle of the α–particle detector. The resonance strengths given by Eqs. 5.8 and 5.9 are independent of the properties of the target (stoichiometry, stopping power and uniformity) and of the beam (current integration and straggling). The (p,α) resonance strength $\omega\gamma_{p\alpha}$ does depend on the observed numbers of resonant α–particles and elastically scattered protons, and on the angular distribution of the resonant α–particles. Further, $\omega\gamma_{p\alpha}$ depends on the ratio Ω_p/Ω_α and, consequently, is independent of the knowledge of *absolute* α–particle and proton detection efficiencies. This ratio was measured directly in the present work with the ^{15}N(p,α)^{12}C reaction at E_R = 340 keV. It should be noted that all quantities in Eq. 5.9 are given in the center-of-mass system.

5.3 Procedure

5.3.1 Yields of α–particles and protons

A typical resonant α–particle spectrum measured at $E_p = 341$ keV, with the α–particle detector positioned at $\theta_\alpha = 140°$, is shown in the top part of Fig. 5.1. The α–particle yield curve of the $E_R = 338$ keV resonance in ^{23}Na(p,α)^{20}Ne obtained with a 5 keV thick NaCl transmission target is presented in Fig. 5.2. A χ^2 minimization algorithm was used in order to determine the area under the resonant yield curve. This routine begins with the assumption that the reaction yield of a target with thickness ξ at a beam energy E_o may be written as

$$Y(E_o) = \int_{E_o-\xi}^{E_o} \frac{\sigma(E)}{\epsilon(E)} dE. \tag{5.10}$$

The shape, and hence the area, of a yield curve may be affected by a two factors. First, charged-particle beams are never completely monoenergetic. The beam generally has some distribution given by $g(E, E_o)$, where E_o is the mean incident energy. This beam spread may be approximated by a Gaussian function as described in Rolfs and Rodney [Rol88]. The second factor affecting the shape of the yield curve is beam straggle. This occurs as the beam of charged particles penetrates matter, slows down and spreads in energy because of statistical fluctuations in the number of collisions. The beam straggle, $W(E, E', E'')$, may also be approximated by a Gaussian function. Folding in the effects of beam spread and beam straggle, the reaction yield may be written as a triple integral,

$$Y(E_o) = \int_{E_o-\xi}^{E_o} \int_0^\infty \int_0^\infty \frac{\sigma(E'')}{\epsilon(E'')} g(E', E_o) W(E, E', E'') dE'' dE' dE. \tag{5.11}$$

As mentioned above, the yield curve data in the present work was fit via a χ^2 minimization algorithm. The area was found by integrating over the fit. The uncertainty in the area is given by [Pow99]

$$\sigma_A^2 = \xi^2 \sigma_H^2 + H^2 \sigma_\xi^2 + 2\xi H \sigma_\xi \sigma_H C, \tag{5.12}$$

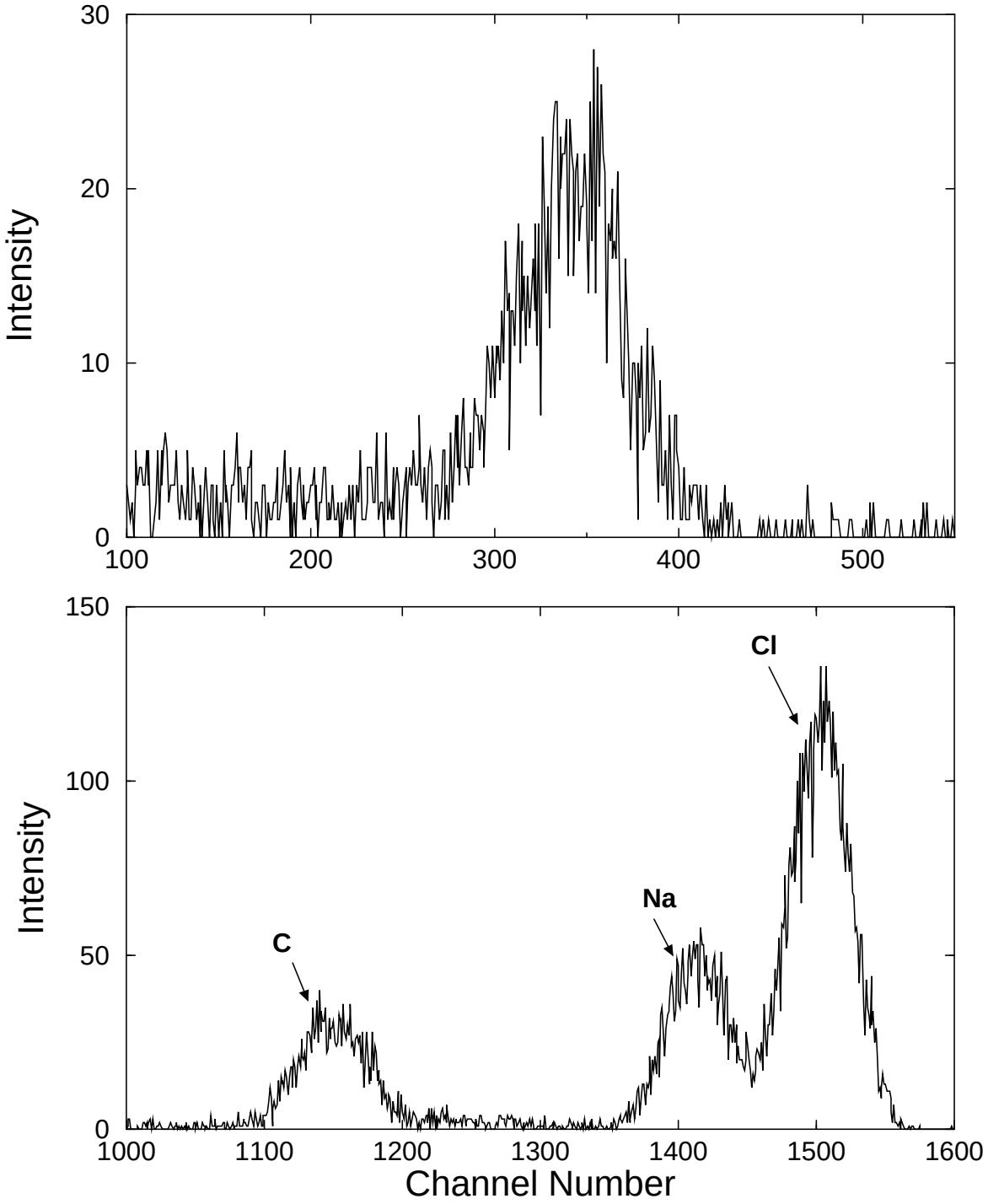

Figure 5.1: Top: Resonant α–particle spectrum measured at E_p = 341 keV with the α–particle detector located at $\theta_\alpha = 140°$. The peak centroid corresponds to an α–particle energy of about 720 keV. Potential background from elastically-scattered protons caused by pinholes in the Havar foil would occur below 300 keV (channel 130). Bottom: Spectrum of elastically scattered protons measured with a NaCl transmission target, obtained at E_p = 400 keV and $\theta_p = 155°$.

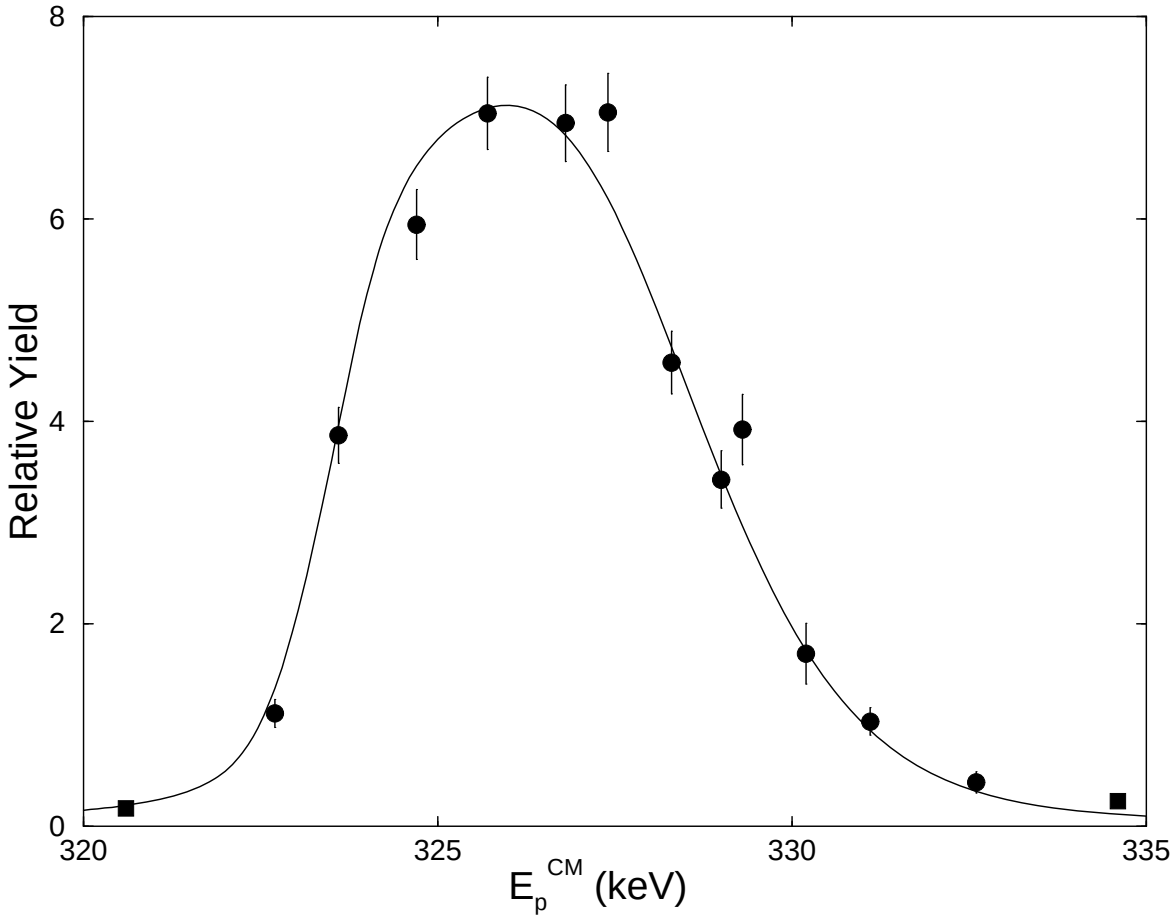

Figure 5.2: Relative yield of α–particles in the energy region of the 338 keV resonance in ^{23}Na(p,α)^{20}Ne. The solid line is a least-squares fit to the data. The squares represent upper limits.

where ξ and σ_ξ is the target thickness and its uncertainty, H and σ_H is the yield curve height and its uncertainty. C is the correlation between the height and target thickness. Using the above formalism, the integral in Eq. 5.9 was found to have a value of (42.70 ± 0.87) fm^2 keV/sr.

A proton spectrum measured at $E_p = 400$ keV with the proton detector positioned at $\theta_p = 155°$ is displayed in the bottom part of Fig. 5.1. Contributions from Na, Cl and from the carbon backing are clearly resolved. It should be pointed out that the peak positions of protons elastically scattered by Na or Cl contain information regarding the bombarding energy and have been used in order to check the energy calibration of the accelerator.

Our method of measuring absolute resonance strengths depends on the assumption

that the proton elastic scattering at low energies is well described by the Rutherford law. This assumption was verified in the present work by measuring the yield of scattered protons (i) as a function of bombarding energy at fixed detector angle (top left part of Fig. 5.3), and (ii) as a function of detector angle at constant bombarding energy (top right part of Fig. 5.3). The bottom part of Fig. 5.3 shows the yield curve for proton elastic scattering over the region of the E_R = 338 keV resonance in ^{23}Na(p,α)^{20}Ne. The data include on- and off-resonance runs. The solid lines represent the Rutherford yield normalized to the data points. No deviations from the Rutherford law were observed in any of the elastic scattering yield curves obtained in the present work.

5.3.2 Detection efficiencies

The resonance strength $\omega\gamma_{p\alpha}$ given in Eq. 5.9, depends on the ratio of proton and α–particle detection efficiencies. In the present work, the ratio was measured near the broad E_R = 335 keV ($J^\pi = 1^-$) resonance in ^{15}N(p,α)^{12}C. It is shown in Redder *et al.* [Red82] that the angular distribution of the ^{15}N(p,α)^{12}C reaction is isotropic at E_p = 340 keV. Therefore the solid angle ratio Ω_p/Ω_α is given, apart from center-of-mass corrections, by the ratio of the observed α–particle intensities in each detector. This measurement was performed with a thin ^{15}N enriched melamine ($C_3H_6N_6$) target with the same setup as used for the resonance strength measurement. After correcting for the effects of finite target thickness and detector solid angle attenuation, the ratio of proton and α–particle detector solid angles is found to have a value[2] of $\Omega_p^{lab}/\Omega_\alpha^{lab} = (2.330 \pm 0.057)\cdot 10^{-4}$. This result has a much smaller error compared to the value $\Omega_p^{lab,abs}/\Omega_\alpha^{lab,abs} = (2.1 \pm 0.3)\cdot 10^{-4}$, which is calculated from the geometry of the charged-particle detectors.

[2]The quoted number has to be converted to the ^{23}Na+p center-of-mass system for use in Eq. 5.3. The result is $\Omega_p/\Omega_\alpha = (2.283 \pm 0.057)\cdot 10^{-4}$. Note that a value of unity has been assumed for the intrinsic efficiencies of the charged-particle counters for the detection of low-energy protons and α–particles. This assumption has been verified in the present work by performing Monte-Carlo simulations using the SRIM software[Bie95].

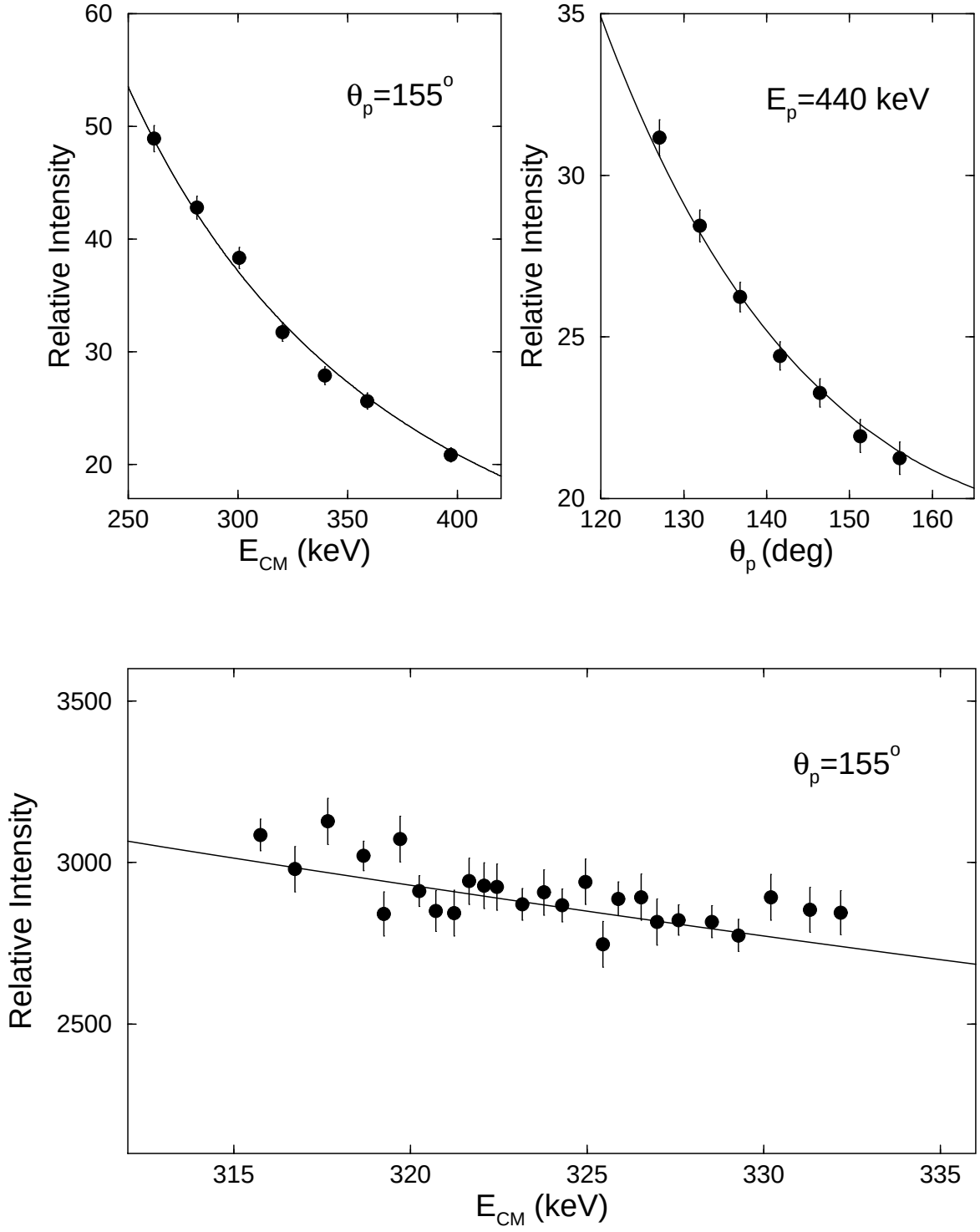

Figure 5.3: Yields of elastically scattered protons from ^{23}Na. The top left part of the figure shows the yield as a function of bombarding energy, with the proton detector located at $\theta_p = 155°$. The top right part shows the angular distribution obtained at $E_p = 440$ keV. The bottom part of the figure shows yields of elastically scattered protons over the region of the $E_R = 338$ keV resonance in ^{23}Na(p,α)^{20}Ne. The data include on- and off-resonance runs. In all diagrams the solid line represents the Rutherford yield normalized to the data.

5.3.3 Angular distribution

As can be seen from Eq. 5.9, the resonance strength depends on the angular distribution of the resonant α–particles. The angular distribution [Gov59] is

$$W_\alpha(\theta_{CM}) \;=\; 1 + \sum_k a_k Q_k P_k(cos\theta_{CM}), \tag{5.13}$$

where a_k, Q_k, and $P_k(\cos\theta_{CM})$ are the angular distribution coefficients, solid angle attenuation coefficients and Legendre polynomials, respectively. For the E_R = 338 keV ($J^\pi = 1^-$) resonance in ^{23}Na(p,α)^{20}Ne, the angular distribution coefficients, a_k, have been measured previously by Fisher and Whaling [Fis63] and Kuperus et al. [Kup63]. The results of these independent measurements are in excellent agreement and a weighted average has been adopted in the present work. The attenuation coefficients, Q_k, have been estimated according to the procedure given in Gove [Gov59]. The resulting value for the angular distribution, averaged over the solid angle of the α–particle detector, is $W_\alpha(\theta_{CM} = 141.2^\circ) = 1.293 \pm 0.034$.

5.4 Results and implications

A value of $\omega\gamma_{p\alpha} = (7.16 \pm 0.29)\cdot 10^{-2}$ eV was obtained for the E_R = 338 keV resonance in ^{23}Na(p,α)^{20}Ne. The experimental error of 4.1% is given by uncertainties in the area under the resonance curve (2.0%), the ratio of the proton and α–particle detection efficiencies (2.5%), and the α–particle angular distribution (2.6%).

Previous values for the resonance strength were determined using the step height of the thick-target yield curve, Y_α, according to

$$\omega\gamma \;=\; \frac{2\epsilon_{eff}}{\lambda^2}\;\frac{Y_\alpha}{\Omega_\alpha W_\alpha(\theta)}. \tag{5.14}$$

All measurements (present and previous) have used NaCl targets. In this case, the effective stopping power is given by

$$\epsilon_{eff} \;=\; \epsilon_{Na} + \frac{N_{Cl}}{N_{Na}}\epsilon_{Cl}, \tag{5.15}$$

$\omega\gamma\times10^{-3}$ (eV)				
Present	Ref.[Gör89]	Ref.[Fis63][a,b]	Ref.[Fla54][a,c]	Ref.[Kup63][a]
71.6 ± 2.9	97 ± 19	88 ± 16	72 ± 18	130 ± 33

Table 5.1: Absolute resonance strengths for the E_R = 338 keV resonance in ^{23}Na(p,α)^{20}Ne.

[a] Obtained by using stopping powers from Biersack *et al.* [Bie95] (with an estimated error of 15%), assuming a target stoichiometry of Na:Cl = 1:1.

[b] Calculated from the reported differential α–particle yield measured at $\theta_\alpha = 90°$.

[c] Calculated from the reported total α–particle yield and corrected for angular distribution effects.

where ϵ_{Na} and ϵ_{Cl} are the stopping powers of protons in Na and Cl, respectively, at the resonance energy; N_{Cl} and N_{Na} are the number of Cl and Na target atoms per unit area. All quantities in Eqs. 5.14 - 5.15 are given in the center-of-mass system.

In Kuperus *et al.* and Görres *et al.*, resonance strengths were obtained by assuming a target stoichiometry of Na:Cl = 1:1. In Fisher and Whaling and in Flack *et al.* [Fla54], only resonant α–particle yields are presented. Those yields have been converted into resonance strengths by using the stopping power values of Biersack and Ziegler [Bie95] and a stoichiometry of Na:Cl = 1:1. All $\omega\gamma_{p\alpha}$ values are listed in Table 5.1 and are shown in the top part of Fig. 5.4. It is apparent that (i) the error of the present $\omega\gamma_{p\alpha}$ value is much smaller compared to previous results and (ii) most $\omega\gamma_{p\alpha}$ values reported in the literature are systematically higher compared to the present result.

It can be seen that that a reliable resonance strength can only be obtained from Eqs. 5.14 - 5.15 if the target stoichiometry is accurately known. It is interesting to note that the stoichiometry of NaCl targets changes under proton bombardment. The effect is demonstrated in Fig. 4 of Paine *et al.* [Pai78]. The NaCl targets lost significant amounts of chlorine during bombardment. After an accumulated charge of $\approx 8{\cdot}10^{-5}$ C, the stoichiometry amounted to Na:Cl = 5:3 and remained approximately constant for continued charge collection. An accumulated charge of $8{\cdot}10^{-5}$ C is obtained after only 1.6 s with a 50 μA proton beam (as used in Görres *et al.*) or after 260 s with a 300 nA

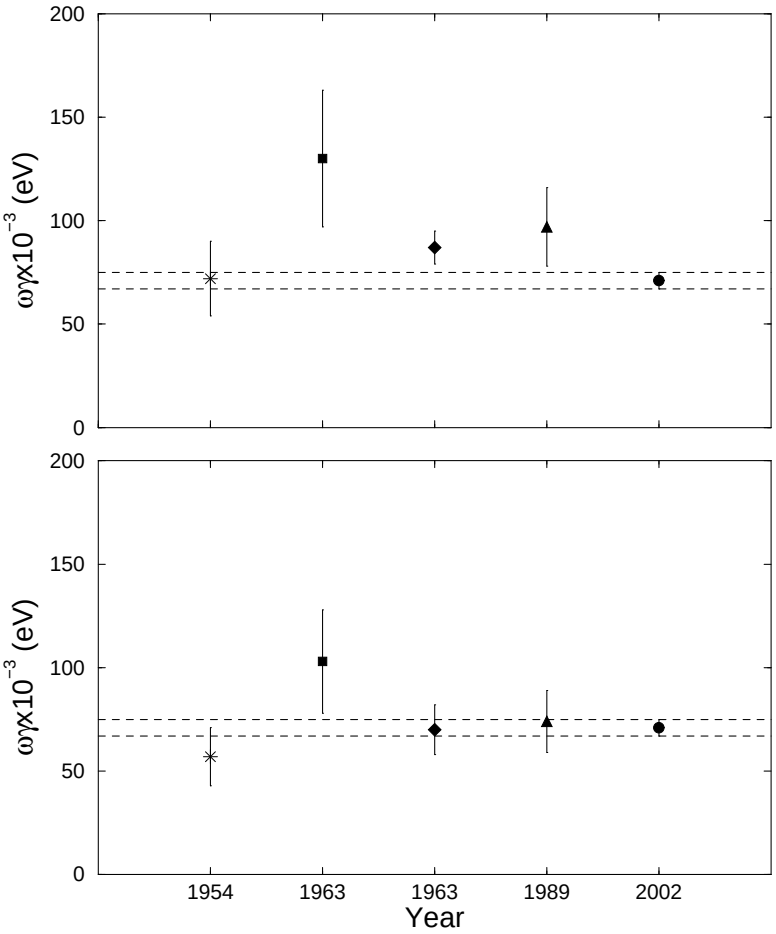

Figure 5.4: Top: Present value for the resonance strength compared with values reported in the literature, versus year of measurement. Symbols: star [Fla54], square [Kup63], diamond [Fis63], triangle [Gör89], circle (present work). Bottom: Present value for the resonance strength compared with literature results. The latter values have been corrected for a stoichiometry of Na:Cl = 5:3. The dotted lines indicate the error of the present value.

proton beam (as used in the present work). Therefore, the conclusion is that the target stoichiometry of all NaCl targets used in measurements of the ^{23}Na(p,α)^{20}Ne reaction differs significantly from the commonly assumed value of Na:Cl = 1:1. Shown again in the bottom part of Fig. 4.3 are all $\omega\gamma_{p\alpha}$ values, but now corrected for the variation in target stoichiometry (i.e., assuming a stoichiometry of Na:Cl = 5:3). Clearly, the agreement between the present result (which is *independent* of target stoichiometry) and previous values has improved significantly.

The new value for the E_R = 338 keV resonance strength is used as a standard strength for the determination of the ^{23}Na(p,γ)^{20}Ne reaction rate. The resulting re-

action rate and astrophysical implications are presented in Ch. 7.

Chapter 6

The ^{23}Na(p,γ)^{24}Mg reaction

6.1 Motivation

As shown in Fig. 1.4, the ratio of the ^{23}Na(p,α)^{20}Ne rate to the ^{23}Na(p,γ)^{24}Mg rate is uncertain by four orders of magnitude at temperatures of astrophysical interest. The largest source of uncertainty in the ^{23}Na(p,γ)^{24}Mg reaction rate comes from a resonance at E_R = 144 keV (E_x = 11828 keV). The current literature value for the E_R = 144 keV resonance strength is an upper limit (Görres et al. gives a value of $\omega\gamma \leq 5{\cdot}10^{-6}$ eV [Gör89].) In the present work, a new upper limit for this resonance has been determined. Using the same experimental setup and analysis techniques, the E_R = 251 keV and 309 keV resonance strengths were also measured. Although these resonances do not contribute to the uncertainty in the reaction rate as strongly as the E_R = 144 keV resonance, they are useful as a check of the techniques used.

The new value for the upper limit was obtained using the coincidence methods described in Ch. 4. This measurement was performed at the TUNL Laboratory for Experimental Nuclear Astrophysics (LENA) and the equipment used, including the experimental setup, targets, and detectors has been described in Ch. 3.

Determination of the E_R = 144 keV resonance strength is complicated because the decay of this resonance is not known. The formalism used in determining an upper limit for such a case is described in Sec. 6.2. The procedure used for measuring this resonance strength and the strengths of the E_R = 251 and 309 keV resonances is

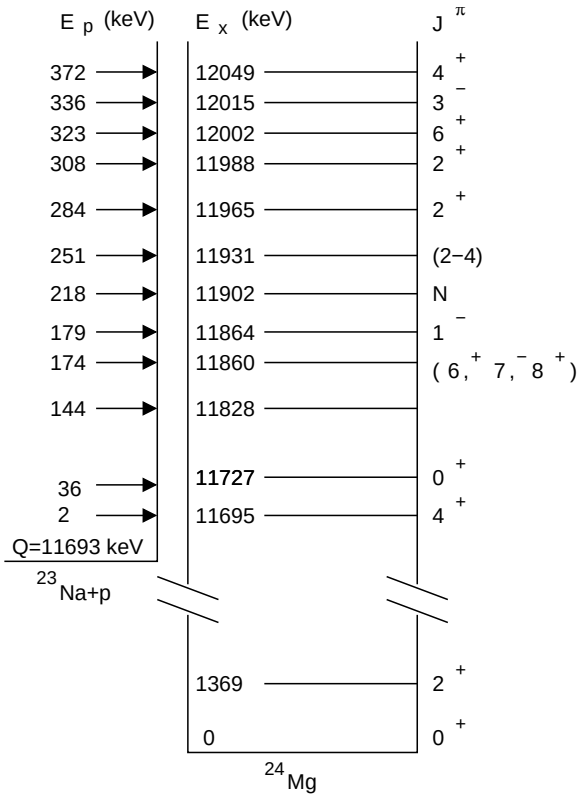

Figure 6.1: Level diagram of ^{24}Mg. Low-lying levels and proton threshold states are shown together with corresponding resonances. Energies and J^{π} values are adopted from Ref. [End90]

presented in Sec. 6.3.

6.2 Formalism

As described in Ch. 4, for many reactions of astrophysical interest the majority of primary γ–ray transitions proceed to the first few excited levels in the compound nucleus. For the ^{26}Mg(p,γ)^{27}Al reaction, these levels are located at energies $E_x < 3.0$ MeV, and this is also the case for the ^{23}Na(p,γ)^{24}Mg reaction. An energy level diagram with proton threshold states and corresponding resonances for ^{23}Na+p is shown in Fig. 6.1. A statistical analysis of the branching ratios of fifty-six ^{24}Mg levels shows that all γ–rays either decay through the first excited state at $E_\gamma = 1369$ keV or, in a few cases, proceed directly to the ground state.

In Sec. 4.2.1, the resonance strength is related to the thick-target yield by Eq. 4.1,

and the thick-target yield is given experimentally by Eq. 4.2. From these equations, it follows that an upper limit for the resonance strength may be obtained from the singles germanium spectrum with the following:

$$\omega\gamma \;\leq\; \frac{2}{\lambda_{CM}^2}\;\epsilon_{CM}\frac{1}{N_p}\;\left(\frac{N_{\gamma,R0}^{Ge,S}}{\eta_{\gamma R0}^{Ge,P}}\;+\;\frac{N_{\gamma 10}^{Ge,S}}{\eta_{\gamma 10}^{Ge,P}}\frac{1}{B_\gamma}\right), \tag{6.1}$$

where we assume that this resonance either decays with 100% to the ground state or through the first excited state at 1369 keV with a branching ratio of B_γ. N_γ is the number of observed γ-rays and $\eta_\gamma^{Ge,P}$ is the germanium detector full energy peak efficiency. The $R0$ and 10 subscripts indicate the transitions from resonance to ground state and from first excited state to ground state, respectively. The S superscript implies the number of observed γ-rays is taken from the singles spectrum.

The branching ratios are not known for the decay of the $E_R = 144$ keV ($E_x = 11828$ keV) resonance, but is possible to obtain a conservative estimate for the probability B_γ in Eq. 6.1. Fig. 6.2 shows the probability of decay through the first excited state for all ^{24}Mg levels below $E_x = 12$ MeV. From Fig. 6.2, it is clear that B_γ is at least 25%. Adopting this value for the branching ratio, we obtain from Eq. 6.1, an upper limit for this resonance strength of $\omega\gamma \leq 1.0{\cdot}10^{-6}$ eV. It should be noted that in determining $N_{\gamma,R0}^{Ge,S}$ the NaI annulus was operated as a veto shield with a veto gate of 5 μs. The ground state transition contributes most to the resonance strength upper limit.

The upper limit for the secondary transition (1369 keV to ground state) may be reduced substantially via the coincidence technique discussed in Ch. 4. Consider the decay scheme shown in Fig. 6.3. Of interest is the detection of the transition from the first excited state to the ground state (γ_{10}) in the germanium spectrum. If the NaI spectrum is used to detect in coincidence various primary transitions, the number of observed γ–rays for the first excited state to ground state transition in the coincidence Ge spectrum for cascade **b** is given by

$$N_{\gamma 10}^{C,Ge} \;=\; N\;B_{\gamma 31}B_{\gamma 10}\;\eta_{\gamma 10}^{Ge,P}\eta_{\gamma 31}^{NaI,T}, \tag{6.2}$$

where N is the total number of decays, B_{ji} is the branching ratio from level j to i,

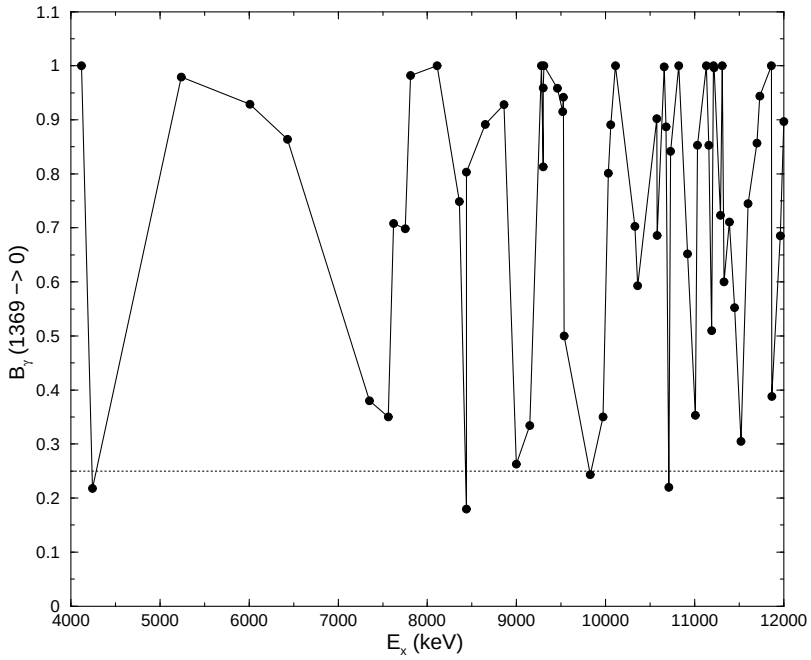

Figure 6.2: The branching ratio of the first excited state (E_x = 1369 keV) to the ground state for levels below 12 MeV in ^{24}Mg. The dotted line is at 25%.

and $\eta^{NaI,T}_{\gamma ji}$ is the total efficiency in the NaI detector for that transition. For cascade **a**, the number of observed γ–rays for the first excited state to ground state transition in the coincidence Ge spectrum is given by

$$N^{C,Ge}_{\gamma 10} = N\ B_{\gamma 32}B_{\gamma 21}B_{\gamma 10}\ \eta^{Ge,P}_{\gamma 10}\ (\eta^{NaI,T}_{\gamma 32}(1-\eta^{NaI,T}_{\gamma 21}) + \eta^{NaI,T}_{\gamma 21}(1-\eta^{NaI,T}_{\gamma 32}) + \eta^{NaI,T}_{\gamma 32}\eta^{NaI,T}_{\gamma 21}). \quad (6.3)$$

The above may be simplified to yield

$$N^{C,Ge}_{\gamma 10} = N\ B_{\gamma 32}B_{\gamma 21}B_{\gamma 10}\ \eta^{Ge,P}_{\gamma 10}\ (\eta^{NaI,T}_{\gamma 32} + \eta^{NaI,T}_{\gamma 21} - \eta^{NaI,T}_{\gamma 32}\eta^{NaI,T}_{\gamma 21}), \quad (6.4)$$

The first term in Eq. 6.4 occurs when γ_{32} is detected and γ_{21} is not detected. The second term occurs when γ_{21} is detected and γ_{32} is not detected. Final term occurs when γ_{32} and γ_{21} are both detected. Cascade **c** is not of interest since the goal is to observe the transition from the first excited state to the ground state, i.e. γ_{10}.

Results for Eqs. 6.2 and 6.4 may also be obtained from the following more general

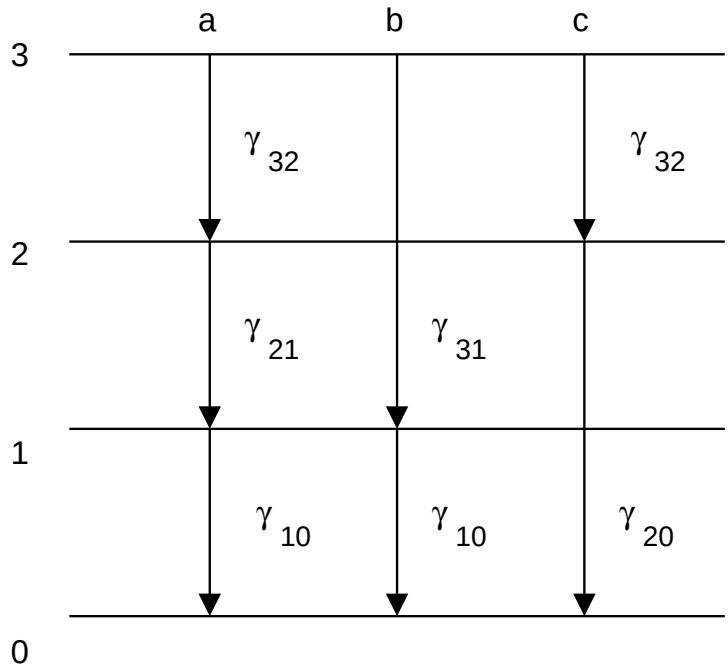

Figure 6.3: A simple decay scheme to illustrate the calculation the the number of observed γ-rays in the first excited state to ground state transition.

expressions:

$$\begin{aligned} \eta_{\gamma 31}^{NaI,T} &= 1-(1-\eta_{\gamma 31}^{NaI,T}) \qquad (6.5) \\ \eta_{\gamma 32}^{NaI,T}+\eta_{\gamma 21}^{NaI,T}-\eta_{\gamma 32}^{NaI,T}\eta_{\gamma 21}^{NaI,T} &= 1-(1-\eta_{\gamma 32}^{NaI,T})(1-\eta_{\gamma 21}^{NaI,T}). \end{aligned}$$

Based on Eqs. 6.2, 6.4, and 6.5, it can be shown [Ili03] that for the general case of an arbitrary γ-decay scheme, the total number of observed decays can be written as

$$N = \frac{N_{\gamma 10}^{Ge,C}}{\eta_{\gamma 10}^{Ge,P} f_\gamma} \qquad (6.6)$$

where the quantity f_γ is given by

$$f_\gamma = \sum_{k\geq 2}\Big(\prod_{i'\,j'} B_{\gamma j' i'}\Big)\Big(1-\prod_{i\,j}(1-\eta_{ji}^{NaI,T})\Big). \qquad (6.7)$$

The summation is over cascades of multiplicity k $\geq$ 2. The first term in parentheses is the product over the branching ratios, including the transition from the first excited state to the ground state. The second product is over the total efficiencies in the NaI

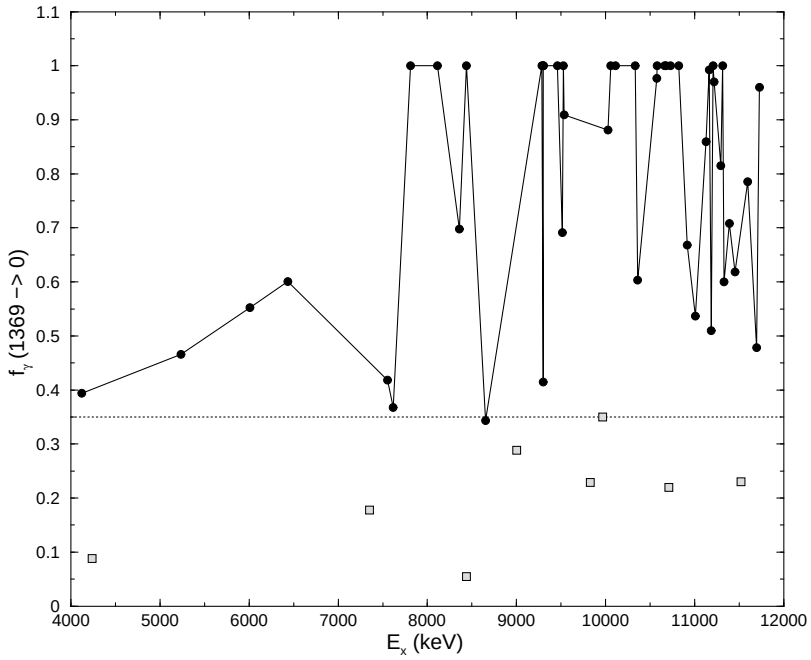

Figure 6.4: Values for f_γ as defined in Eq. 6.7. The dotted line is at 35%. The gray squares indicate levels that proceed directly to the ground state with a branching ratio greater than 50%.

detector, excluding the transition from the first excited state to ground. Values of f_γ for ^{24}Mg levels with $E_x < 12$ MeV are shown in Fig. 6.4. (States which decay directly to the ground state with a probability greater than 50% are indicated by the gray squares.)

Using Eqs. 6.6 and 6.7 an improved upper limit may be obtained from the following,

$$\omega\gamma \;\leq\; \frac{2}{\lambda_{CM}^2}\;\epsilon_{CM}\frac{1}{N_p}\;\left(\frac{N_{\gamma R0}^{Ge,S}}{\eta_{\gamma R0}^{Ge,P}}+\frac{N_{\gamma 10}^{Ge,C}}{\eta_{\gamma 10}^{Ge,P}\;\;f_\gamma}\right). \tag{6.8}$$

From Fig. 6.4, the lowest value of f_γ is ≈ 0.35. This value is taken as a conservative estimate and is used to determine the upper limit of the $E_R = 144$ keV resonance strength via Eq. 6.8. Results of this calculation are presented in 6.3.3.

6.3 Procedure

The search for the $E_R = 144$ keV resonance was performed at LENA with the detectors and electronics described in Ch. 3. Two sodium beamstop targets were

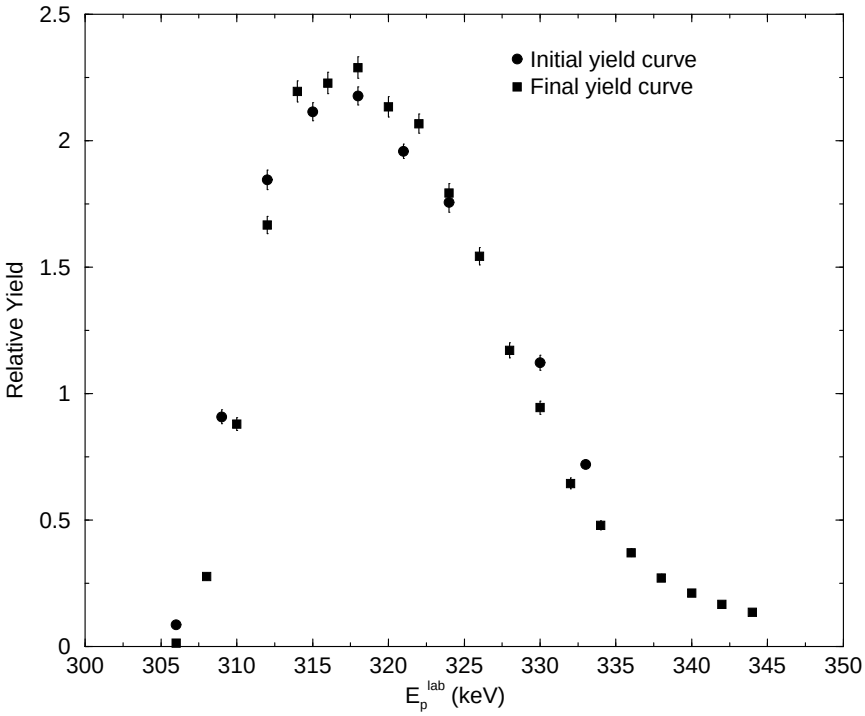

Figure 6.5: Target tests using the $E_R = 144$ keV resonance in ^{23}Na(p,γ)^{24}Mg. The circles show the initial target yield and the squares show the final target yield.

prepared by evaporating Na_2WO_4 onto 0.5-mm-thick tantalum backings. The target thickness was about 16 keV at a bombarding energy of $E_p = 315$ keV. The targets were checked frequently and were found to be stable during the course of the experiment. Fig. 6.5 shows the first and last yield curves taken over the $E_R = 309$ keV resonance.

In addition to the search for the $E_R = 144$ keV resonance, two other resonances were measured in the ^{23}Na(p,γ)^{24}Mg reaction and their strengths were determined according to Eq. 6.8. The results are presented below as well.

6.3.1 Maximum likelihood estimation

In the current literature, only an upper limit is available for the $E_R = 144$ keV resonance strength in ^{23}Na(p,γ)^{24}Mg. Görres et al. established an upper limit for this strength by measuring the upper limit of γ-ray yield for the transition from the first excited state to ground state ($E_\gamma = 1369$ keV) relative to the γ-ray yield of the the $E_R = 309$ keV resonance.

In the present work the $E_R = 144$ keV resonance was searched for at LENA with (lab) proton energies of 133, 146, 149.5, 151, and 153 keV. For each energy between 5 and 6 Coulombs of ion beam charge was accumulated on target. In the final analysis, only the data from $E_p = 149.5$ keV was used, since at higher energies contaminant lines from the $^{18}O(p,\gamma)^{19}F$ reaction appear in the region of interest.

In determining the resonance energy, the Q-value from Audi and Wapstra [Aud95] was used ($Q_{p\gamma} = 11692.9 \pm 0.3$ keV). Endt [End90] gives an excitation energy of $E_x = 11828 \pm 3$ keV, and Hale [Hal99] quotes a value of $E_x = 11831.7 \pm 1.8$ keV. Using the Audi and Wapstra Q-value, the resonance energy (in the laboratory frame) is 141.9 ± 3 keV with the Endt excitation energy, or 145.7 ± 1.8 keV with the Hale excitation energy. In the present work, an average of these two values was assumed. Fig. 6.6 (a) shows a conceptual picture of the relative yield vs. bombarding proton energy and the uncertainty in resonance energy. Fig. 6.6 (b) shows the upper limits obtained for five proton energies.

Fig. 6.7 shows the germanium detector singles and coincidence spectra at $E_p = 149.5$ keV. The coincidence spectrum was obtained with the condition 3.0 MeV $< (E_\gamma^{Ge} + E_\gamma^{NaI}) <$ 13.0 MeV. The dotted line in both spectra indicates where the 1369 keV $\rightarrow$ 0 transition should appear. Even though the background has been reduced in the coincidence spectrum by two orders of magnitude, no statistically significant signal is observed at 1369 keV.

In a case like the present one, where the background is larger than the signal, statistical fluctuations in the background may hide the signal. Hannam et al. [Han99] presents a method for estimating small signals in the presence of large background assuming that both signal and background statistics are Poissonian. This maximum likelihood estimation is used in the present work to determine the number of observed γ–rays at the energies of interest.

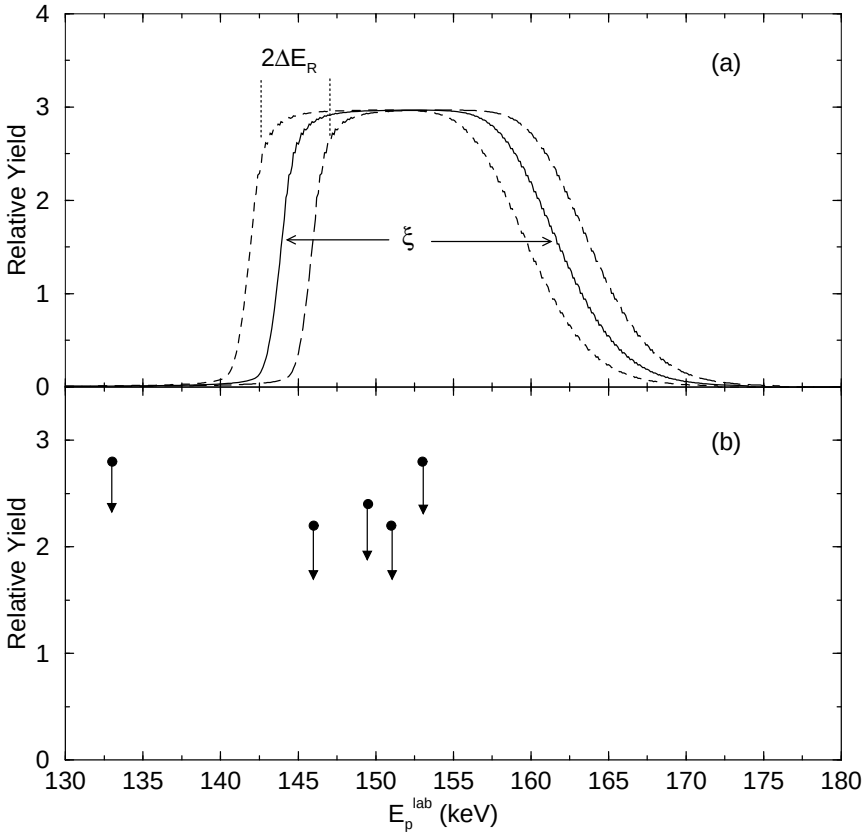

Figure 6.6: (a) Conceptual picture of the relative yield vs. bombarding proton energy to illustrate uncertainty in the assumed resonance energy; (b) measured upper limits for five proton energies.

6.3.2 Detection efficiencies

As discussed in Ch. 4, the calculation of resonance strengths from γ–ray peak intensities observed in singles and coincidence germanium spectra requires reliable detection efficiencies as input. Eq. 6.8 requires the absolute full energy peak efficiency of the Ge detector and the absolute total efficiency of the NaI annulus.

For the germanium detector, absolute full-energy peak efficiencies in the range of $E_\gamma = 0.8$–12.0 MeV were measured by using a calibrated ^{56}Co source as well as resonant γ–rays from the reactions ^{27}Al(p,γ)^{26}Mg (E_R = 406 keV [End90]) and ^{26}Mg(p,γ)^{27}Al (E_R = 338 keV [End90]). The experimental efficiency values are displayed in Fig 6.8 (a). The results have been corrected for coincidence summing effects, since the germanium detector was located in close geometry to the target (Fig. 3.6). Appendix A describes the summing correction procedure. The solid line is a fit to the measured

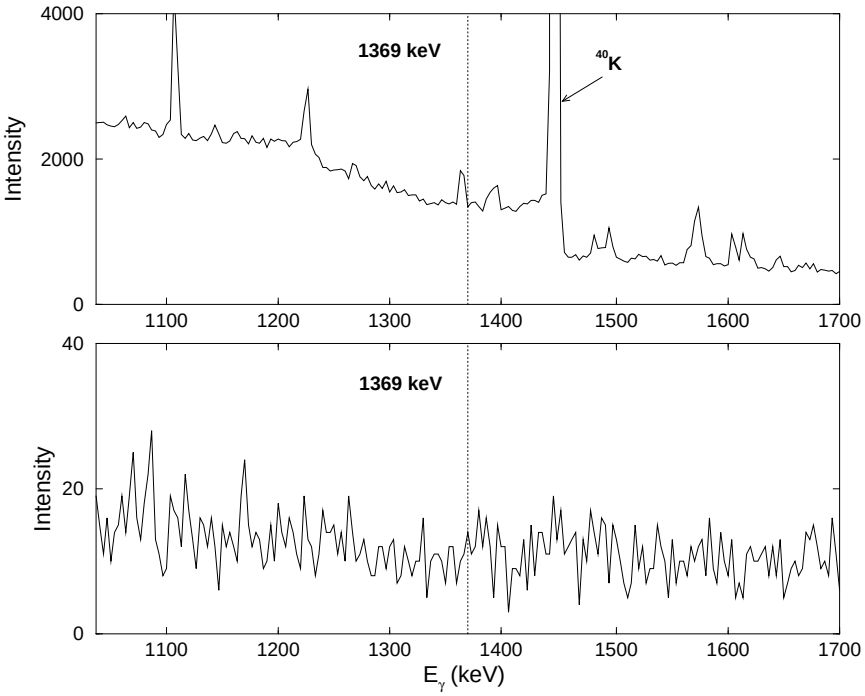

Figure 6.7: Singles and coincidence spectra for E_p = 149.5 keV in the region E_γ^{Ge} = 1050–1700 keV and 5.0 Coulombs on target. The dotted line indicates where the 1369 keV → ground state transition should appear: (a) singles spectrum; (b) coincidence spectrum obtained with the condition 3.0 MeV < (E_γ^{Ge} + E_γ^{NaI}) < 13.0 MeV.

efficiency given by

$$\log(\eta_\gamma^{Ge,p}) = \text{-}2.596 + 1.490\ \log(E_\gamma) \text{ - } 0.341\ \ (\log(E_\gamma))^2.$$

Fig. 6.8 shows that the $\eta_\gamma^{Ge,p}$ values are much higher that the ones shown in Fig. 4.6 since the detector was located in closer geometry. The total efficiency of the germanium detector was determined using the decay of a ^{60}Co. This efficiency is given by [Run03]

$$\eta_\gamma^{Ge,T} = 0.158\ e^{-0.001089} + 0.156.$$

For the NaI annulus, the total efficiency depends on the selected energy window. The procedure for obtaining this efficiency is discussed in Sec. 4.2.3. The coincidence spectrum shown in Fig. 6.7 was obtained with a NaI gate of 3000 keV $\leq E_\gamma^{Ge}+E_\gamma^{NaI} \leq$ 13 MeV. The region of interest in the Ge spectrum is at E_γ^{Ge} = 1369 keV. Therefore re-

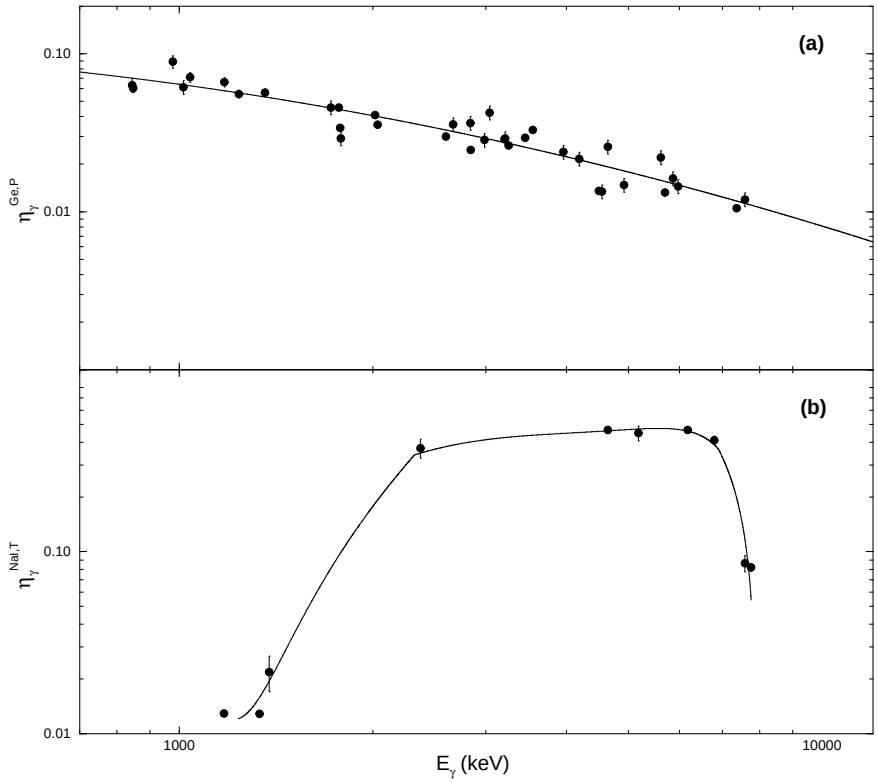

Figure 6.8: (a) Absolute full-energy peak efficiency of germanium detector vs. γ-ray energy; (b) absolute total efficiency of NaI annulus for an energy window of E_{γ}^{NaI} = 1.63–13.0 MeV. The solid lines are fits to the data.

quired in the NaI spectrum is a gate with a lower energy limit of 3000 keV = 1369 keV + E_{γ}^{NaI}, i.e. the lower energy of the NaI gate is E_{γ}^{NaI} = 1631 keV.

A curve of $\eta_{\gamma}^{NaI,T}$ vs. E_{γ} is obtained from resonant γ-rays from the reactions ^{14}N(p,γ)^{15}O (E_R = 278 keV [Run03]) and ^{26}Mg(p,γ)^{27}Al (E_R = 338 keV [End90]), as well as from the decay of ^{60}Co. As seen in Eqs. 4.6 and 4.7, the germanium detector total efficiency is also needed. This was obtained from observing the decay of a calibrated ^{60}Co source. Fig 6.8 (b) shows the absolute total efficiency of the NaI annulus. The solid line is a fit to the efficiency given by,

$$\eta_{\gamma}^{NaI,T} = 40.3 - 6.45\cdot10^{-4}\ E_{\gamma} + 2.66\ E_{\gamma}^{2} \quad \text{for } E_{\gamma} \leq 2.32 \text{ MeV};$$

$$\eta_{\gamma}^{NaI,T} = -1.13 + 1.38\cdot10^{-3}\ E_{\gamma} - 4.64\cdot10^{-7}\ E_{\gamma}^{2} - 3.97\cdot10^{-11}\ E_{\gamma}^{3}$$

$$\text{for } 2.32 \text{ MeV} \leq E_{\gamma} \leq 6.90 \text{ MeV};$$

$$\eta_{\gamma}^{NaI,T} = 2.87 - 3.63\cdot10^{-3}\ E_{\gamma} \quad \text{for } E_{\gamma} \geq 6.90 \text{ MeV}.$$

In order to compare the annulus used in this experiment with the annulus used in the coincidence tests, the total efficiency was found with an energy gate of E_γ^{NaI} = 250–9000 keV, as shown in the upper curve of Fig. 4.6. With this gate, the total efficiency at E_γ^{NaI} = 1332 keV is $\approx$ 55% for the new annulus vs. 35% for the older annulus.

6.3.3 Resonance strengths

The upper limit for the E_R = 144 keV resonance was determined according to Eq. 6.8. The values for $N_{\gamma R0}^{Ge,S}$ and $N_{\gamma 10}^{Ge,C}$ were determined using the maximum likelihood estimation technique and the efficiencies used were discussed in the preceding section. The value for f_γ was taken to be 0.35, as described in Sec. 6.2. The present value for the upper limit of the resonance strength is $\omega\gamma \leq 1.5{\cdot}10^{-7}$ eV. Table 6.1 presents this upper limit and the current literature value. The upper limit in the present work has been reduced by a factor of $\approx$ 33.

In addition to determining an upper limit for the E_R = 144 keV resonance strength, the strengths of the E_R = 251 and 309 keV were also measured. Yield curves for these resonances are shown in Fig. 6.9. Although both the E_R = 251 keV and E_R = 309 keV are both strong enough that an upper limit calculation is not necessary, it is useful to calculate these limits as a test of the presented method. First the resonance strengths were determined in the usual manner (See Sec. 4.2.1) with the singles spectra. Intensities were sum corrected as described in Appendix A. For the 251 and 309 keV resonances, the R $\rightarrow$ 1369 keV transition was used with a branching ratio of B_γ = 0.32 and 0.40 [Boy75], respectively. These strengths agree with literature values and are presented in Table 6.1 under the heading "singles".

The strengths for these two resonances were also determined according to Eq. 6.8. Since the 251 and 309 keV resonances are stronger than the 144 keV resonances, the primary to ground state and the first excited state to ground (1369 keV $\rightarrow$ 0) transitions are seen in the spectra. The values for $N_{\gamma R0}^{Ge,S}$ and $N_{\gamma 10}^{Ge,C}$ in Eq. 6.8 were found by taking the background subtracted area. The quantity f_γ defined in Eq. 6.7 was found to be 0.72 and 0.60 for the 250 and 309 keV resonances, respectively. Branching ratio

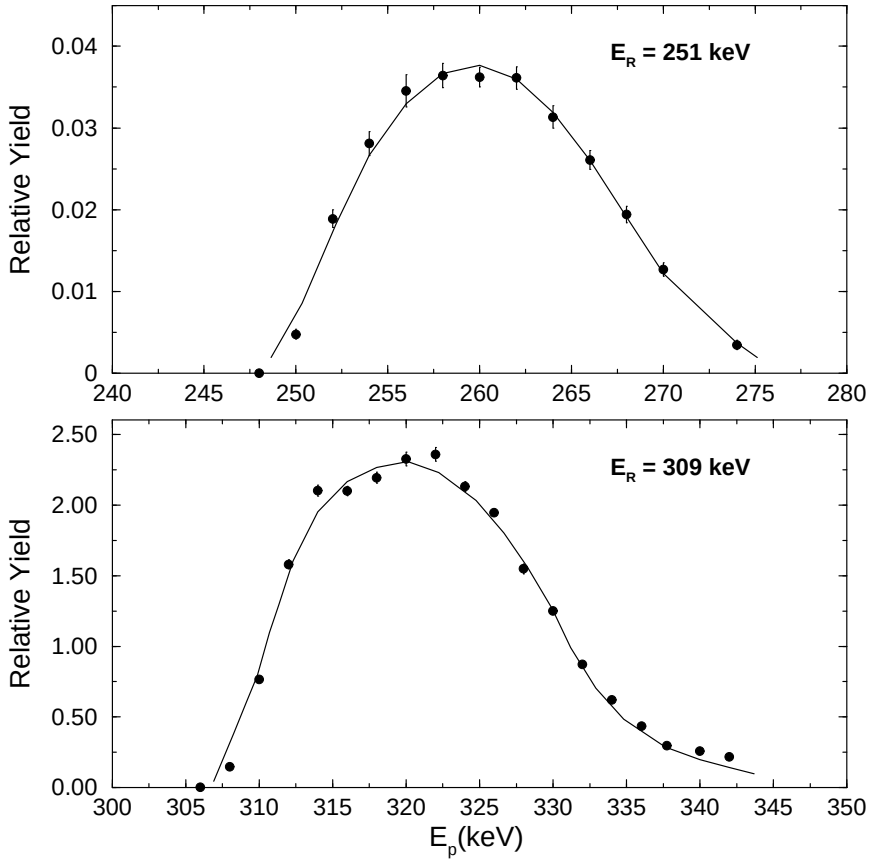

Figure 6.9: Yield curves for the $E_R = 251$ keV and $E_R = 309$ keV resonances. The solid lines are to guide the eye.

information was taken from [Boy75] and [Swi75]. The resulting resonance strengths are presented in Table 6.1 under the heading "coincidence". These values are seen to be smaller than those determined using the singles spectra.

As a final check an upper limit was determined. For this case, the background was not subtracted and the values for $N_{\gamma R0}^{Ge,S}$ and $N_{\gamma 10}^{Ge,C}$ were taken to be the net area in the region of interest. For the case of the 144 keV resonance, the decay scheme is not known. To have a consistent check of the method used to determine the upper limit for that resonance, the quantity f_γ was taken to be 0.35, as described in Sec. 6.2. The resulting upper limits for the strengths are shown in Table 6.1. The values are higher than literature values, which is to be expected. It is unlikely that the strength for this resonance is any larger than the value presented in Table 6.1.

E_R (keV)	$\omega\gamma$ (eV)			
	singles	coincidence	upper limit	literature [Gör89]
144	- - -	- - -	$\leq 1.5 \cdot 10^{-7}$	$\leq 5 \cdot 10^{-6}$
251	$(6.3 \pm 1.5) \cdot 10^{-4}$	$(3.9 \pm 1.0) \cdot 10^{-4}$	$\leq 7.4 \cdot 10^{-4}$	$(6.0 \pm 2.0) \cdot 10^{-4}$
309	$(1.3 \pm 0.3) \cdot 10^{-1}$	$(0.8 \pm 0.2) \cdot 10^{-1}$	$\leq 1.40 \cdot 10^{-1}$	$(1.07 \pm 0.22) \cdot 10^{-1}$

Table 6.1: Strengths for three ^{23}Na(p,γ)^{24}Mg resonances.

Chapter 7

Reaction rates and stellar models

The formalism used to describe the thermonuclear reaction rate has been presented in Ch. 2. In this chapter, the procedure for determining the ^{23}Na(p,α)^{20}Ne and ^{23}Na(p,γ)^{24}Mg reaction rates is discussed in further detail. As mentioned in Ch. 2, for a (p,γ) or (p,α) reaction, the rate is dependent on the total cross section, and the total cross section is determined by the sum of the resonant and nonresonant contributions to the reaction mechanism. These various contributions as well as final results for the reaction rates are presented in Sec. 7.1 and 7.2 for the ^{23}Na(p,α)^{20}Ne and ^{23}Na(p,γ)^{24}Mg reactions, respectively. Sec. 7.3 presents the results of stellar model calculations and the resulting astrophysical implications. Details for both reactions, including Q-values and literature sources are presented in Table 7.1.

7.1 ^{23}Na(p,α)^{20}Ne

In determining the ^{23}Na(p,α)^{20}Ne reaction rate, contributions from narrow resonances (observed and unobserved), broad resonances, and subthreshold resonances were considered. The details of each contribution are presented in Sects. 7.1.1, 7.1.2, and 7.1.3. Results for the ^{23}Na(p,α)^{20}Ne reaction rate are presented in Sec. 7.1.4.

Reaction	Q[a] (keV)	N_R	$E^{Lab}_{R,min}$–$E^{Lab}_{R,max}$ (keV)	Reference[b]
^{23}Na(p,α)^{24}Mg	2376.5 ± 0.2	4	2–175	- - -
		4[c]	179–284	[Gör89]
		44[d]	309–2430	[End90]
^{23}Na(p,γ)^{20}Ne	11692.9 ± 0.2	6[e]	2–223	- - -
		51	251–492	[End90]

Table 7.1: Information for ^{23}Na+p reactions.

[a] Taken from [Aud95].

[b] If no reference is given, the resonances are unobserved.

[c] Except strengths for $E_R = 222$ keV and $E_R = 251$ keV which have been taken from [End90].

[d] Except strength for $E_R = 338$ keV which has been measured in the present work.

[e] Except strength for $E_R = 144$ keV for which an upper limit has been determined in the present work.

7.1.1 Narrow observed resonances

The contribution to the reaction rate from narrow isolated resonances was determined using Eq. 2.15. A total of 48 resonances were used ranging in (lab) energy from 179 to 2430 keV. In the present work, the $E_R = 338$ keV resonance strength was measured. The other resonances used in the narrow resonance rate calculation were normalized to this measured strength. Table 7.1 gives details on the literature sources. If an uncertainty for the resonance strength was not given in the literature, a value of 20% was assumed as a typical experimental error. Table 7.2 shows resonance strengths used for narrow resonances below $E_R = 400$ keV.

7.1.2 Unobserved resonances

Four resonances between 2 and 175 keV are unobserved. Upper limits of the resonance strengths for $E_R = 2.2$, 35.6 and 174.4 keV were calculated from available proton width information from Hale [Hal99] and Endt [End90]. For the $E_R = 144$ keV resonance, Görres *et al.* [Gör89] presents an upper limit for the strength. Resonance

E_x (keV)	E_R^{cm} (keV)	E_R^{Lab} (keV)	$\omega\gamma_{p\alpha}$ (eV)
11864 ± 3	171.1	178.5	$(2.6 \pm 0.8)\cdot10^{-5}$
11906 ± 2	213.1	222.4	$(5.2 \pm 1.2)\cdot10^{-5}$
11964.7 ± 0.8	271.8	283.6	$(3.0 \pm 0.6)\cdot10^{-2}$
11988.0 ± 0.3	295.1	307.9	$(1.0 \pm 0.2)\cdot10^{-2}$
12015.2 ± 0.8	323.4	337.5	$(7.16 \pm 0.90)\cdot10^{-2}$

Table 7.2: ^{23}Na(p,α)^{20}Ne strengths for observed narrow resonances in the energy region $E_R < 400$ keV.

E_x (keV)	E_R^{cm} (keV)	E_R^{Lab} (keV)	$\omega\gamma_{p\alpha}$ (eV)
11695 ± 2	2.1	2.2	$\leq 3.9\cdot10^{-96}$
11727 ± 2	34.1	35.6	$\leq 2.3\cdot10^{-19}$
11828 ± 3	138	144	$\leq 5.0\cdot10^{-7}$
11860 ± 3	167.1	174.4	$\leq 3.7\cdot10^{-8}$

Table 7.3: Resonance strengths for unobserved states in ^{23}Na(p,α)^{20}Ne.

strengths for these states are presented in Table 7.3. In determining the upper limit of the reaction rate, the values presented in Table 7.3 were included in the analysis. For the recommended value of the rate, an estimate for these strengths was obtained by multiplying the upper limits by a factor of 0.1.

7.1.3 Broad and subthreshold resonances

As discussed in Sec. 2.2, a resonance for which $\Gamma/E_R \geq 10\%$ is called a broad resonance. In the present work, the S-factor contribution for low energy tails of broad resonances was calculated for resonances with known strengths and widths for states with energies between 178 and 2430 keV. The calculation was performed with a code written by Iliadis [Ili03]. Resonance strength and width information was taken from Endt [End90] and Hale [Hal99]. For the contribution of broad resonance tails, the S-factor is given by,

E_x (keV)	E_R^{cm} (keV)	J^π	l_p	Γ (keV)	C^2S	θ_α^{2a}
11390	-303	1^-	1	0.5	0.078	0.01
11519	-174	2^+	0	0.5	0.023	0.14

Table 7.4: Information for substhreshold states in ^{23}Na(p,α)^{20}Ne.

[a] Values for θ_α^2 taken from [Ver88]. All other information in table taken from [End90].

$$S(E)_{BR} = 1.01 - 10.3E + \frac{1}{2}884E^2. \quad (7.1)$$

where E is in units of MeV and S is in units of MeV·b. The S-factor given in 7.1 is applicable for energies E $\leq$ 0.125 MeV.

Subthreshold resonances have also been discussed in Sec. 2.2. Such resonances occur when the high-energy wing of a subthreshold state extends above the particle threshold. In the present work, the contribution to the reaction rate of two subthreshold resonances at E_R^{cm} = -174 and -303 keV was considered. Table 7.1.3 gives information for these states. The S-factor was again calculated using the algorithm developed by Iliadis and is found to be,

$$S(E)_{ST} = 4.26 - 21.0E + \frac{1}{2}103.0E^2. \quad (7.2)$$

The S-factor given in 7.1 is applicable for energies E $\leq$ 0.25 MeV.

7.1.4 Results for ^{23}Na(p,α)^{20}Ne

Table 7.5 shows the individual contributions to the total recommended reaction rate from narrow, broad and subthreshold resonances. The values from this table are plotted in Fig. 7.1. Table 7.1.4 gives the lower, upper and recommended values for the total rate as well as the most recent literature values from Iliadis [Ili01]. Fig. 7.3 shows an estimate of the reaction rate uncertainty.

T_9 (keV)	$E_R \geq 174$ keV	$E_R < 179$ keV recommended	broad res.	subthresh.
0.010	$3.13 \cdot 10^{-81}$	$2.45 \cdot 10^{-30}$	$7.19 \cdot 10^{-31}$	$2.50 \cdot 10^{-30}$
0.015	$1.76 \cdot 10^{-53}$	$7.17 \cdot 10^{-25}$	$1.18 \cdot 10^{-25}$	$3.46 \cdot 10^{-25}$
0.020	$1.16 \cdot 10^{-39}$	$3.41 \cdot 10^{-22}$	$2.42 \cdot 10^{-22}$	$5.94 \cdot 10^{-22}$
0.030	$6.42 \cdot 10^{-26}$	$1.36 \cdot 10^{-19}$	$3.62 \cdot 10^{-18}$	$6.50 \cdot 10^{-18}$
0.040	$4.21 \cdot 10^{-19}$	$1.21 \cdot 10^{-17}$	$1.58 \cdot 10^{-15}$	$2.22 \cdot 10^{-15}$
0.050	$4.79 \cdot 10^{-15}$	$1.77 \cdot 10^{-14}$	$1.17 \cdot 10^{-13}$	$1.37 \cdot 10^{-13}$
0.060	$2.31 \cdot 10^{-12}$	$2.50 \cdot 10^{-12}$	- -	$3.13 \cdot 10^{-12}$
0.070	$1.84 \cdot 10^{-10}$	$8.31 \cdot 10^{-11}$	- -	$3.76 \cdot 10^{-11}$
0.080	$4.77 \cdot 10^{-09}$	$1.12 \cdot 10^{-09}$	- -	$2.87 \cdot 10^{-10}$
0.090	$5.89 \cdot 10^{-08}$	$8.27 \cdot 10^{-09}$	- -	$1.59 \cdot 10^{-09}$
0.100	$4.35 \cdot 10^{-07}$	$4.04 \cdot 10^{-08}$	- -	$6.86 \cdot 10^{-09}$
0.150	$2.12 \cdot 10^{-04}$	$4.11 \cdot 10^{-06}$	- -	$1.08 \cdot 10^{-06}$
0.200	$1.09 \cdot 10^{-02}$	$3.65 \cdot 10^{-05}$	- -	$2.30 \cdot 10^{-05}$
0.300	$1.15 \cdot 10^{+00}$	$2.74 \cdot 10^{-04}$	- -	$7.30 \cdot 10^{-04}$
0.400	$1.32 \cdot 10^{+01}$	$6.63 \cdot 10^{-04}$	- -	$3.66 \cdot 10^{-03}$
0.500	$6.85 \cdot 10^{+02}$	$1.04 \cdot 10^{-03}$	- -	$5.90 \cdot 10^{-03}$
0.600	$2.59 \cdot 10^{+02}$	$1.35 \cdot 10^{-03}$	- -	$4.09 \cdot 10^{-03}$
0.700	$7.73 \cdot 10^{+03}$	$1.56 \cdot 10^{-03}$	- -	$1.42 \cdot 10^{-03}$
0.800	$1.89 \cdot 10^{+03}$	$1.69 \cdot 10^{-03}$	- -	$2.70 \cdot 10^{-04}$
0.900	$3.97 \cdot 10^{+03}$	$1.77 \cdot 10^{-03}$	- -	- -
1.000	$7.47 \cdot 10^{+03}$	$1.80 \cdot 10^{-03}$	- -	- -
1.500	$7.03 \cdot 10^{+04}$	$1.66 \cdot 10^{-03}$	- -	- -
2.000	$2.74 \cdot 10^{+05}$	$1.41 \cdot 10^{-03}$	- -	- -

Table 7.5: Recommended ^{23}Na(p,α)^{20}Ne reaction rate from narrow, broad and subthreshold contributions.

T_9 (keV)	$N_A<\sigma\ v>_{low}$	$N_A<\sigma\ v>_{high}$	$N_A<\sigma\ v>^{a}_{rec.}$	$N_A<\sigma\ v>^{b}_{rec.}$
0.010	$3.22{\cdot}10^{-30}$	$2.49{\cdot}10^{-28}$	$5.68{\cdot}10^{-30}$	$5.67{\cdot}10^{-30}$
0.015	$4.64{\cdot}10^{-25}$	$7.22{\cdot}10^{-23}$	$1.18{\cdot}10^{-24}$	$1.18{\cdot}10^{-24}$
0.020	$8.36{\cdot}10^{-22}$	$3.49{\cdot}10^{-20}$	$1.18{\cdot}10^{-21}$	$1.18{\cdot}10^{-21}$
0.030	$1.01{\cdot}10^{-17}$	$2.37{\cdot}10^{-17}$	$1.02{\cdot}10^{-17}$	$1.02{\cdot}10^{-17}$
0.040	$3.80{\cdot}10^{-15}$	$4.14{\cdot}10^{-15}$	$3.81{\cdot}10^{-15}$	$3.81{\cdot}10^{-15}$
0.050	$2.59{\cdot}10^{-13}$	$4.37{\cdot}10^{-13}$	$2.76{\cdot}10^{-13}$	$2.78{\cdot}10^{-13}$
0.060	$5.44{\cdot}10^{-12}$	$3.04{\cdot}10^{-11}$	$7.94{\cdot}10^{-12}$	$8.71{\cdot}10^{-12}$
0.070	$2.22{\cdot}10^{-10}$	$1.05{\cdot}10^{-09}$	$3.05{\cdot}10^{-10}$	$3.65{\cdot}10^{-10}$
0.080	$5.06{\cdot}10^{-09}$	$1.63{\cdot}10^{-08}$	$6.18{\cdot}10^{-09}$	$7.77{\cdot}10^{-09}$
0.090	$6.05{\cdot}10^{-08}$	$1.43{\cdot}10^{-07}$	$6.88{\cdot}10^{-08}$	$8.85{\cdot}10^{-08}$
0.100	$4.42{\cdot}10^{-07}$	$8.46{\cdot}10^{-07}$	$4.82{\cdot}10^{-07}$	$6.27{\cdot}10^{-07}$
0.150	$2.13{\cdot}10^{-04}$	$2.54{\cdot}10^{-04}$	$2.17{\cdot}10^{-04}$	$2.89{\cdot}10^{-04}$
0.200	$1.09{\cdot}10^{-02}$	$1.13{\cdot}10^{-02}$	$1.10{\cdot}10^{-02}$	$1.47{\cdot}10^{-02}$
0.300	$1.15{\cdot}10^{+00}$	$1.15{\cdot}10^{+00}$	$1.15{\cdot}10^{+00}$	$1.55{\cdot}10^{+00}$
0.400	$1.32{\cdot}10^{+01}$	$1.32{\cdot}10^{+01}$	$1.32{\cdot}10^{+01}$	$1.81{\cdot}10^{+01}$
0.500	$6.85{\cdot}10^{+01}$	$6.85{\cdot}10^{+01}$	$6.85{\cdot}10^{+01}$	$1.00{\cdot}10^{+02}$
0.600	$2.59{\cdot}10^{+02}$	$2.59{\cdot}10^{+02}$	$2.59{\cdot}10^{+02}$	$4.10{\cdot}10^{+02}$
0.700	$7.73{\cdot}10^{+02}$	$7.73{\cdot}10^{+02}$	$7.73{\cdot}10^{+02}$	$1.27{\cdot}10^{+03}$
0.800	$1.89{\cdot}10^{+03}$	$1.89{\cdot}10^{+03}$	$1.89{\cdot}10^{+03}$	$3.15{\cdot}10^{+03}$
0.900	$3.97{\cdot}10^{+03}$	$3.97{\cdot}10^{+03}$	$3.97{\cdot}10^{+03}$	$6.55{\cdot}10^{+03}$
1.000	$7.47{\cdot}10^{+03}$	$7.47{\cdot}10^{+03}$	$7.47{\cdot}10^{+03}$	$1.20{\cdot}10^{+04}$
1.500	$7.03{\cdot}10^{+04}$	$7.03{\cdot}10^{+04}$	$7.03{\cdot}10^{+04}$	$9.30{\cdot}10^{+04}$
2.000	$2.74{\cdot}10^{+05}$	$2.74{\cdot}10^{+05}$	$2.74{\cdot}10^{+05}$	$3.20{\cdot}10^{+05}$

Table 7.6: Upper, lower, recommended and literature reaction rate for ^{23}Na(p,α)^{20}Ne.

[a] Present work

[b] Literature [Ili01]

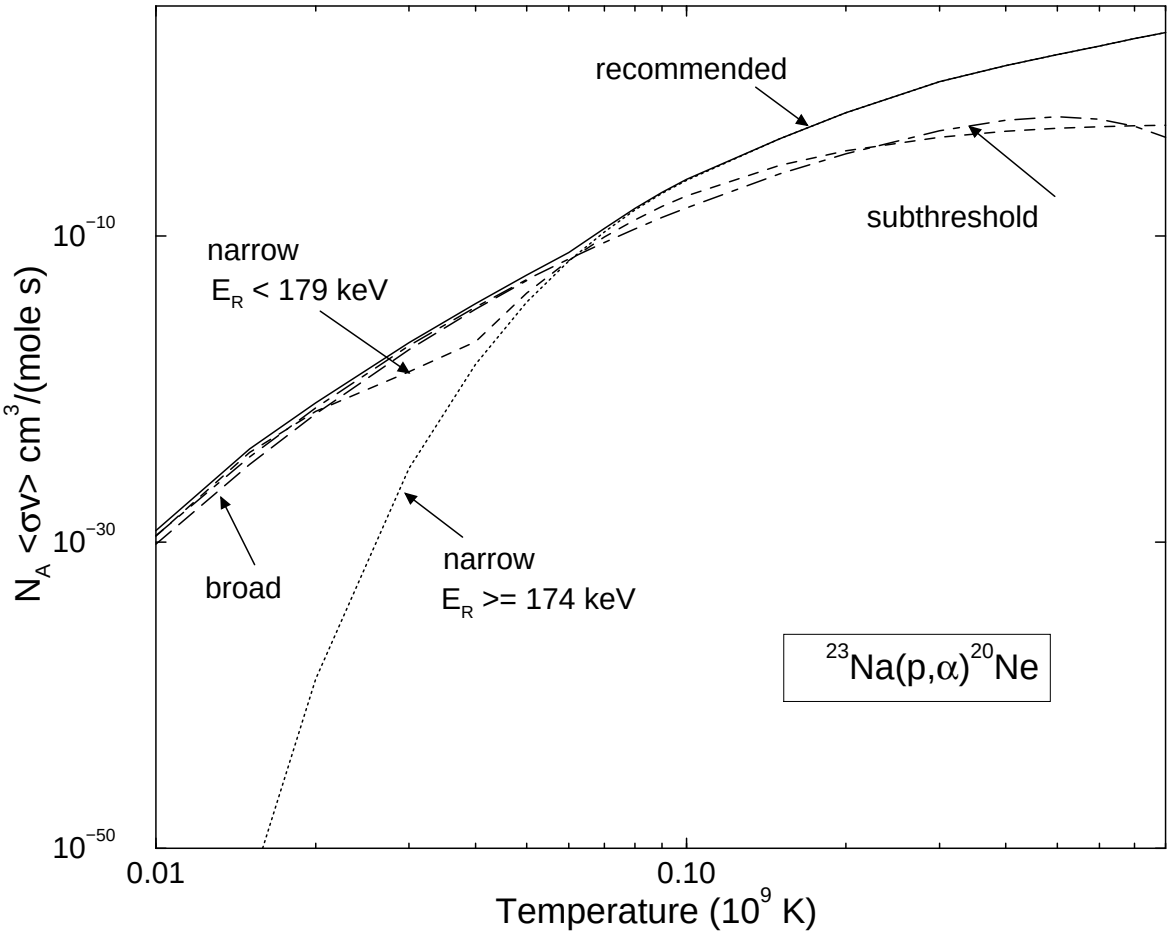

Figure 7.1: Contributions to the ^{23}Na(p,α)^{20}Ne reaction rate from narrow, broad, and subthreshold resonances. Total recommended rate is given by the solid line.

7.2 ^{23}Na(p,γ)^{24}Mg

In determining the ^{23}Na(p,γ)^{24}Mg reaction rate, contributions from narrow resonances (observed and unobserved) and direct capture were considered. Rate values coming solely from subthreshold resonances are not presented here since this contribution was found to be negligible compared to direct capture.

The details for the narrow resonances are presented in Sects. 7.2.1 and 7.2.2. The direct capture contribution is discussed in Sec. 7.2.3. Results for the ^{23}Na(p,γ)^{24}Mg reaction rate are presented in Sec. 7.2.4.

E_x (keV)	E_R^{cm} (keV)	E_R^{Lab} (keV)	$\omega\gamma_{p\gamma}$ (eV)
11931.2 ± 0.6	239.7	250.1	(6 ± 2)·10−4
11987.0 ± 0.3	295.1	308.8	0.104 ± 0.022
12049.4 ± 0.7	358.7	374.3	$(1.37 \pm 2.7)\cdot 10^{-3}$

Table 7.7: ^{23}Na(p,γ)^{24}Mg strengths for observed narrow resonances in the energy region $E_R < 400$ keV.

7.2.1 Narrow observed resonances

The contribution to the reaction rate from narrow isolated resonances was again determined using 2.15. A total of 51 resonances were used ranging in (lab) energy from 249 to 2492 keV. Table 7.1 gives details on the literature sources. If an uncertainty for the resonance strength was not given in the literature, a value of 20% was assumed as a typical experimental error. The resonance strengths for E_R = 251 and 309 keV were determined experimentally in the present work and these measurements have been described in Ch. 6. The contribution to the total reaction rate from observed narrow resonances was determined as described above in Sec. 7.1.1. Table 7.7 lists the strengths used for resonances below E_R = 400 keV.

7.2.2 Unobserved resonances

Six resonances between 2 and 223 keV are unobserved. Upper limits of the resonance strengths for E_R = 2.2, 35.6, 174.4, 178.5, and 222.4 keV resonances were calculated from available width information from Endt [End90] and Hale [Hal99]. In the case of ^{23}Na$(p,\gamma)^{24}$Mg, the largest source of uncertainty in the reaction rate comes from a resonance at E_R = 144 keV. This resonance was searched for at LENA and an improved upper limit was determined as described in Ch. 6. Resonance strengths for unobserved states are presented in Table 7.8. In determining the upper limit of the reaction rate, the values presented in Table 7.8 were used in the analysis. For the recommended value of the rate, an estimate for these strengths was obtained by multiplying the upper limits by a factor of 0.1.

E_x (keV)	E_R^{cm} (keV)	E_R^{Lab} (keV)	$\omega\gamma_{p\gamma}$ (eV)
11695 ± 2	2.1	2.2	$\leq 3.4{\cdot}10^{-97}$
11727 ± 2	34.1	35.6	$\leq 8.3{\cdot}10^{-24}$
11828 ± 3	138	144	$\leq 1.5{\cdot}10^{-7}$ [a]
11860 ± 3	167.1	174.4	$\leq 3.7{\cdot}10^{-8}$
11864 ± 3	171.1	178.5	$\leq 1.3{\cdot}10^{-9}$
11906 ± 2	213.1	222.4	$\leq 6.9{\cdot}10^{-5}$

Table 7.8: Resonance strengths for unobserved states in ^{23}Na(p,γ)^{24}Mg.

[a] From present work; see Table 6.1.

7.2.3 Direct capture

The direct capture contribution to the ^{23}Na(p,γ)^{24}Mg reaction rate was determined according to the formalism described in Ch. 2. The spectroscopic factors and quantum numbers for states between 0 and 11453 keV were taken from [End90]. The S-factor for each state was calculated for energies between 100 and 900 keV with the algorithm provided by [Ili03]. Each state's S-factor is weighted by C^2S, where C^2 is the isospin Clebsch-Gordan coefficient and S in this case is the spectroscopic factor. The weighted S-factors are summed for all states for each energy and the curve of S(E) is fitted according to,

$$S(E) \;=\; S(0) + E\dot{S}(0) + \frac{1}{2}\ddot{S}(0)E^2. \tag{7.3}$$

Using this technique, the S-factor for direct capture in the energy range E $\leq$ 1 MeV was found to be,

$$S(E)_{DC} \;=\; 0.0248 \;-\; 0.00731\ E \;+\; \frac{1}{2}\ 0.0321\ E^2. \tag{7.4}$$

7.2.4 Results for ^{23}Na(p,γ)^{24}Mg

Table 7.9 shows the individual contributions to the total recommended reaction rate from narrow resonances and direct capture. The values from this table are plotted

in Fig. 7.2. Table 7.2.4 gives the lower, upper and recommended values for the total rate as well as the most recent literature values from Iliadis [Ili01]. Fig. 7.3 shows an estimate of the reaction rate uncertainty. The dotted lines show the uncertainty from the most recent literature values [Ili01] and the solid lines indicate the present work. Clearly, the uncertainty in the ^{23}Na(p,γ)^{24}Mg reaction rate has been improved significantly. In particular, the lower limit of this rate has been brought up by over an order of magnitude. Fig. 7.4 shows the ratio of the (p,α) rate to the (p,γ) rate for the new values. The dotted lines indicate recent literature values [Ili01] and the solid lines indicate the present work. Again there is an improvement in the uncertainties. For temperatures of astrophysical interest, the ^{23}Na(p,α)^{20}Ne rate appears to dominate.

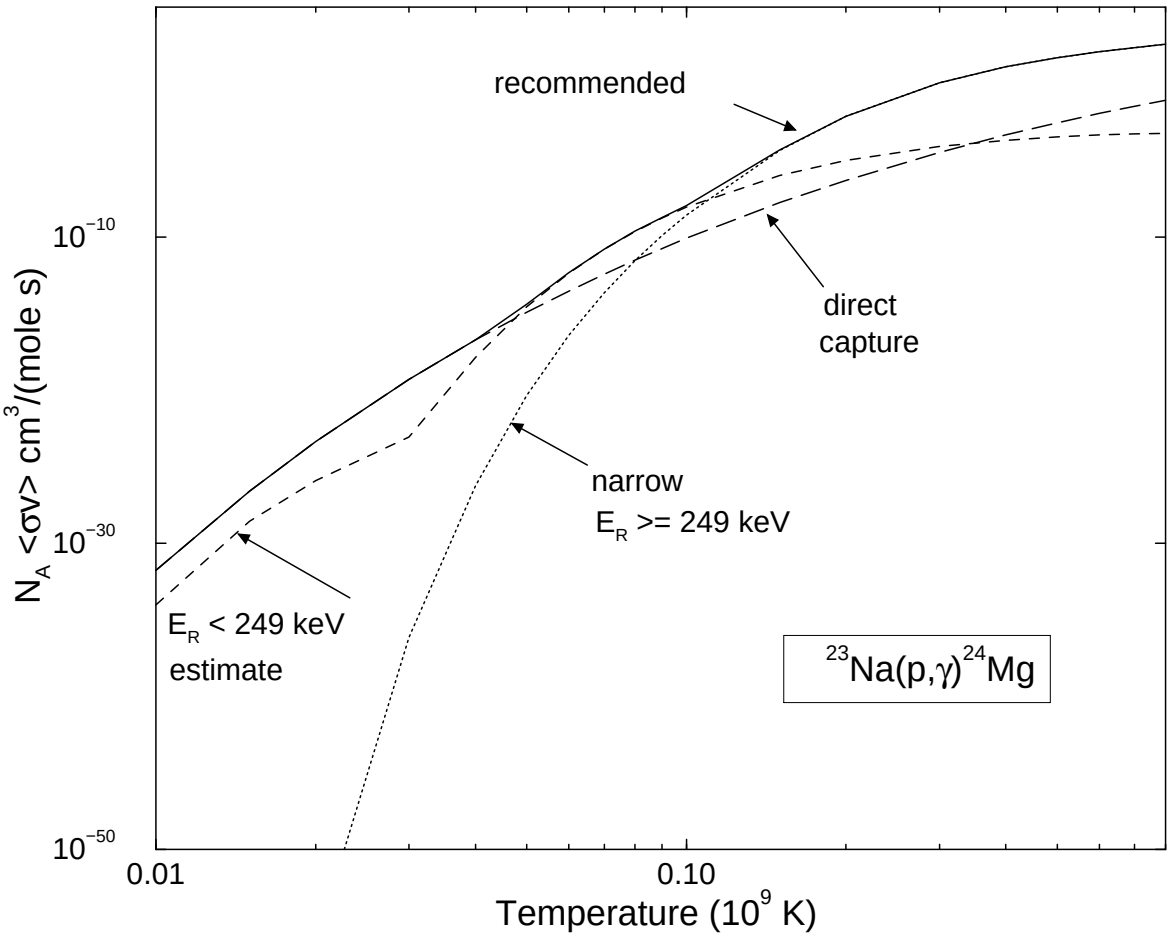

Figure 7.2: Contributions to the ^{23}Na(p,γ)^{24}Mg reaction rate for narrow resonances and direct capture. Total rate is given by the solid line.

T_9 (keV)	$E_R \geq 249$ keV	$E_R < 249$ keV recommended	direct capture
0.010	$5.64 \cdot 10^{-117}$	$8.87 \cdot 10^{-35}$	$1.64 \cdot 10^{-32}$
0.015	$7.61 \cdot 10^{-77}$	$2.59 \cdot 10^{-29}$	$2.38 \cdot 10^{-27}$
0.020	$7.79 \cdot 10^{-57}$	$1.23 \cdot 10^{-26}$	$4.24 \cdot 10^{-24}$
0.030	$6.68 \cdot 10^{-37}$	$8.25 \cdot 10^{-24}$	$5.00 \cdot 10^{-20}$
0.040	$5.45 \cdot 10^{-27}$	$1.33 \cdot 10^{-18}$	$1.83 \cdot 10^{-17}$
0.050	$4.47 \cdot 10^{-21}$	$2.83 \cdot 10^{-15}$	$1.21 \cdot 10^{-15}$
0.060	$3.74 \cdot 10^{-17}$	$4.47 \cdot 10^{-13}$	$2.93 \cdot 10^{-14}$
0.070	$2.31 \cdot 10^{-14}$	$1.63 \cdot 10^{-11}$	$3.74 \cdot 10^{-13}$
0.080	$2.88 \cdot 10^{-12}$	$2.40 \cdot 10^{-10}$	$3.04 \cdot 10^{-12}$
0.090	$1.26 \cdot 10^{-10}$	$1.95 \cdot 10^{-09}$	$1.79 \cdot 10^{-11}$
0.100	$2.74 \cdot 10^{-09}$	$1.05 \cdot 10^{-08}$	$8.19 \cdot 10^{-11}$
0.150	$4.62 \cdot 10^{-05}$	$1.01 \cdot 10^{-06}$	$1.75 \cdot 10^{-08}$
0.200	$7.56 \cdot 10^{-03}$	$1.01 \cdot 10^{-05}$	$5.05 \cdot 10^{-07}$
0.300	$1.17 \cdot 10^{+00}$	$8.06 \cdot 10^{-05}$	$3.33 \cdot 10^{-05}$
0.400	$1.31 \cdot 10^{+01}$	$2.41 \cdot 10^{-04}$	$4.56 \cdot 10^{-04}$
0.500	$5.25 \cdot 10^{+01}$	$4.80 \cdot 10^{-04}$	$2.89 \cdot 10^{-03}$
0.600	$1.28 \cdot 10^{+02}$	$7.70 \cdot 10^{-04}$	$1.17 \cdot 10^{-02}$
0.700	$2.39 \cdot 10^{+02}$	$1.09 \cdot 10^{-03}$	$3.54 \cdot 10^{-02}$
0.800	$3.82 \cdot 10^{+02}$	$1.42 \cdot 10^{-03}$	$8.77 \cdot 10^{-02}$
0.900	$5.53 \cdot 10^{+02}$	$1.74 \cdot 10^{-03}$	$1.87 \cdot 10^{-01}$
1.000	$7.52 \cdot 10^{+02}$	$2.06 \cdot 10^{-03}$	$3.58 \cdot 10^{-01}$
1.500	$2.19 \cdot 10^{+03}$	$1.67 \cdot 10^{-03}$	$3.31 \cdot 10^{+00}$
2.000	$4.39 \cdot 10^{+03}$	$1.56 \cdot 10^{-03}$	$1.22 \cdot 10^{+01}$

Table 7.9: Recommended ^{23}Na(p,γ)^{24}Mg reaction rate from narrow and direct capture contributions.

T_9 (keV)	$N_A<\sigma\ v>_{low}$	$N_A<\sigma\ v>_{high}$	$N_A<\sigma\ v>^{a}_{rec.}$	$N_A<\sigma\ v>^{b}_{rec.}$
0.010	$1.64{\cdot}10^{-32}$	$2.53{\cdot}10^{-32}$	$1.65{\cdot}10^{-32}$	$1.66{\cdot}10^{-32}$
0.015	$2.38{\cdot}10^{-27}$	$4.97{\cdot}10^{-27}$	$2.41{\cdot}10^{-27}$	$2.42{\cdot}10^{-27}$
0.020	$4.24{\cdot}10^{-24}$	$5.47{\cdot}10^{-24}$	$4.25{\cdot}10^{-24}$	$4.29{\cdot}10^{-24}$
0.030	$5.00{\cdot}10^{-20}$	$5.05{\cdot}10^{-20}$	$5.00{\cdot}10^{-20}$	$5.07{\cdot}10^{-20}$
0.040	$1.83{\cdot}10^{-17}$	$3.16{\cdot}10^{-17}$	$1.96{\cdot}10^{-17}$	$1.16{\cdot}10^{-16}$
0.050	$1.25{\cdot}10^{-15}$	$2.95{\cdot}10^{-14}$	$4.04{\cdot}10^{-15}$	$1.78{\cdot}10^{-13}$
0.060	$3.56{\cdot}10^{-14}$	$4.48{\cdot}10^{-12}$	$4.74{\cdot}10^{-13}$	$2.50{\cdot}10^{-11}$
0.070	$6.25{\cdot}10^{-13}$	$1.60{\cdot}10^{-10}$	$1.63{\cdot}10^{-11}$	$8.31{\cdot}10^{-10}$
0.080	$9.25{\cdot}10^{-12}$	$2.30{\cdot}10^{-09}$	$2.33{\cdot}10^{-10}$	$1.12{\cdot}10^{-08}$
0.090	$1.71{\cdot}10^{-10}$	$1.82{\cdot}10^{-08}$	$1.90{\cdot}10^{-09}$	$8.28{\cdot}10^{-08}$
0.100	$2.96{\cdot}10^{-09}$	$9.83{\cdot}10^{-08}$	$1.17{\cdot}10^{-08}$	$4.06{\cdot}10^{-07}$
0.150	$4.62{\cdot}10^{-05}$	$6.99{\cdot}10^{-05}$	$4.72{\cdot}10^{-05}$	$8.70{\cdot}10^{-05}$
0.200	$7.56{\cdot}10^{-03}$	$8.20{\cdot}10^{-03}$	$7.57{\cdot}10^{-03}$	$7.92{\cdot}10^{-03}$
0.300	$1.17{\cdot}10^{+00}$	$1.19{\cdot}10^{+00}$	$1.17{\cdot}10^{+00}$	$1.17{\cdot}10^{+00}$
0.400	$1.31{\cdot}10^{+01}$	$1.32{\cdot}10^{+01}$	$1.31{\cdot}10^{+01}$	$1.31{\cdot}10^{+01}$
0.500	$5.25{\cdot}10^{+01}$	$5.27{\cdot}10^{+01}$	$5.25{\cdot}10^{+01}$	$5.25{\cdot}10^{+01}$
0.600	$1.28{\cdot}10^{+02}$	$1.28{\cdot}10^{+02}$	$1.28{\cdot}10^{+02}$	$1.28{\cdot}10^{+02}$
0.700	$2.39{\cdot}10^{+02}$	$2.40{\cdot}10^{+02}$	$2.39{\cdot}10^{+02}$	$2.39{\cdot}10^{+02}$
0.800	$3.82{\cdot}10^{+02}$	$3.83{\cdot}10^{+02}$	$3.82{\cdot}10^{+02}$	$3.82{\cdot}10^{+02}$
0.900	$5.53{\cdot}10^{+02}$	$5.54{\cdot}10^{+02}$	$5.53{\cdot}10^{+02}$	$5.53{\cdot}10^{+02}$
1.000	$7.52{\cdot}10^{+02}$	$7.53{\cdot}10^{+02}$	$7.52{\cdot}10^{+02}$	$7.52{\cdot}10^{+02}$
1.500	$2.19{\cdot}10^{+03}$	$2.19{\cdot}10^{+03}$	$2.19{\cdot}10^{+03}$	$2.19{\cdot}10^{+03}$
2.000	$4.40{\cdot}10^{+03}$	$4.40{\cdot}10^{+03}$	$4.40{\cdot}10^{+03}$	$4.40{\cdot}10^{+03}$

Table 7.10: Upper, lower, recommended and literature reaction rate for ^{23}Na(p,γ)^{24}Mg.

[a] Present work

[b] Literature [Ili01]

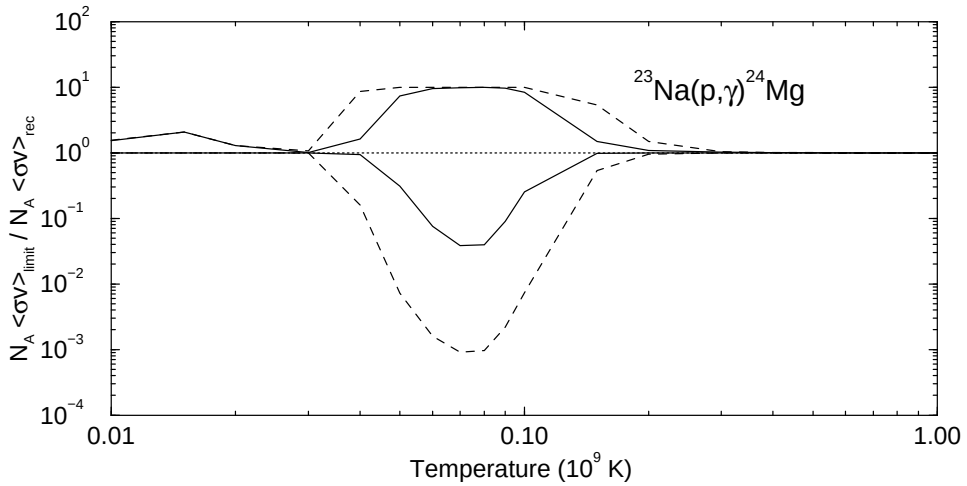

Figure 7.3: Ratio of the upper and lower limits of the ^{23}Na$(p,\gamma)^{24}$Mg reaction rate to the recommended value vs. temperature.as an estimate of rate uncertainty. Solid lines indicate the present work and dotted lines indicate the most recent literature values [Ili01].

7.3 Stellar models and reaction network

As discussed in Ch. 1, the standard model of stellar evolution predicts that there should be little change in the surface abundances of red giants within a monometallic globular cluster. Contrary to predictions, however, there are wide star-to-star variations in the abundances of elements such as C, N, O, Na, and Al. Some of these variations are related to evolutionary state and suggest that some extra process is responsible for the anomalies. Other variations could be due to primordial differences, possibly caused by nucleosynthesis in stars of a previous generation enriching the material that formed the cluster.

The present work uses the nuclear reaction network and stellar sequences of Cavallo *et al.* [Cav98] with the updated reaction rates to determine the effects on the predicted abundances. Three of the stellar sequences presented in Cavallo *et al.* cover the range of metallicities seen in globular clusters and one corresponds to an old disk star with solar metallicity. The masses of the globular cluster sequences are chosen to give an age of ≈ 15 Gyr at the tip of the RGB. The sequences are begun at the zero-age main sequence and are evolved up the red giant branch (RGB) to the He flash at the tip of the RGB (see Fig. 1.1). Each model provides the temperature and density around

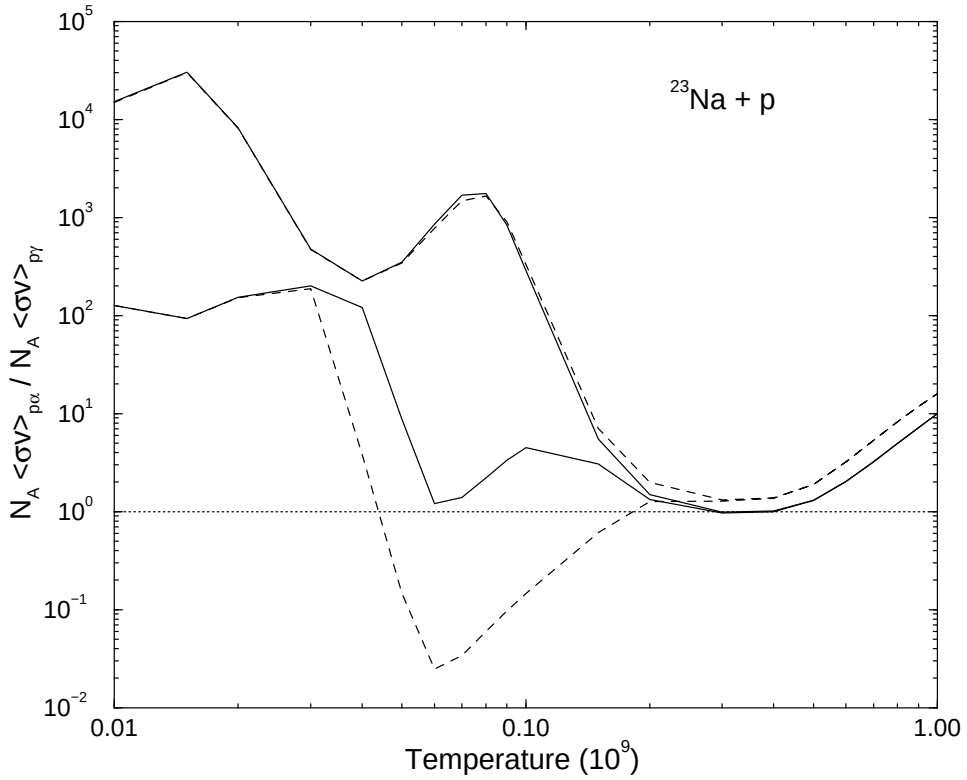

Figure 7.4: Ratio of the (p,α) rate to the (p,γ) rate vs. temperature. Solid lines indicate the present work and dotted lines indicate the most recent literature values [Ili01].

the hydrogen shell as well as the hydrogen shell luminosity, effective temperature and age. The properties of the sequences are shown in Table 7.11. The reaction network requires the temperatures and densities from the stellar model, the initial abundances in the envelope, and the nuclear reaction rates. Isotopes from F through Ca are scaled to solar abundance and are supplied as an initial composition. The envelope values of the C, N, and O isotopes are given by the models and include the effects of the first dredge up at the base of the RGB. The network follows the reactions of 113 nuclei from ^{1}H to ^{49}Ca and produces abundance profiles in the region of the H shell for each model.

The reaction network has been run with updated reaction rates from the present work for ^{23}Na(p,α)^{20}Ne and ^{23}Na(p,γ)^{24}Mg. Most of the rates used in these calculations were taken from Iliadis [Ili01]. Reaction rates not presented in [Ili01] were taken from the NACRE compilation [Ang99]. As mentioned earlier, the largest source of

Z	[Fe/H][a]	M($M_\odot$)	log L^b_{mix} ($M_\odot$)	log L^c_{tip} ($M_\odot$)
0.0001	-2.27	0.795	2.28	3.22
0.0004	-1.67	0.800	2.11	3.26
0.004	-0.67	0.875	1.72	3.33
0.01685	0.00	1.500	1.83	3.34

Table 7.11: Properties of the RGB stellar models. Z indicates the number abundance relative to all metals.

[a] [Fe/H] = log(Fe/H)$_*$ - log(Fe/H)$_\odot$.

[b] Luminosity at the start of mixing.

[c] Luminosity at the tip of the RGB.

uncertainty in the ^{23}Na(p,γ)^{24}Mg reaction rate comes from the resonance at $E_R = 144$ keV. The questions that arise are (1) how much does the new upper limit affect the predicted abundance profiles? and (2) how important is the remaining uncertainty in the rate?

To explore the first question, the recommended ^{23}Na+p rates from the present work were used in the nuclear reaction network for each of the above described stellar sequences. The resulting abundance profiles may be compared to those obtained using the most recent reaction rates in the literature [Ili01]. The results for the NeNa and MgAl mass regions are shown in Figs. 7.5 and 7.6, respectively. The first column of plots show the abundance profiles for the NeNa cycle isotopes at the presumed start of mixing for the four stellar sequences. Each row in this figure represents a different stellar sequence. The top row is the most metal-poor sequence and the bottom row is the least metal-poor (the old disk star with solar metallicity). The second and third columns show the abundance profiles at the tip of RGB obtained using the literature values for the reaction rates [Ili01] and those obtained with the rates from the present work, respectively. The ordinate is the number abundance relative to all metals. The abscissa, ΔS, is the mass difference between any point and the center of the H-shell divided by the H-shell thickness. The "top", "center", and "base" of the H shell always appear at $\Delta S = 1$, 0, and -1, respectively [Cav98]. The arrows indicate the center of

the oxygen shell, defined as the point where the ^{16}O abundance is half of its initial value.

As can be seen in Fig. 7.5, the abundances of Na and Mg are very sensitive to the metallicity of the stellar sequence. Clearly there is much more processing occurring for the low-metallicity sequence where temperatures are higher. At temperatures of interest, the ^{23}Na(p,γ)^{24}Mg reaction rate determined in the present work is as much 50 times smaller than the literature rate. Therefore it is expected that the abundance of ^{24}Mg should be enhanced in the calculations that use the literature reaction rates. This can be seen in Fig 7.5 for the two low metallicity sequences (Z=0.0001 and 0.0004). The abundance of ^{24}Mg obtained using the literature rates is strongly enhanced in a region just above the H-shell compared to the abundance obtained from rates used in the present work. Also, the ^{23}Na abundance for these lower metallicity sequences is larger in the present work, as expected from the smaller ^{23}Na(p,γ)^{24}Mg rate.

Fig. 7.5 also indicates the location of the center of the O-shell (arrows). It can be seen that the center of the O-shell moves away from the H-shell with increasing luminosity and decreasing metallicity. The ^{23}Na abundance becomes more strongly enhanced in only the two most metal-poor sequences. The enhancement is close to the center of the H-shell and well below the center of the O-shell. To reach this region of enhanced ^{23}Na would require deep mixing into the O depleted region, which implies that large Na enhancements should be accompanied by large O depletions. This precisely what is seen in the globular cluster M13 (see Fig. 1.2).

Fig. 7.6 shows abundance profiles for the MgAl mass region. Again, the abundances are very sensitive to the metallicity of the stellar sequence. For the lowest metallicity sequence (Z=0.0001), the abundance of ^{27}Al just below the H-shell is nearly a factor of two larger using the literature rates. This is to be expected since the literature rate of ^{23}Na(p,γ)^{24}Mg is so much larger than the rate determined in the present work. The larger rate clearly allows for more leakage into the MgAl cycle resulting in an enhancement of Al. For the higher metallicity sequences where processing is less robust, the abundances obtained using the literature rates are comparable to those obtained using rates from the present work. It should be noted that the ^{27}Al enhancements

occur below or at the base of the H-shell. Therefore, the depletion of Mg and the large enhancements of Al seen at the surface of globular cluster red giant stars are likely the result of mixing deep within the H-shell during the latter half of the RGB lifetime.

The second question addresses how important the remaining uncertainty in the ^{23}Na(p,γ)^{24}Mg reaction rate is for the predicted abundances. To explore this issue, the ^{23}Na(p,γ)^{24}Na reaction rate was first calculated excluding the 144 keV resonance and the network was run for the above described stellar sequences. The resulting abundance profiles using this lower limit may then be compared to those obtained using the upper limit of the ^{23}Na(p,γ)^{24}Mg reaction rate. The results are shown in Fig. 7.7. The profiles obtained from the upper limit are very similar to those obtained with reaction rates from the literature (center column of Fig. 7.5). As expected, for the upper limit, the ^{24}Mg abundance is enhanced, particularly for the two lowest metallicity sequences. For profiles obtained using rates from the present work, there is a modest enhancement of ^{23}Na and a slightly lower yield of ^{20}Ne compared to the upper limit values. Again, the region of enhanced ^{23}Na is below the O-shell and near the H-shell center.

For the MgAl mass region shown if in Fig. 7.8, the abundance profiles obtained for the upper limit are again very similar to those obtain with the reaction rates from the literature (center column of Fig. 7.6). The upper limit calculations show an enhancement in the Al isotopes, as expected. Again the ^{27}Al enhancements occur below or near the base of the H-shell, suggesting that the observed Mg-Al anticorrelation is indeed the result of deep mixing.

An analysis of the reaction network results shows a modest variation caused by the remaining uncertainty in the ^{23}Na(p,α)^{20}Ne and ^{23}Na(p,γ)^{24}Mg reaction rates. It is important to decrease the rate uncertainties further, particularly in the case of ^{23}Na(p,γ)^{24}Mg. Improvements in beam current and target fabrication may allow for the detection of the E_R = 144 keV, or a further reduction of the upper limit. Even with the most accurate reaction rates there is still much work to do in area of stellar modeling. Cavallo *et al.* have developed software which will subject the stellar sequences to a mixing algorithm. It will be very interesting to see the results on this

software when the most reliable of reaction rates are used.

The motivation for this work was based on observations of globular cluster red giant stars, although the ^{23}Na+p reaction rates are very important for other scenarios as well, such as nucleosynthesis associated with AGB stars and novae explosions. Clearly, systematic studies of an even larger number of globular cluster stars would be very useful. At present, many of the reported anomalies are based on few stars in a particular cluster. Extracting reliable abundances from cluster stars is difficult, but terribly important in the effort to understand the details of stellar evolution. As equipment and techniques improve, both in observational astronomy and in experimental nuclear physics, it becomes more likely that the star to star variations now considered anomalous will soon be anything but.

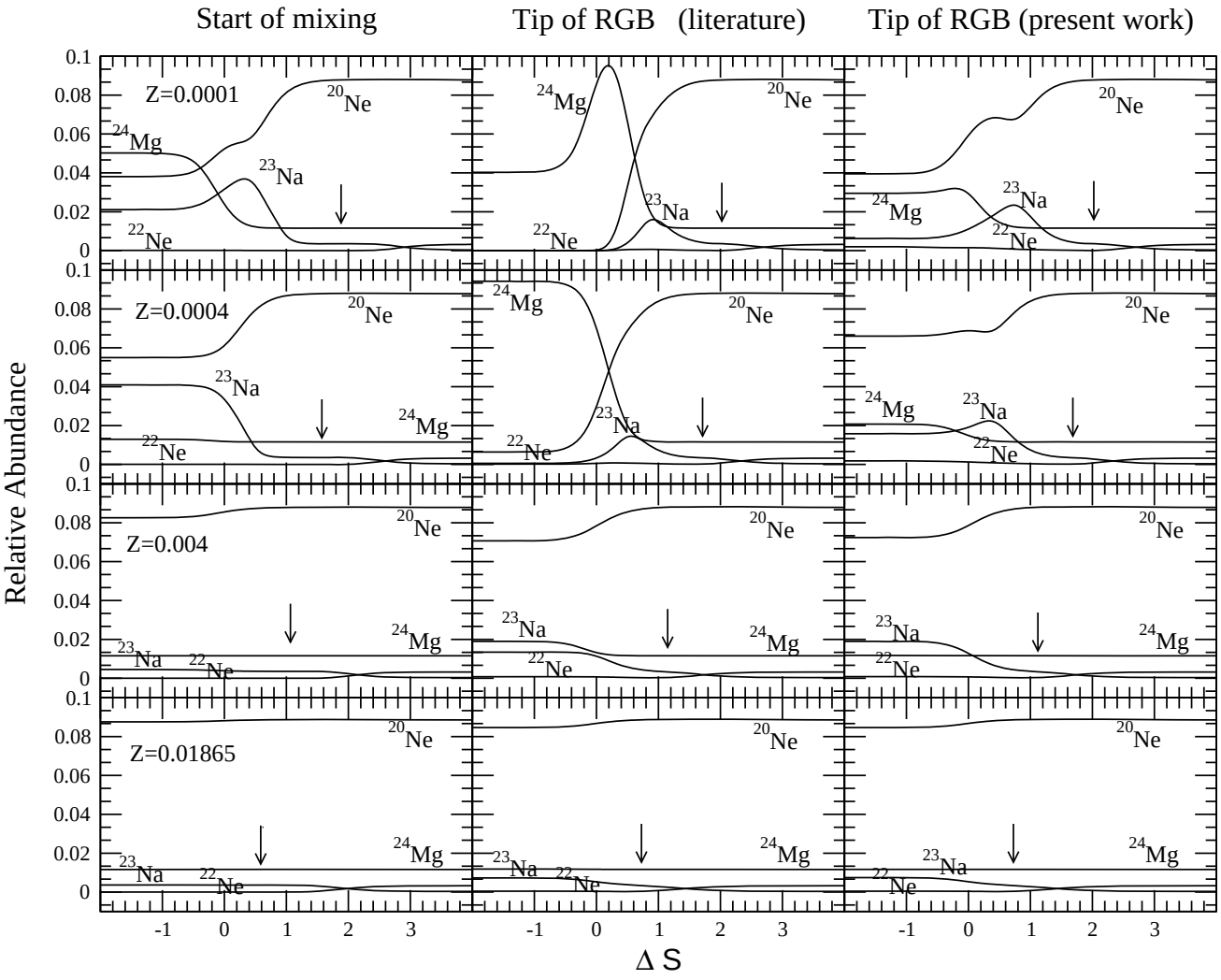

Figure 7.5: The NeNa mass region for four stellar sequences. The first column indicates the abundance profiles at the start of mixing; the second and third columns indicate the abundance profiles at the tip of the RGB obtained using ^{23}Na+p reaction rates from the literature [Ili01] and those obtained using rates from the present work, respectively. The ordinate is the number abundance relative to all metals. The abscissa, ΔS is the mass difference between any point and the center of the H-shell divided by the H-shell thickness [Cav98]. The arrows indicate the center of the O-shell.

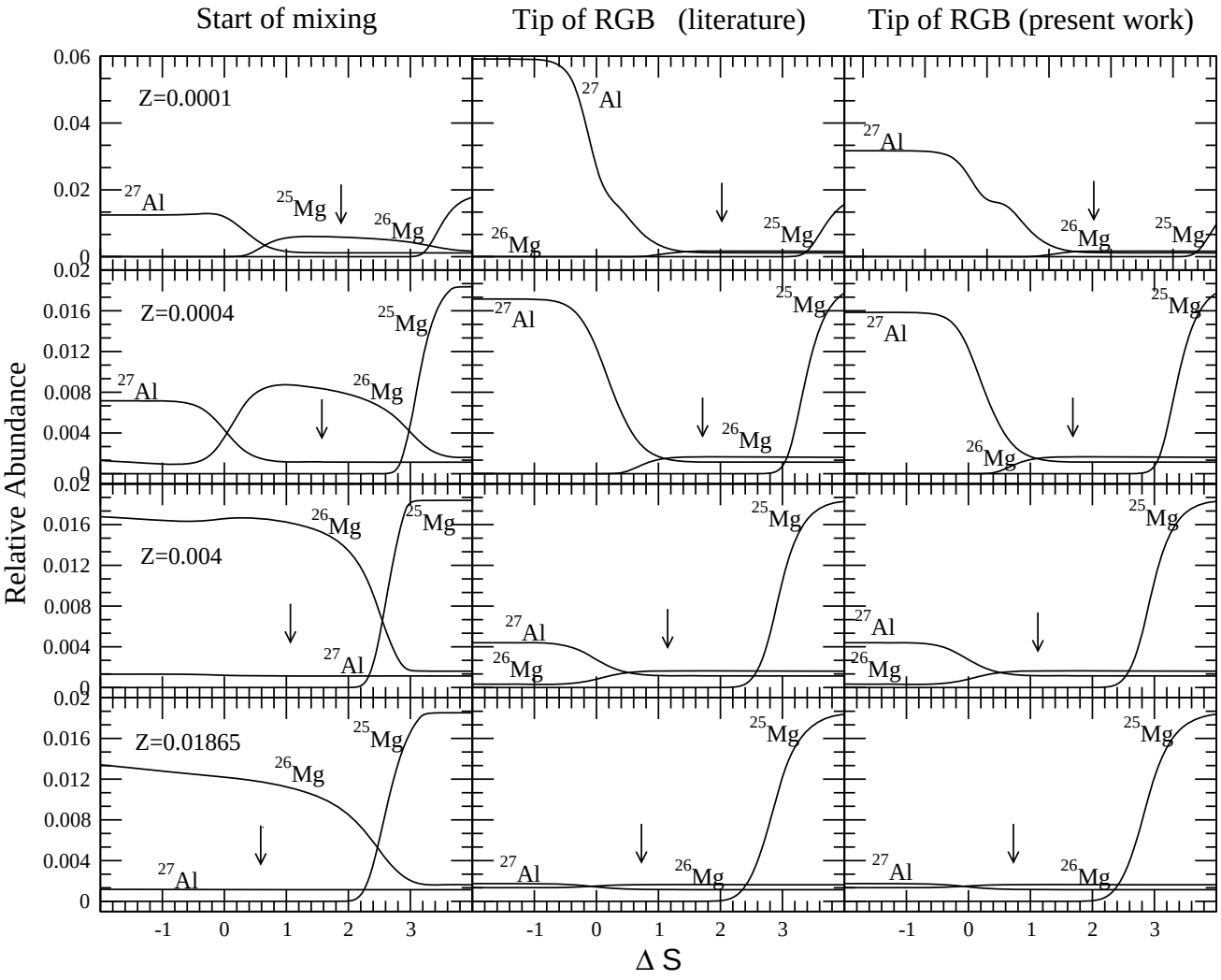

Figure 7.6: The MgAl mass region for four stellar sequences. The first column indicates the abundance profiles at the start of mixing; the second and third columns indicate the abundance profiles at the tip of the RGB obtained using ^{23}Na+p reaction rates from the literature [Ili01] and those obtained using rates from the present work, respectively. The ordinate is the number abundance relative to all metals. The abscissa, ΔS is the mass difference between any point and the center of the H-shell divided by the H-shell thickness [Cav98]. The arrows indicate the center of the O-shell.

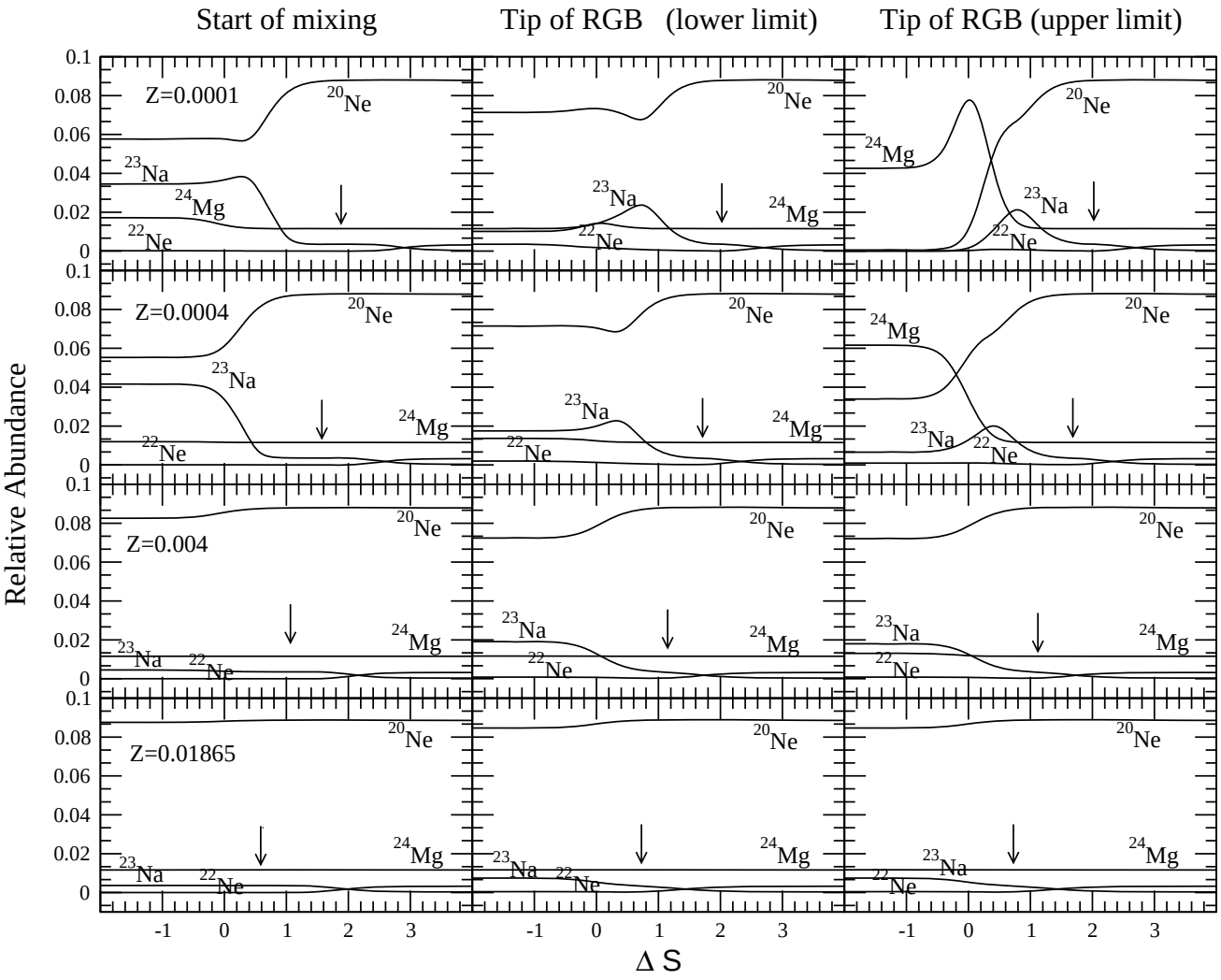

Figure 7.7: The NeNa mass region for four stellar sequences. The first column indicates the abundance profiles at the start of mixing; the second and third columns indicate the abundance profiles at the tip of the RGB obtained using the lower limits for the ^{23}Na(p,γ)^{24}Mg reaction rate (excluding the 144 keV resonance) and those obtained using upper limits, respectively. The ordinate is the number abundance relative to all metals. The abscissa, ΔS is the mass difference between any point and the center of the H-shell divided by the H-shell thickness [Cav98]. The arrows indicate the center of the O-shell.

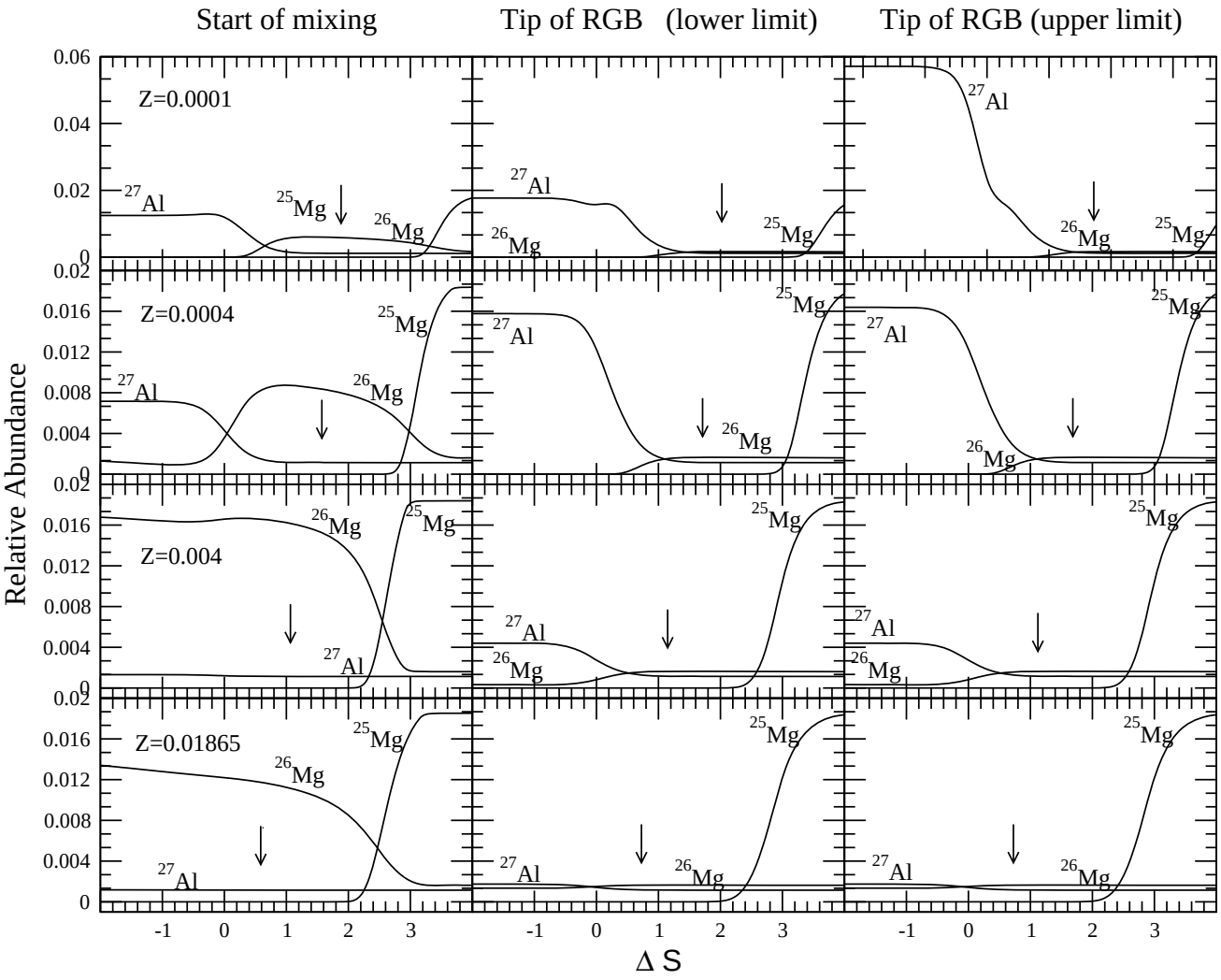

Figure 7.8: The MgAl mass region for four stellar sequences. The first column indicates the abundance profiles at the start of mixing; the second and third columns indicate the abundance profiles at the tip of the RGB obtained using the lower limits for the ^{23}Na(p,γ)^{24}Mg reaction rate (excluding the 144 keV resonance) and those obtained using upper limits, respectively. The ordinate is the number abundance relative to all metals. The abscissa, ΔS is the mass difference between any point and the center of the H-shell divided by the H-shell thickness [Cav98]. The arrows indicate the center of the O-shell.

Appendix A

Coincidence summing in γ-ray spectroscopy

A.1 Introduction

If two or more photons are emitted within the resolving time of a gamma-ray detector, an effect called coincidence summing will occur. The probability for summing increases with the total efficiency of the detector. Since total efficiency is a function of source-detector distance, the probability for summing increases when the source and detector are placed in close geometry. Coincidence summing is, however, not affected by count rate.

Consider the simple decay scheme shown in Fig. A.1. If γ_1 is detected in coincidence with γ_2, counts will be missing in the full-energy peaks for each of these transitions (at E_1 and E_2). This is referred to as "summing out". For example, if no coincidence summing occurs, the rate of counts in γ_1 is given by

$$n_{21} = A\frac{\epsilon_{21}^{p}}{1+\alpha_{21}}x_{21}, \tag{A.1}$$

where A is the source activity, x_{ji} is the branching ratio, α_{ji} is the internal conversion coefficient, and ϵ_{ji}^{p} is the full-energy peak efficiency. For most cases, the internal conversion coefficients are zero so that the rate of counts in γ_1 may be written more simply as

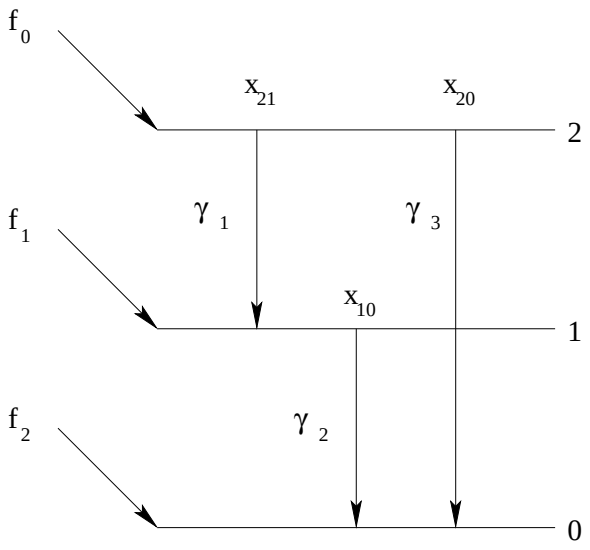

Figure A.1: A diagram defining decay scheme parameters. f_i are the feeding fractions and x_{ji} are the branching ratios.

$$n_{21} = A\epsilon_{21}^{p} x_{21}, \tag{A.2}$$

The rate of counts in γ_2 may be written similarly as

$$n_{10} = A\epsilon_{10}^{p} x_{21} x_{10}. \tag{A.3}$$

If each γ_1 is followed in coincidence with by γ_2, then the observed rate of counts from γ_1 will be smaller and may be written

$$n_{21}^{c} = A x_{21} \epsilon_{21}^{p} (1 - \epsilon_{21}^{t}). \tag{A.4}$$

The correction factor is then

$$C_1 = \frac{n_{21}}{n_{21}^{c}} = \frac{1}{(1 - \epsilon_{10}^{t})}. \tag{A.5}$$

For γ_2, the correction factor is found to be[Deb88]

$$C_2 = \frac{n_{10}}{n_{10}^{c}} = \frac{1}{(1 - \frac{x_{21}}{x_{10}} \epsilon_{21}^{t})}, \tag{A.6}$$

For γ_3, "summing in" may occur. That is, if γ_1 and γ_2 arrive in coincidence and deposit all of their energy into the detector, extra counts will appear in γ_3. The observed rate for γ_3 is given by

$$n_{20}^c = Ax_{20}\epsilon_{20}^p + Ax_{20}\epsilon_{20}^p\epsilon_{10}^p, \tag{A.7}$$

The correction factor for γ_3 is then written as

$$C_3 = \frac{n_{20}}{n_{20}^c} = \frac{1}{1+\frac{x_{21}\epsilon_{21}^p\epsilon_{10}^p}{x_{20}\epsilon_{20}^p}}. \tag{A.8}$$

A.2 Correcting the photopeak efficiencies

Semkow *et al.* [Sem90] details a technique for calculating coincidence-summing corrections for an arbitrarily large decay scheme. In this technique the general coincidence-summing equations were derived in matrix notation allowing for a first-order correction (combinations of only two coincident γ–rays) or a full correction (all possible combinations of emitted γ–rays). This technique was applied in the present work for the determination of sum-corrected full-energy peak efficiencies. Once sum-corrections are established for a particular source detector geometry, they may be applied to any γ-ray spectra taken with that geometry.

The complete formalism describing the sum corrections is too lengthy to be repeated here, but it may be found in Semkow *et al.* [Sem90] The photopeak efficiency is given by,

$$\epsilon_{ji}^p = \frac{S_{ji}}{I_{ji}} - \frac{D_{ji}}{[\mathbf{N}^{(0)}\mathbf{c}]_{ji}}, \tag{A.9}$$

where S_{ji} are the measured intensities, I_{ji} are the γ-ray emission rates, D_{ji} are the elements of the correction matrix $\mathbf{D}$, the matrix $\mathbf{N}^{(0)}$ contains information on the decay pattern, and the matrix $\mathbf{c}$ contains the branching ratios and conversion coefficients.

Calculating the photopeak efficiency in the presence of coincidence summing from A.9 is more complicated because the matrix $\mathbf{D}$ is a complicated function of ϵ_{ji}^p. It is found using a self-consistent iterative procedure [Sem90]. The corrected efficiency

may be written,

$$\epsilon_{ji}^{p}(m) = \frac{S_{ji}}{I_{ji}} - \frac{D_{ji}(m-1)}{[\mathbf{N}^{(0)}\mathbf{c}]_{ji}}, \tag{A.10}$$

where (m) is the iteration. The zeroth iteration corresponds to $D_{ji}(-1) = 0$, or the case where coincidence-summing effects are absent. The iterative procedure is continued until a desired degree of convergence in the ϵ_{ji}^{p} is reached.

A.3 Determining the source disintegration rate

A method for calculating the source disintegration rate in the presence of coincidence summing is described by Korun and Martinčič [Kor94]. This method is also based on the matrix algorithms presented in Semkow*et al.* Again, the formalism is too lengthy to be presented here, but the final result for the source disintegration rate is found to be

$$R = \frac{\sum_{j=1}^{N-1}\sum_{i=0}^{j-1}\frac{S_{ji}(NAM)_{ji}}{\Delta S_{ji}^{2}}}{\sum_{j=1}^{N-1}\sum_{i=0}^{j-1}\frac{(NAM)_{ji}^{2}}{\Delta S_{ji}^{2}}}, \tag{A.11}$$

and its uncertainty is

$$\Delta R^{2} = \sum_{j=1}^{N-1}\sum_{i=0}^{j-1}\frac{(NAM)_{ji}^{2}}{\Delta S_{ji}^{2}}, \tag{A.12}$$

Where S_{ji} are the measured γ-ray intensities and ΔS_{ji} are the uncertainties of those intensities. The matrices **N**, **A**, and **M** are described in Semkow*et al.* and Korun and Martinčič. Matrix **A** is a function of the peak efficiencies ϵ_{ji}^{p} and its purpose is to add the contribution from summing in. Matrices **N** and **N** are functions of the total efficiencies ϵ_{ji}^{t}. These two matrices subtract the contributions from summing out and they provide the decay pattern. Matrix **N** describes feeding of a particular level j from the decay of a parent as well as from the γ-decay above level j. Matrix **M** describes the decay pattern below the level i.

A.4 Performing the calculations

In the present work, software was developed to calculate photopeak efficiencies and source disintegration rates in the presence of coincidence summing based on the formalism of Semkow*et al.* and Korun and Martinčič The software has two main options: (1) To sum correct efficiency data from a source or known resonance or (2) to determine summing-corrected source disintegration rates and branching ratios. The latter option requires sum corrected efficiencies as input. In both cases it is assumed that the absolute total efficiency is known.

The software is designed to work for an arbitrary decay scheme. Consider, for example the simple β-decay of ^{60}Co shown in Fig. A.2. There can be a significant amount of summing out for γ_1 and γ_2. In order to sum correct efficiencies, the software requires the decay scheme of ^{60}Co. The input file should look like Table A.4. The first line after the "60Co" title indicates the number of levels above the ground state (in this case 2) and the fraction of 100 decays leading to this set of states. The latter number is usually 100, but some nuclei (like ^{152}Eu) decay in two final nuclei. The next three lines give the energy of each state and the feeding fraction. The following lines give information on the decays. For example, the line 1 0 100 1 0 indicates a transition from the J = 1 level to the I = 0 level with a branching ratio of (100 $\pm$1)% and an internal conversion coefficient of 0.

The software also requires the source activity and measured intensities. Table A.4 shows what this input file should look like. The first line under the "60Co" title is the source activity. The following give the observed intensity for each transition. For example the line 1 0 1332 62368 266 indicates a transition from the J = 1 level to the I = 0 level with γ-ray energy 1332 keV and an observed intensity of 62368 $\pm$ 266 counts [Lon03]. The software outputs the uncorrected and summing corrected efficiencies. For this example, the results are shown in Fig. A.3. As expected, the corrected efficiencies are larger.

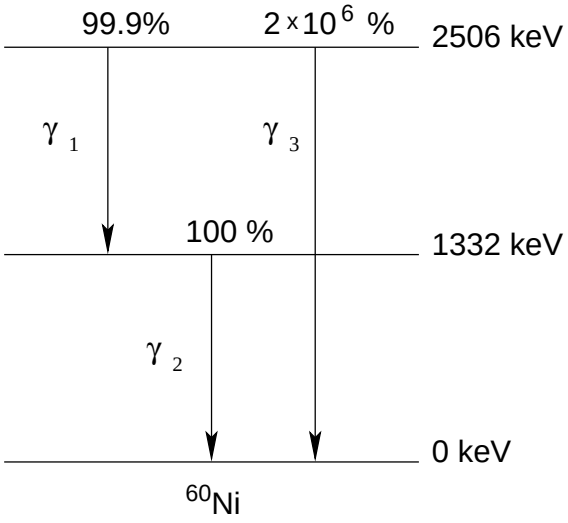

Figure A.2: Decay scheme of ^{60}Co.

60Co				
2	100			
0.0	0			
1332.516	0.00057			
2505.765	0.99941			
1	0	100	1	0
2	1	99.99	0.99	0
2	0	2e-6	2e-7	0

Table A.1: Data file for the decay of ^{60}Co.

60Co				
A=	1904605			
J	I	E	I	error
1	0	1332	62368	266
2	1	1173	67575	296
2	0	2506	3439	64

Table A.2: Input file containing source activity and observed intensities decay of ^{60}Co.

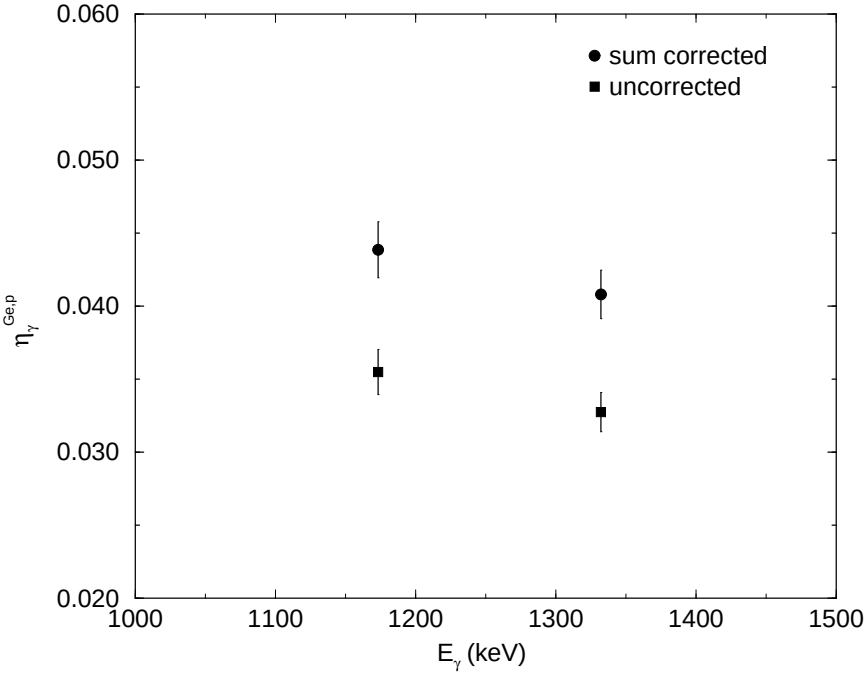

Figure A.3: Results from the summing correction software for the decay of ^{60}Co.

REFERENCES

[Ang99] C. Angulo, M. A. M. Rayet, P. Descouvemont, D. Baye, C. Leclercq-Willain, S. B. A. Coc, P. Aguer, and C. R. *et al.*, Nucl. Phys. **A656**, 3 (1999).

[Aud95] G. Audi and A. H. Wapstra, Nucl. Phys. **A595**, 409 (1995).

[Bie95] J. Biersack and J. Ziegler, "Transport of Ions in Matter, TRIM program Version 95.06", 1995.

[Bla93] T. C. Black, B. E. Hendrix, E. R. Crosson, K. A. Fletcher, H. J. Karwowski, and E. J. Ludwig, Nucl. Instr. and Meth. **A333**, 239 (1993).

[Bou94] Y. Bourlat, J. Millies-Lacroix, and D. Abt, Nucl. Instr. Meth. **A339**, 309 (1994).

[Boy75] S. G. Boydell and D. G. Sargood, Aust. J. Phys. **28**, 369 (1975).

[Bra75] F. Brauer, J. Kaye, and J. Fager, IEEE Trans. Nucl. Sci. **NS–22**, 661 (1975).

[Bro85] R. Brodzinski, D. Brown, J. Evans, W. Hensley, J. Reeves, N. Wogman, F. A. III, and H. Miley, Nucl. Instr. and Meth. **A23**, 207 (1985).

[Buc80] L. Buchmann, H. Becker, K. Kettner, W. Kieser, P. Schmalbrock, and C. Rolfs, Z. Phys. **A296**, 273 (1980).

[Cav98] R. M. Cavallo, A. V. Sweigart, and R. A. Bell, Astrophysical Journal **492**, 575 (1998).

[Coo72] J. Cooper and R. Perkins, Nucl. Instr. and Meth. **99**, 125 (1972).

[Deb88] K. Debertin and R. Helmer, *Gamma– and X–Ray Spectrometry with Semiconductor Detectors*, North–Holland, Amsterdam, 1988.

[End90] P. M. Endt, Nucl. Phys. **A521**, 1 (1990).

[End98] P. M. Endt, Nucl. Phys. **A633**, 1 (1998).

[Fis63] T. Fisher and W. Whaling, Phys. Rev. **131**, 1723 (1963).

[Fit03] R. P. Fitzgerald, *The RPF99 Monte Carlo Method*, B. Bros. Press, Tonawanda, 2003.

[Fla54] F. Flack, J. Rutherglen, and P. Grant, Proc. Phys. Soc. London **A67**, 68 (1954).

[For84] A. Forster, H. Kwon, J. Markey, F. Boehm, and H. Henrikson, Phys. Lett. **B138**, 301 (1984).

[Gie92] U. Giesen, *Study of α–capture and α–transfer reactions on ^{18}O and ^{22}Ne and astrophysical implications*, Ph.D. thesis, University of Notre Dame, 1992.

[Gör89] J. Görres, M. Wiescher, , and C. Rolfs, Astrophysical Journal **343**, 365 (1989).

[Gov59] H. E. Gove, *Nuclear Reactions, vol. I*, North-Holland, New York, 1959.

[Gov60] H. Gove and A. Litherland, *Nuclear Spectroscopy, Part A, ed. F. Ajzenberg–Selove*, Academic Press, New York, 1960.

[Hal99] S. E. Hale, *$^{22}Ne(p,\gamma)^{23}Na$, $^{23}Na(p,\gamma)^{24}Mg$, and globular cluster abundance anomalies*, Ph.D. thesis, University of North Carolina at Chapel Hill, 1999.

[Han99] M. D. Hannam and W. J. Thompson, Nuc. Instr. and Meth. **A431**, 239 (1999).

[Heu86] G. Heusser, Nucl. Instr. and Meth. **B17**, 418 (1986).

[Heu91] G. Heusser, Nucl. Instr. and Meth **B58**, 79 (1991).

[Heu93] G. Heusser, Nucl. Instr. Meth. **B83**, 223 (1993).

[Heu95] G. Heusser, Nucl. Par. Sci. **45**, 543 (1995).

[Ili90] C. Iliadis, T. Schange, C. Rolfs, U. Schröder, E. Somorjai, H. P. Trautvetter, K. Wolke, P. M. Endt, S. W. Kikstra, A. E. Champagne, M. Arnould, and G. Paulus, Nucl. Phys. **A512**, 509 (1990).

[Ili97] C. Iliadis, Nucl. Phys. **A618**, 166 (1997).

[Ili01] C. Iliadis, J. M. D'Auria, S. Starrfield, W. J. Thompson, and M. Wiescher, Astrophysical Journal Supplement Series **134**, 151 (2001).

[Ili03] C. Iliadis, 2003, private communication.

[Jos99] J. Jose, A. Coc, and M. Hernanz, Astrophysical Journal **520**, 347 (1999).

[Kam86] N. Kamikubota, H. Ejiri, T. Shibata, Y. Nagai, K. Okada, T. Watanabe, T. Irie, Y. Itoh, and T. Nakamura, **A245**, 379 (1986).

[Kay72] J. Kaye, F. Brauer, R. Connally, and H. Rieck, Nucl. Instr. and Meth. **100**, 333 (1972).

[Kor94] M. Korun and R. Martiničič, Nucl. Instr. and Meth. **A355**, 600 (1994).

[Kra94] R. P. Kraft, Publications of Astronomical Society of the Pacific **106**, 553 (1994).

[Kup63] J. Kuperus, P. Glaudemans, and P. Endt, Physica **29**, 1281 (1963).

[Lau96] J. Laurec, X. Blanchard, F. Pointurier, and A. Adam, Nucl. Instr. Meth. **A369**, 566 (1996).

[Lee99] J. Lee and B. W. Carney, Astronomical Journal **117**, 2868 (1999).

[Lon03] R. Longland, 2003, private communication.

[Mal84] H. Malm, M. Watt, I. Bostock, J. Campbell, P. Jagam, and J. Simpson, Nucl. Instr. and Meth. **223**, 420 (1984).

[Mas91] D. Masse, A. Adam, and J. Laurec, Nucl. Instr. and Meth. **A309**, 227 (1991).

[Mül90] G. Müller, F. Wissmann, F. Schröder, G. Mondry, H. Brinkmann, F. Smend, M. Schumacher, P. Fettweis, and R. Carchon, Nucl. Instr. and Meth. **A295**, 133 (1990).

[Pai78] B. Paine, S. Kennett, and D. Sargood, Phys. Rev. **C17**, 1550 (1978).

[Pow98] D. Powell, C. Iliadis, A. Champagne, S. Hale, V. Hansper, R. Surman, and K. Veal, Nucl. Phys. **A644**, 263 (1998).

[Pow99] D. C. Powell, *Determination of the $^{24}Mg(p,\gamma)^{25}Al$ reaction rate at low stellar temperatures*, Ph.D. thesis, University of North Carolina at Chapel Hill, 1999.

[Red82] A. Redder, H. Becker, H. Lorenz-Wirzba, and C. Rolfs, Z. Phys. **A305**, 325 (1982).

[Rol88] C. E. Rolfs and W. S. Rodney, *Cauldrons in the Cosmos*, The University of Chicago Press, Chicago and London, 1988.

[Row02a] C. Rowland, C. Iliadis, A. E. Champagne, A. K. Dummer, R. Fitzgerald, E. C. T. Harley, J. Mosher, and R. Runkle, Nucl. Instr. and Meth. **A480**, 610 (2002).

[Row02b] C. Rowland, C. Iliadis, A. E. Champagne, and J. Mosher, Phys. Rev. **C65** (2002).

[Run03] R. Runkle, 2003, private communication.

[Sch99] G. Schmid, D. Beckedahl, J. Blair, A. Friensehner, and J. Kammeraad, Nucl. Instr. Meth. **A422**, 368 (1999).

[Sem90] T. Semkow, G. Mehmood, P. Parekh, and M. Virgil, Nucl. Instr. Meth. **A290**, 437 (1990).

[Seu87] S. Seuthe, H. W. Becker, A. Krauss, A. Redder, C. Rolfs, U. Schroder, H. P. Trautvetter, K. Wolke, S. Wustenbecker, R. W. Kavanagh, and F. B. Waanders, Nucl. Instrum. and Meth. **A260**, 33 (1987).

[She96] M. D. Shetrone, Astronomical Journal **112**, 2639 (1996).

[Smi82] J. J. A. Smit, J. P. L. Reinecke, M. Meyer, D. Reitmann, and P. Endt, Nucl. Phys. **A377**, 15 (1982).

[Ste68] A. Stenberg and I. Olsson, Nucl. Instr. and Meth. **61**, 125 (1968).

[Swe79] A. V. Sweigart and J. G. Mengel, Astrophysical Journal **229**, 624 (1979).

[Swi75] Z. E. Switkowski, R. O. O'Brien, A. K. Smith, and D. G. Sargood, Aust. J. Phys. **28**, 140 (1975).

[Tak66] S. Takayanagi, M. Katsuta, K. Katori, and R. Chiba, Nucl. Instr. and Meth. **45**, 345 (1966).

[Ver88] W. J. Vermeer and D. M. Pringle, Nucl. Phys. **A485**, 380 (1988).

[Voj94] P. Vojtyla, J. Beer, and P. Stavina, Nucl. Instr. Meth. **B86**, 380 (1994).

[Voj95] P. Vojtyla, Nucl. Instr. Meth. **B100**, 87 (1995).

[Wor96] R. Wordel, D. Mouchel, T. Altzitzoglou, G. Heusser, B. Q. Arnes, and P. Meynendonckx, Nucl. Instr. Meth. **A369**, 557 (1996).

[Zop93] A. D. Zoppo, C. Agodi, R. Alba, G. Bellia, R. Coniglione, K. Loukachine, C. Maiolino, E. Migneco, , P. Piattelli, D. Santonocito, and P. Sapienza, Nucl. Instr. Meth. **A334**, 450 (1993).